Inaugural - Dissertation

Dissertation
submitted to the
Combined Faculties for the Natural Sciences and for Mathematics
of the Ruperto-Carola University of Heidelberg, Germany
for the degree of
Doctor of Natural Sciences

presented by
Alexander Georg Sperl, Dipl.-Phys.
born in Stuttgart, Germany

Date of oral examination: 08. February 2013

XUV–IR pump–probe experiments: Exploring nuclear and electronic correlated quantum dynamics in the hydrogen molecule

Gutachter: **Prof. Dr. Joachim Ullrich**
Prof. Dr. Andreas Wolf

Abstract

Wave packet dynamics and autoionization of doubly excited states in molecules can be studied by combining an intense, short-pulse infrared (IR) laser and a extreme ultraviolet (XUV) source with a Reaction Microscope, which allows for coincident measurements of ions and electrons. Furthermore, this detection system is capable of measuring the three dimensional momentum of each charged particle involved in the ionization process.

This technique was used to investigate the autoionization of doubly excited H_2 molecules, a process that occurs on a timescale of a few femtoseconds. Since this reaction time is of the order of the molecular motion, the nuclei can no longer be regarded as stationary. The coupling of the dissociation dynamics of H_2^+ to the corresponding electron, which is emitted through the autoionization of doubly excited states, leads to a symmetry breaking in the dissociation. In the conducted measurements, this translates into a localization of coincident electron–ion pairs. In order to study the temporal dynamics of these processes, the molecules were further probed with delayed IR pulses, revealing dynamics within the autoionization.

Zusammenfassung

Die Dynamik von molekularen Wellenpaketen sowie die Autoionisation von doppelt angeregten Zuständen in H_2 sind in der vorliegenden Arbeit mit Hilfe eines intensiven, ultrakurzen infrarot (IR) Lasers, einer zugehörigen extremen, ultravioletten Strahlungsquelle (XUV) und einem Reaktionsmikroskop untersucht worden. Das Detektionssystem ermöglicht hierbei koinzidente Messungen von Ionen und Elektronen, mit den entsprechenden dreidimensionalen Impulsen aller geladenen Fragmente, die aus einem vorangehenden Ionisationsschritt resultieren.

Die Kombination dieser Techniken wurde verwendet, um die Autoionisation von H_2 Molekülen, die auf der Zeitskala weniger Femtosekunden stattfindet, zu studieren. Da diese Prozesse im Zeitbereich von molekularen Schwingungen ablaufen, können die Kerne nicht als stationär Objekte behandelt werden. Darüber hinaus findet bei der Ionisation mit XUV Photonen über die doppelt angeregten Zustände eine Kopplung zwischen den H_2^+ Ionen und den zugehörigen Elektronen statt, durch die eine Symmetriebrechung in der Dissoziation hervorgerufen wird. Im Experiment zeigt sich diese über eine Lokalisierung der koinzidenten Ion–Elektron Paare. Um die zeitliche Dynamik zu visualisieren, wurden die doppelt angeregten Moleküle mit zeitversetzten IR Pulsen geprobt und offenbaren eine im Vergleich zur Wellenpaketdynamik deutlich verringerte Kopplung an den IR Laser.

Contents

1 Introduction

Pioneers of laser physics, such as Charles Townes and colleagues, who built the first maser (a laser in the microwave regime) [GZT54], or Theodore Maiman [Mai60], who succeeded in realizing light amplification in the optical domain, could not have imagined, how diverse laser applications in natural sciences would become. Particularly in the field of atomic physics lasers are used due to the extremely high temporal and spatial coherence, and feasible intensities that can be up to 10^{22} times higher than the intensity of sun light at the distance to the earth[1] [Yan+08]. Since the 1960s the processing of laser systems followed two main, almost contrasting directions. The first resulted in very stable monochromatic laser systems, which currently are indispensable in high–resolution spectroscopy, as well as in the preparation and trapping of ultracold atomic samples into specific states [And+95]. The other has led to pulsed, broad–band lasers which opened new research areas within atomic and molecular physics. Among these, attosecond science has become an important field within the last 12 years, with constant progress in attosecond source developments, pulse–characterization techniques and most significantly, applications for quantum dynamical studies.

Guided by the fast development of laser systems in the 1970s and 1980s, investigations of non–linear processes in light–matter interaction have become possible with high field intensities. For example, the conversion of photon energies to the soft and extreme ultraviolet regime (XUV), triggered by strongly driven valence electrons in the laser field, was reported. An important milestone in this context was achieved in 1987 by McPherson et. al., who studied multiphoton ionization processes in rare gases and observed photon energies of odd multiples of the fundamental, incident light [McP+87]. In subsequent years, principal features of this "high–harmonic generation" (HHG) were analyzed, such as the plateau building behavior which means that the photon energies extend to a high–harmonic order at a nearly constant conversion efficiency [Fer+88]. Only one year after this discovery, first numerical calculations emphasized, in view of a high XUV–photon flux, the importance of the so–called phase–matching condition[2] and a clean linear polarization of the incident light field [KS89]. Further findings were obtained by calculations and experiments, including the atom response to the field, the propagation of the generated light and

[1] The highest intensity is probably provided by the HERCULES laser, operating at 300 TW at a repetition rate of 0.1 Hz with a pulse duration of 30 fs and a single pulse energy of almost 10 J.

[2] For efficient HHG as many atoms as possible must contribute and the emitted photons have to add up constructively in the laser propagation direction. This condition is termed phase matching [Cha11].

the role of the laser focusing and dispersion effects in gaseous targets [LSK91; LB93]. An

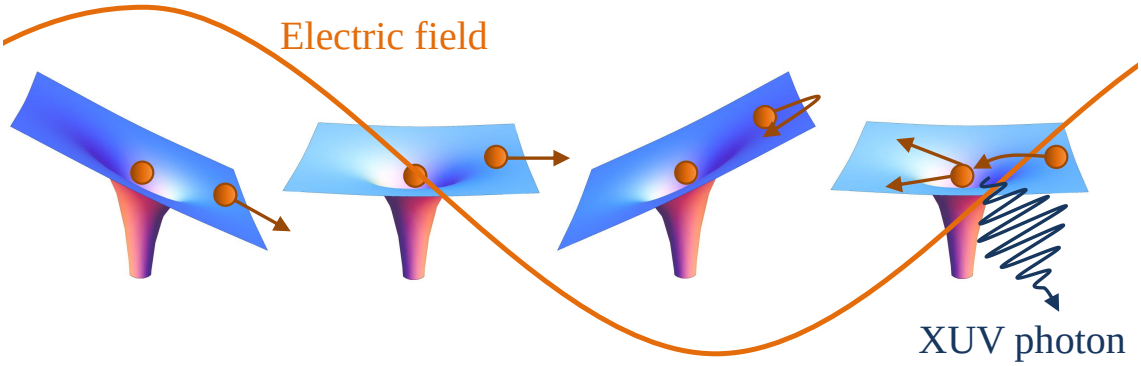

Figure 1.1: Three–step model of the HHG. First, the atomic Coulomb potential is lowered by the strong and comparably slow varying electric field such that an electron tunnels out. The electron is accelerated by the field for a half–cycle period of the laser and returns to the vicinity of the nucleus. In addition to elastic and inelastic scattering, the electron may recombine with its parent ion, thus emitting a highly energetic XUV photon.

exciting moment in this fast growing research field was evoked by the assumption, that the HHG could be a promising candidate for an attosecond beam source [HMH93]; however, it took several years, until the temporal duration of the harmonics became measurable and controllable [Glo+96; Pau+01]. In 1996 it could be shown that the high–harmonic light is confined in attosecond pulse trains (APTs) which contain several single–XUV pulses that are temporally spaced by the half period of the generating laser beam [ALL96].

A theoretical background for the HHG and its attosecond nature was given in 1993 by Corkum and Kulander [Cor93], who introduced an intuitive, semiclassical interpretation of the HHG in a three–step model which was based on the work of Keldysh [Kel65], as well as Ammosov, Delone and Krainov [ADK86]. In this theory, the strong laser field ionizes an atom and drives the free electron such that it gains kinetic energy and recombines with its parent ion, emitting a photon with high energy (see Figure 1.1). A short time afterwards, the theory on HHG was supplemented by Lewenstein and colleagues with a more precise, quantum–mechanical and analytical model. These contributions helped to distinguish the HHG in terms of short and long electron trajectories, since both lead to the generation of XUV light; however, with different properties. Two important characteristics, related to the question, whether HHG is suitable as an attosecond laser source or not, are the coherence and the divergence of the beam. The first of these issues was addressed in [Zer+97] where the authors showed in a twofold HHG process with a subsequent interference of the beams, that the high–harmonic light exhibits a high degree of coherence. Furthermore, it could be demonstrated [Bel+98], that long electron trajectories feature a comparably large divergence, suggesting an enhancement of the short trajectories in experimental setups.

In the late 1990s, high–harmonic radiation was preferentially produced with ultrashort, femtosecond pulses from Ti:Sapphire lasers [Nis+97a; Sch+98], which allowed for the generation of single attosecond pulses (SAP), and photon energies above the water window[3] [Spi+97]. The advancement of the Ti:Sapphire laser systems in terms of generating single–cycle, carrier envelope phase–stabilized pulses and the invention of gating techniques further led to several significant improvements on the generation of SAP [Dre+01; San+06].

In addition to these progress, attosecond pulse characterization methods were pushed forward, in order to provide more control over the HHG. The first measurements were based on a cross–correlation of HHG–XUV pulses [Kob+98]; however, with the development of the so–called RABBITT technique, a powerful characterization method became available [Pau+01]. In this method, the XUV and its generating infrared (IR) field are spatially overlapped on an atomic target and temporally delayed with respect to one another. Electrons are ionized by single XUV photons and eventually absorb (or emit) photons from the collinear IR beam, giving rise to sideband electron energies (which can be distinguished from electrons that are ionized by a single XUV photon). As a function of the time delay between the XUV and IR pulses, the sideband signals oscillate and, thus, represent the temporal phase of the harmonic pulse trains. Recently, this technique was extended to study electron dynamics in atoms [Mai+03; Mau+04; Klü+11]. Note, for SAP there exists an analogous method to RABBIT which is referred to as streaking [Kie+02; Sch+10]. A comprehensive overview of the most important developments in attosecond physics is provided by several review articles, such as [CC10; KI09; NS09; GCK12].

In this work, state–of–the–art technologies for the generation of ultrashort, femtosecond–IR and attosecond–XUV laser pulses were combined with a reaction microscope (ReMi), thus, enabling unique quantum–dynamical studies below the timescale of molecular vibrations. The present setup offers several advantages in comparison to other laser and detection systems. First, the photon energies and the duration of the attosecond laser pulses allow to induce "simple" single–photon transitions at a well–defined time. Furthermore, multiphoton or in general strong–field processes with infrared or optical lasers are not required in order to excite, for example, highly–energetic states. Second, both the attosecond–XUV and the femtosecond–IR laser beams are inherently phase correlated, since the high–harmonic generating IR pulses transfer their phase information onto the corresponding XUV–APTs. This fact is crucial for pump–probe measurements with subcycle resolution. Third, the utilized detection system is the most advanced device to analyze ionization processes, because the three–dimensional momenta of all charged particles are recorded, resulting in fully–differential data sets and angular distributions. In addition, the ReMi allows for the detection of multiple, coincident particles and, thus, an event–by–event analysis of ionization processes.

[3] The water window ranges between 280 and 540 eV. Water is transparent for X-rays in that region, in contrast to carbon and nitrogen. The radiation is therefore used to study biological samples.

Two typical experimental schemes in the field of light–matter interaction are especially suited to utilize the full capabilities of a ReMi. These are sequential and non–sequential double–ionization as well as molecular fragmentations. In contrast, photo–induced single–ionization of atoms, for instance, can also be studied in less complex detection devices, such as time–of–flight [Hen+01], magnetic–bottle–electron [KR83; Rij+00] and velocity–map–imaging [Bor+96; EP97; Mau+08] spectrometers. In single ionization, ions and electrons exhibit identical absolute momenta and they are emitted back–to–back. As their dynamics are imprinted primarily along the polarization axis of the laser, a measurement of two components of the three–dimensional momentum vector is usually sufficient to explore the complete process.

Following these arguments, it is convenient to operate ReMis in ionization experiments with molecules and study processes, where the specific structure of the molecule, as well as its orientation in the laboratory frame of reference, becomes relevant. A prototype system in this context is the molecular hydrogen H_2 and its associated ion, the H_2^+, which both consist of two protons and two or one electron(s), respectively. In comparison to other homonuclear, diatomic molecules, the nuclear dynamics can be extremely fast, even in the order of 10 fs and, thus, reach the range of electronic correlation times [SBM06]. A process, where the nuclear motion and the electron–electron interaction both become significant arises for example from the population of doubly–excited states. These highly energetic states are totally repulsive resulting in two neutral, but excited hydrogen atoms in the final state. However, under some conditions, this dissociation is accompanied by a molecular Auger, autoionization process with a probability that strongly depends on the instantaneous internuclear distance [SM97]. In other words, the autoionization width of a particular Auger decay channel changes as a function of time, since the corresponding doubly–excited molecular state dissociates and, thus, the internuclear distance increases continuously. Vice versa, if autoionization occurs during dissociation, the new electronic potential curve might be a binding state of the molecular ion, such that the electronic transition directly influences the nuclear dynamics.

These considerations illustrate how the non–separable autoionization and dissociation effects, reflecting electron and nuclear dynamics, transform the apparently simple molecule into a complex four–body quantum–dynamical system, demanding for advanced, fully quantum mechanical theoretical descriptions [Mar99]. Studying this form of interaction between nuclear and electronic dynamics was one of the main goals in this project and the technique to initiate and trace these processes was based on single and two–color pump–probe laser pulse measurements. In this context, the combination of short laser pulses and high photon energies along with the ability of fully characterizing the final momentum state with the ReMi were crucial in order to distinguish several collateral dissociative ionization processes, often leading to the same final state: $H^+ + H^{(*)} + e^-$.

One of the processes investigated is the direct, single–photon induced “ground–state dissociation” and the “nuclear–wave packet dynamics”, that can be traced with a time–

delayed, ultrashort IR laser field. Hereby, the first XUV photon ionizes the molecule and excites coherently several vibrational levels in an almost instantaneous step, giving rise to the formation of a wave packet that oscillates within the potential energy surface of the bound $H_2^+(1s\sigma_g)$. Its properties can be investigated by the absorption of an additional IR photon, by means of a projection onto the dissociative continuum of the hydrogen molecular ion, revealing time dependent structures, such as fast ($\sim$ 26 fs) and slow ($\sim$ 305 fs) oscillations. Here, they are all followed over an extended time interval of $\sim$ 1200 fs such that a Fourier analysis of the temporal wave–packet dynamics yielded a high energy resolution and enabled to extract and identify contributions of individual vibrational states. Similar results obtained with intense ultrashort laser pulses have been presented before [Erg+05; Erg+06c], as well as with XUV light [Kel+09], but the present measurement is the first to combine XUV and IR pulses within a kinematically complete detection system.

A different process which can be induced by photon energies starting from $\sim$ 27 eV is the simultaneous resonant excitation of both electrons to series of doubly–excited states, as mentioned before. The same photon energy suffices to ionize the molecule directly, giving rise to Fano profiles in the photon–absorption cross sections and a fast autoionization process of the doubly–excited states [Fan61; SM97]. The transition, involving electron–electron correlation and nuclear motion is governed by selection rules and, thus, by the symmetry of the states, yielding significant consequences with respect to autoionization times[4] and energies [BD74; SM97; SM99b]. Here, the coincident detection technique provides the possibility to identify several of these states, by the energies and the angular distributions of the particles, as well as through the initial orientation of the molecule in the laboratory frame of reference [HE02]. Furthermore, a large contribution of ionized and directly dissociating molecules is identified. As all of these processes exhibit quantum mechanical overlap regions in energies, it is possible to encounter the same final state via two or more competing pathways. This interference can ultimately result in an asymmetry or so–called "localization" effect, whereby ionized electrons and dissociating ions propagate preferentially in the same or in opposite directions [Laf+03] and [Mar+07]. However, it is important to note, that more conditions must be fulfilled in order to measure this form of entanglement between ions and electrons. In addition, there exist other possibilities to cause asymmetry effects with laser fields, as shown in [Red+12; Kli+06; Kre+09] for molecular hydrogen and [Gol+97] for molecular oxygen.

In this work, the described asymmetry has been observed for the first time in a complete picture, showing the full energy–partition range between electrons and ions for all configurations between the laser polarization and the original molecular axis. Hereby, the doubly–differential correlated energy diagram and the electron angular distributions in the molecular frame of reference were used to identify the involved doubly–excited states of

[4] Doubly–excited Q_1 states of Σ_u^+ symmetry have in contrast to Π_u states a short autoionization time, when the H_2 molecule is close to its equilibrium distance.

H_2 as well as the relevant non–resonant states of H_2^+. Thus, it was possible to distinguish different localization–processes in two oppositional orientations of the molecule; one where the internuclear axis and the polarization of the laser are parallel with respect to each other and another, where they are perpendicular. A simple representation of this asymmetry, for instance, is given in Figure 1.2 (b) for the first, parallel case. The red and blue energy ranges denote coincident ions and electrons which are emitted preferentially into the same (red) or into opposite (blue) hemispheres, respectively. The corresponding kinetic energy distribution of the electrons is shown in Figure 1.2 (a).

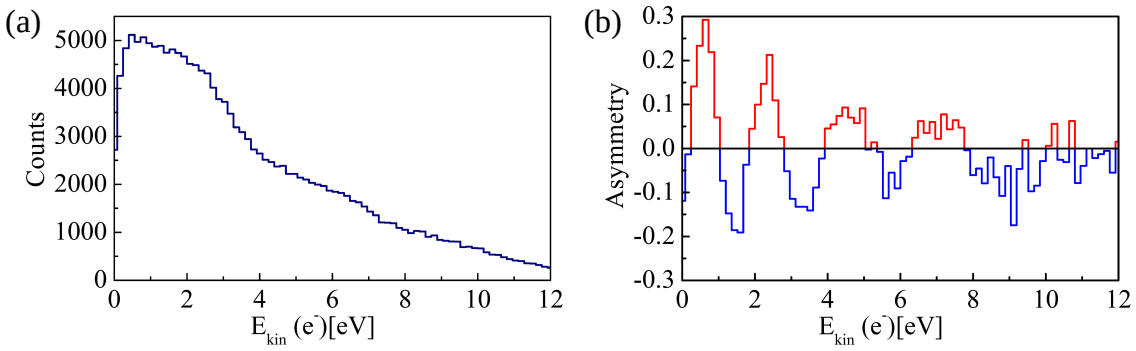

Figure 1.2: (a) Measured kinetic energy distribution of the electrons for parallel transitions. Here, the molecule and the polarization axes are parallel. (b) Asymmetry for the same events. The red and blue sections denote energy ranges where ions and electrons preferentially fly into the same or into opposite directions, respectively.

Furthermore, the results include pump–probe measurements on the population of doubly–excited states, with the objective of influencing and potentially controlling the process of autoionization dynamically. Although the observed effects have been small, it was possible to obtain pivotal findings, which can be used as a guideline for future experiments. For example, we identified different IR–dependencies for the two mentioned molecular orientations with respect to the polarization axis. In parallel transitions, first indications of sideband structures in doubly–excited states were measured and confirmed the theoretical results recently presented in [SRM12]. In contrast to that, a strong IR–coupling between the doubly excited H_2^{**} and the anti–binding H_2^+ states was observed for perpendicular transitions. In addition, the ion yield as a function of pulse–delay, indicates that the autoionization width of doubly–excited states of different symmetry varies strongly, thus offering a first direct measurement of the lifetime of doubly–excited states, in comparison to the method, described in [Gar+06].

Following this brief motivation on quantum dynamical studies of small molecules with XUV and IR laser pulses, this thesis will begin with a theoretical chapter, introducing basic concepts on short laser pulses and HHG. A description of ultrashort laser pulses and the effect of dispersion will be given, as one of the technical parts of this work was the design

and commissioning of a stable hollow–core fiber system in order to increase the spectral width and to achieve shorter pulse durations. Furthermore, basic theoretical concepts on the light–atom interaction will be presented with an emphasis on HHG as a consequence of electron recollision with the parent ion. Chapter 3 will explain general features of small two–atomic molecules and describe detailed properties of the hydrogen molecule and its associated ion H_2^+. An introduction to the quantum dynamical representation of molecular states and the definition of symmetries is included to facilitate the discussion on transitions and angular distributions of electrons. Finally, the section will close with considerations of laser–pulse molecule interactions, including scenarios with highly energetic, but low intense XUV radiation as well as low energetic, but intense femtosecond IR laser pulses. In chapter 4, the complete experimental setup will be presented, starting with the laser system and the subsequent spectral broadening via hollow–core fiber. Then, the experimental realization of the HHG will be described, including details on the versatile characteristics of the generation chamber and measured spectral profiles. The last section in the experimental discussion will address the reaction microscope and present possibilities to identify coincident particles in ionization processes. Furthermore, the extraction of molecular frame photoelectron angular distributions (MFPADs) in fragmentation of diatomic molecules will be illustrated. In chapter 5, single–pulse XUV and two–color XUV–IR pump–probe experiments with molecular hydrogen will be shown. The discussion will begin in section 5.1 with the XUV–photon induced ground–state dissociation and the generation of vibrational wave packets in the hydrogen molecular ion. The XUV–photon induced population of doubly excited states as a signature of electron–electron correlation will be analyzed in section 5.2. These states further evoke asymmetry effects, or in other words, localization of charged particles which has been studied in great detail. The dynamics of these states, such as the repulsion of the nuclear fragments, as well as the extremely "fast" autoionization were investigated with ultrashort XUV and IR pulses and the results are presented in section 5.3. This thesis will conclude with a summary of the results and provide suggestions and ideas for future experiments on H_2 and other small molecules.

2 Ultrashort laser pulses and high–harmonic generation

In the development of pulsed laser systems the primary goal has remained to achieve high repetition rates and – more importantly – high field intensities by increasing the single pulse energy ϵ or by decreasing the pulse duration τ [KS08]. In this work, such pulses were used to study fast temporal dynamics and electron–localization effects in the dissociative ionization of molecular hydrogen. The necessary conditions for these experiments has been provided by the generation of two types of laser pulses, including high–intensity $\sim 10\,\mathrm{fs}$, infrared (IR) pulses from a Ti:Sapphire CPA–system and, highly energetic, extreme–ultraviolet (XUV) pulses which result from a process termed high–harmonic generation (HHG). It is therefore worth reviewing a few select basic properties of both types of laser pulses. We will begin with a discussion on the representation of general light fields and short laser pulses. Subsequently, pulse propagation through dispersive media will be elucidated and four important dispersion parameters are introduced.

These basic considerations are sufficient to describe IR pulses; however, as the XUV radiation results from strong–field interactions with atoms, it is necessary to briefly explain the most relevant ionization mechanism, in particular the laser–induced electron tunneling. On this basis and within the frame of a semiclassical model, it is possible to derive several characteristics of the HHG. Afterwards, the theoretical background will be expanded with quantum mechanical considerations which follow from the strong field approximation (SFA) and the Lewenstein model.

2.1 General light fields

In dipole transitions, the dominant contribution in the dipole operator is provided by the electric part of the light field. As magnetic dipole transitions are accounted in the second order of the matrix element, it is convenient to consider only the electric field of an electromagnetic wave.

An intuitive way to describe the electric field $E(t, \boldsymbol{r})$ of a light wave is to assign every point in space–time a certain field amplitude. An equivalent approach is a characterization in the frequency–wave vector domain $\tilde{E}(\omega, \boldsymbol{k})$. Both representations are valid and can be connected via the Fourier transform. For now we want to neglect the space and wave vector dependence of E and $\tilde{E}$ and concentrate on the time or frequency dependent parts, since

they are both crucial for an understanding of ultrashort pulses. Any optical light field can be described by a time–dependent envelope or amplitude function $F(t)$ and a phase factor which contains the center carrier frequency ω_0 and a temporal phase $\phi(t)$.

$$E(t) \;=\; F(t)\,\cos(\omega_0 t + \phi(t)) \tag{2.1}$$

The electric field is a real quantity, but for mathematical reasons it is appropriate to use a complex representation:

$$E(t) \;=\; F(t)\,e^{i[\omega_0 t+\phi(t)]} \quad + \quad c.c. \tag{2.2}$$

As mentioned previously, the electric field in the frequency domain is obtained by performing a Fourier transform in time. The resulting pulse–function $\tilde{E}(\omega)$ can be separated similarly to (2.2) into a spectral amplitude $U(\omega)$ and a spectral phase $\varphi(\omega)$:

$$\tilde{E}(\omega) \;=\; \int_{-\infty}^{+\infty} E(t)\,e^{-i\omega t}dt \;=\; U(\omega)\,e^{i\varphi(\omega)} \tag{2.3}$$

This connection between $E(t)$ and $\tilde{E}(\omega)$ suggests that the temporal width of a short pulse is inversely proportional to its spectral width.

Technically, ultrashort laser pulses are generated in a periodical process, which means that the envelope function $U(\omega)$ in the frequency domain is not continuously; instead it is composed of equally spaced spectral components, each assigned a certain amplitude. This method is realized in typical mode–locked femtosecond–oscillator systems, where amplified frequencies within the resonator interfere constructively and form short, periodic pulse structures in narrow time windows, as shown in Figure 2.1.

From all presented quantities $F(t)$, $U(\omega)$, $\phi(t)$ and $\varphi(\omega)$, the spectral amplitude is technically the easiest to measure; however, only the knowledge of the spectral phase provides relevant information about a short light field. Simply spoken, the spectral amplitude determines how short a pulse can be but only the spectral phase determines how short the pulse effectively will be. This is also illustrated in the description of pulse propagation through a dispersive medium by expanding $\varphi(\omega)$ in a Taylor series, as in section 2.2.2. In contrast, the temporal phase is a more conceptual quantity, as its first time–dependent derivation allocates every frequency component in a particular time and therefore gives a more intuitive picture of the pulse and its corresponding duration. All these basic facts illustrate the importance of both domains and their connection via Fourier transform.

2.2 Description and properties of few cycle laser pulses

So far the envelope functions of neither the field amplitude $F(t)$ nor the spectral amplitude $U(\omega)$ have been specified. There exist many suitable forms based on Lorenzian,

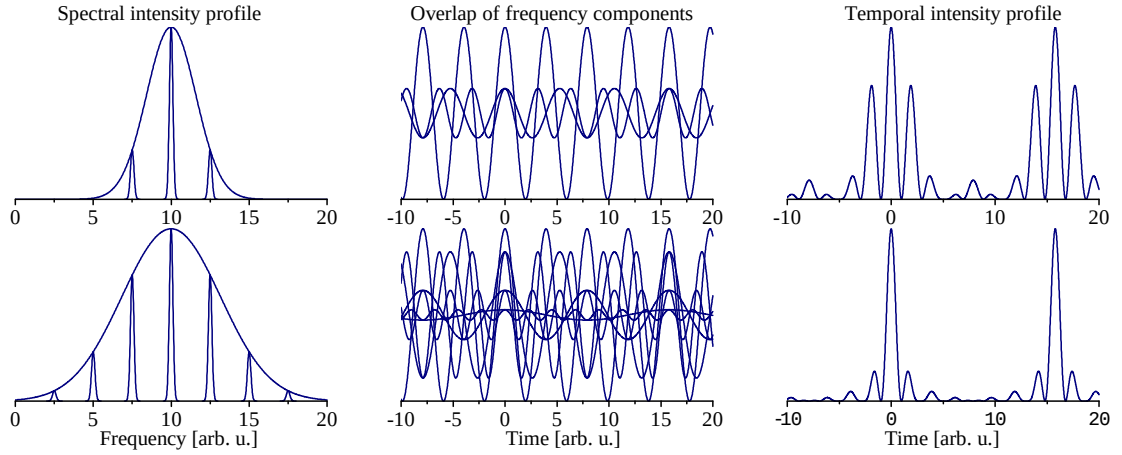

Figure 2.1: Frequency components around $\omega_0 = 10$ are overlapped and superimposed, resulting in periodic pulses in the time domain. The more frequencies that are phase locked, the shorter the pulses become and fewer substructures in between are generated. Here, constructive interference occurs at times 0 and 15.8 arbitrary units.

Gaussian, exponential or linear and squared hyperbolic secant shapes; however, Gaussian functions are commonly used in theory and literature for several reasons. First, they are not extremely far of from reality, even if general pulses may exhibit asymmetric shapes. Second, they can be treated analytically to a certain degree in calculations and simulations. Furthermore, they remain Gaussian shaped under Fourier transform.

Prior to continuing with characteristics of Gaussian laser pulses, it should be mentioned that a more general description of laser pulses is given by the Wigner form [Wig32] which consequently connects all spectral and temporal properties in a two-dimensional representation of waves [DR06; Coh95; Sch01].

2.2.1 Pulses described by Gaussian envelopes

Here, we define the envelope functions in the equations (2.2) and (2.3) as Gaussian profiles, with the peak amplitudes F_0 and U_0:

$$E(t) = F_0\, e^{-2\ln 2\,(\frac{t}{\tau})^2}\, e^{i[\omega_0 t+\phi(t)]} \qquad \tilde{E}(\omega) = U_0\, e^{-2\ln 2\,\frac{(\omega-\omega_0)^2}{(\Delta\omega)^2}}\, e^{i[\varphi(\omega)]} \tag{2.4}$$

The pulse duration (full width at half maximum of the temporal intensity) and the spectral width are given by τ and $\Delta\omega$, respectively. If the spatial dependence of the pulses correspond to a Gaussian beam with beam waist w, it is possible to write $E(r,t)$ as follows:

$$E(r,t) = \sqrt{\frac{2}{\pi w^2}}\, e^{-(\frac{r}{w})^2}\, E(t) = \sqrt{\frac{2}{\pi w^2}}\, F_0\, e^{-(\frac{r}{w})^2}\, e^{-2\ln 2\,(\frac{t}{\tau})^2} \tag{2.5}$$

Two important quantities in ultrafast optics are the peak power P_0 and the peak intensity I_0. In particular I_0 is important, as many interesting processes are highly nonlinear and, thus, show a strong intensity–dependence.

$$P_0 \;=\; \frac{\varepsilon}{\int_{-\infty}^{+\infty} e^{-4\ln 2\left(\frac{t}{\tau}\right)^2} dt} \qquad \Rightarrow \qquad I_0 \;=\; \frac{2P_0}{\pi w^2} \;=\; 4\sqrt{\frac{\ln 2}{\pi^3}}\,\frac{\varepsilon}{w^2\tau} \tag{2.6}$$

By increasing the single pulse energy ϵ or equally, by decreasing the pulse duration τ, higher values of P_0 and I_0 can be achieved. Other notable parameters in femtosecond–laser systems are the average power P_{average} and the repetition rate f_{rep}.

$$P_{\text{average}} = f_{\text{rep}} \cdot \varepsilon \tag{2.7}$$

Another pulse property that connects the pulse duration and the corresponding spectral profile can be specified by the time–bandwidth product $\tau \cdot \Delta\omega$ which assigns a minimum possible pulse duration to a given spectrum. For Gaussian pulses,

$$\tau \cdot \Delta\omega \;=\; \frac{2\ln 2}{\pi} \quad . \tag{2.8}$$

2.2.2 Pulse propagation and dispersion

Dispersion characterizes the influence of transparent media on the temporal profile of an ultrashort laser pulse. This effect appears in frequency dependencies of several material parameters, like the susceptibility and the refractive index and, therefore, the speed of light in a medium [KS08]. Without appropriate control mechanisms, dispersion may lead to devastating changes in the temporal shape of the pulses. Optical elements, such as lenses, prisms and even air, allot different frequency components to different speeds of light, with the result that the pulse broadens in time or even becomes deformed.

In the theoretical frame of linear optics, the change of the pulse will be independent of its intensity profile. As unfocused pulses propagating through dispersive media fulfill this condition, it is convenient to perform the calculation of the time evolution of the pulse in the spectral domain and display the result in the temporal regime via the Fourier transform (2.3). Moreover, the envelope will only change slightly during a cycle period of $\frac{2\pi}{\omega_0}$, therefore according to the "slowly varying envelope approximation", the calculation can be reduced to the temporal pulse envelope function. All the different aspects of dispersion can be understood in a Taylor expansion of the spectral phase $\varphi(\omega)$ or the frequency–dependent wave number $k_n(\omega)$. The latter function allows a description with a dependence of the propagation length z through the dispersive medium.

$$\begin{aligned} \varphi(\omega) &= \varphi(\omega_0) + \varphi^{(1)}(\omega-\omega_0) + \frac{1}{2}\varphi^{(2)}(\omega-\omega_0)^2 + \frac{1}{6}\varphi^{(3)}(\omega-\omega_0)^3 + \cdots = \\ k_n(\omega)z &= k_n(\omega_0)z + k_n^{(1)}z(\omega-\omega_0) + \frac{1}{2}k_n^{(2)}z(\omega-\omega_0)^2 + \frac{1}{6}k_n^{(3)}z(\omega-\omega_0)^3 + \cdots \end{aligned} \tag{2.9}$$

$$\text{with} \qquad \varphi^{(i)} = \left.\frac{d^i\varphi}{d\omega^i}\right|_{\omega=\omega_0} \qquad \text{and} \qquad k_n^{(i)} = \left.\frac{d^i k_n}{d\omega^i}\right|_{\omega=\omega_0} \tag{2.10}$$

Generating even short laser pulses goes conjointly with a broadening the spectral width, whereby dispersion parameters $\varphi^{(i)}$ of higher order become more important. Therefore one has to account for the influence of $\varphi^{(3)}$ for pulses with few optical cycles in the sub–8 fs regime. In Figure 2.2, a pulse of 5 fs duration is shown with the respective influence of the first four dispersion parameters:

$$\varphi^{(0)} = z\,k_n = \frac{2\pi}{\lambda}\,n \qquad \text{PD: Phase delay} \tag{2.11}$$

$$\varphi^{(1)} = z\,\frac{dk_n}{d\omega} = \frac{z\,n}{c}\left(1 - \frac{\lambda}{n}\,\frac{dn}{d\lambda}\right) \qquad \text{GD: Group delay}$$

$$\varphi^{(2)} = z\,\frac{d^2k_n}{d\omega^2} = z\,\frac{\lambda^3}{2\pi c^2}\,\frac{d^2n}{d\lambda^2} \qquad \text{GDD: Group delay dispersion or linear chirp}$$

$$\varphi^{(3)} = z\,\frac{d^3k_n}{d\omega^3} = -z\,\frac{\lambda^4}{4\pi^2c^3}\left(3\,\frac{d^2n}{d\lambda^2} + \lambda\,\frac{d^3n}{d\lambda^3}\right) \qquad \text{TOD: Third order dispersion}$$

The first two dispersion parameters influence the phase and group velocity leading only to significant changes in the carrier envelope phase (CEP), which is defined as the phase difference between the carrier wave and envelope maxima. The values for $k_n^{(2)}$ and $k_n^{(3)}$ have been chosen such that a fused silica optical component of 0.5 mm and 5 mm length are simulated, respectively, corresponding to a typical experimental setup.

2.3 Atoms in external laser fields and high–harmonic generation

Free electron lasers (FEL) and the high–harmonic generation (HHG) represent two advanced light sources which provide ultrashort pulses in the femtosecond and attosecond domain with photon energies in the x–ray range. These systems are particularly used to study light–matter interaction on the basis of temporal dynamics and extend the possibilities of conventional ultrashort laser pulses.

In this project a high–harmonic light source was used for ionization experiments on molecular hydrogen. It is therefore appropriate to explain the origin of the HHG and the

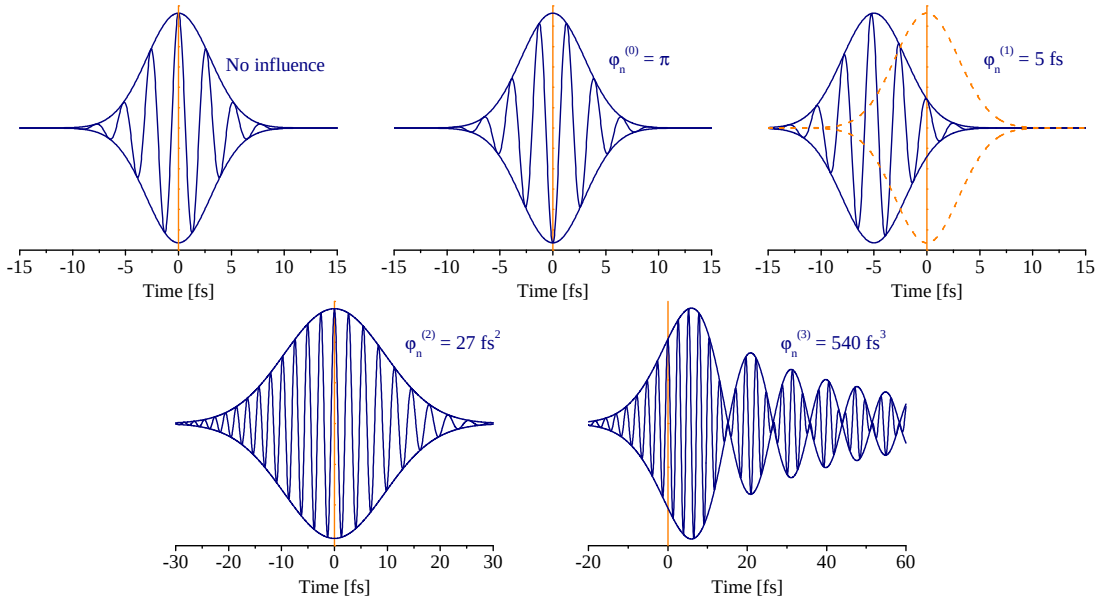

Figure 2.2: A 5 fs pulse is influenced by the first orders of dispersion: $\varphi_n^{(0)}$, $\varphi_n^{(1)}$, $\varphi_n^{(2)}$, $\varphi_n^{(3)}$. The first two parameters $\varphi_n^{(0)}$ and $\varphi_n^{(1)}$ cause a phase shift between the carrier wave and the envelope thus changing the CEP. $\varphi_n^{(2)}$ and $\varphi_n^{(3)}$ both change the pulse duration and $\varphi_n^{(3)}$ further deforms the temporal profile, eventually leading to sub–pulse structures.

most important properties of the resulting pulses. As the HHG follows from strong–field processes in atoms, we will begin the discussion with a few typical phenomena in the high–intensity regime and continue with a simple, semiclassical model on HHG where several characteristics are explainable. Afterwards, the theoretical background will be expanded with quantum mechanical considerations which follow from the strong field approximation (SFA) and the Lewenstein model. Finally, a short comparison between FEL and HHG systems will highlight some advantages and disadvantages of both technologies.

The following section will begin with a discussion on strong field effects for light–atom interactions. The considered high–intensity light source corresponds to focused, ultrashort, infrared (IR) pulses which are technically generated in state–of–the–art femtosecond CPA–laser systems. For these high, but accessible laser intensities, typically in the range of $10^{11} - 10^{15}\,\mathrm{W/cm^2}$, the ponderomotive energy U_p represents the kinetic quiver energy of a classical "free" electron and includes laser parameters, such as the center frequency ω_0 and the intensity I_0 which is proportional to the square of the amplitude F_0^2:

$$U_p = \frac{F_0^2}{4\,\omega_0^2} \quad \text{in atomic units} \qquad\qquad U_p = \frac{e^2\,F_0^2}{4\,m_e\,\omega_0^2} \quad \text{in SI units} \tag{2.12}$$

Another important quantity is the so–called "Keldysh parameter" γ which separates two

competing ionization conceptions, the multi–photon ionization (MPI) for $\gamma > 1$ and electron tunneling for $\gamma < 0.5$ [IDC92] as illustrated in Figure 2.3. γ is defined by the ratio of the electron "tunneling time" t_{tunnel} and the laser period T_0. With a few transformations it is possible to find a relation between γ, the ionization potential I_p and U_p thus combining the most critical atomic and laser dimensions.

$$\gamma = \frac{t_{\text{tunnel}}}{T_0} = \sqrt{\frac{I_p}{2\,U_p}} \tag{2.13}$$

To give an impression for typical, experimental laboratory conditions with an IR laser field, Table 2.1 presents values of U_p, γ and the quiver distance of the free electron resulting for three laser intensities. In these examples, the low and moderate intensities correspond to experimental settings in the reaction microscope, to singly ionize or "probe" atoms and molecules, whereas the high intensity is used for HHG.

Experimental approach	IR–probe pulse in a reaction microscope	Ionization of rare gas atoms	High–harmonic generation
Intensity	$10^{12}\,\mathrm{W/cm^2}$	$5 \cdot 10^{13}\,\mathrm{W/cm^2}$	$10^{15}\,\mathrm{W/cm^2}$
Quiver distance	0.8 Å	5.5 Å	24.8 Å
Ponderomotive potential	0.054 eV	2.7 eV	54 eV
Keldysh parameter	12	1.7	0.38

Table 2.1: Ponderomotive potential, quiver distance of the "free" electron and the Keldysh parameter for several experimental conditions. The considered IR–pulse parameters are: $\tau = 15\,\mathrm{fs}$, $\epsilon = 0.5\,\mathrm{mJ}$ and the central wavelength $\lambda_c = \frac{2\pi c}{\omega_0} = 760\,\mathrm{nm}$. Here, $I_p(\mathrm{Ar}) = 15.8\,\mathrm{eV}$ is used to calculate the corresponding values.

2.3.1 Multi–photon ionization

In the MPI regime ($\gamma > 1$) we consider single photon energies which are not sufficient to ionize atoms; however, if the laser intensity is high enough the probability of simultaneous absorption of a multiple number of photons in a given time Δt increases, eventually enabling ionization [DK99]. In a basic interpretation the electron is excited by each photon to a virtual state without violating the uncertainty principle $\Delta t\,\Delta E \geqslant 1$ with the energy $\Delta E = E_\gamma$. Moreover, it is possible to absorb more photons than necessary for ionization, an effect termed as "Above threshold ionization" (ATI) [Ago+79]. The signature of the ATI process and the dependence of the ionization rate $w \sim I^n$ can be seen in the photoelectron energy spectra, as depicted in Figure 2.3 (a). It must be noted that the strong light field also induces an AC Stark shift to all bound electrons in the atom. The effect is strongest for

the outermost electrons and in particular for the laser–driven, "free" electrons which exhibit the quiver energy U_p. The ionization potential is thus shifted from I_p to $I_p^* \approx I_p + U_p$.

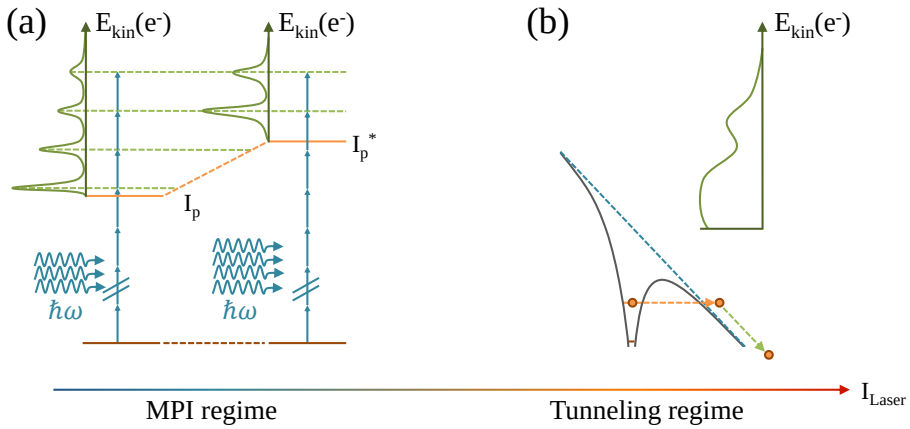

Figure 2.3: (a) Scheme of MPI at two different intensities. The photoelectron energy spectrum features ATI peaks. The ionization threshold I_p is shifted to I_p^* for higher laser intensities due to the Stark effect. (b) Electron tunneling at even stronger IR–light fields. Here, ATI peaks are not encountered in the photoelectron–energy distribution.

2.3.2 Tunnel–ionization and ADK model

At intensities where the electric field of the irradiating light becomes comparable to the Coulomb field between core and electron, the resulting atomic potential appears strongly distorted as depicted in Figure 2.3 (b). In this case, the possibility of an electron tunneling through the considerably slowly varying potential increases drastically. This can also be expressed in terms of an associated electron tunneling time which is short in comparison to the oscillation of the laser field and corresponding potential well.

For both ionization types, the MPI and the tunneling, the ionization rate w can be calculated within the frame of the Perelomov, Popov and Terent'ev (PPT) model; however, in the tunneling regime a simpler expression for the ionization rate is given by the "ADK" formula [ADK86; DK91]

$$w_{\mathrm{ADK}}(t) \quad = \quad |C_{n^*l^*}|^2 \; G_{lm} \, I_p \left(\frac{2(2I_p)^{3/2}}{E(t)} \right)^{2n^* - |m| - 1} e^{-\frac{2(2I_p)^{3/2}}{3\,E(t)}} \quad , \tag{2.14}$$

with the ionization potential I_p and the electric field $E(t)$. The coefficients $|C_{n^*l^*}|^2$, G_{lm} can be calculated from the electron quantum numbers l, m and the effective quantum numbers n^*, l^* and, thus, contain the information of the initial atomic state [Chi04]. This equation; however, underestimates the ionization rate at high γ towards the MPI regime by orders of magnitude.

2.4 High–harmonic generation

In linear polarized and highly–intense IR–laser fields, the tunneling electrons are driven back and forth in an oscillatory motion. Some of the electrons come back to the vicinity of the nucleus and scatter elastically or inelastically with bound electrons. In addition, a recombination processes may occur where the kinetic energy, which the electron gained in the laser field, is converted into a photon. The emitted photons have energies in the x–ray regime and the properties of the corresponding light field can be explained via a semiclassical model.

2.4.1 Semiclassical model

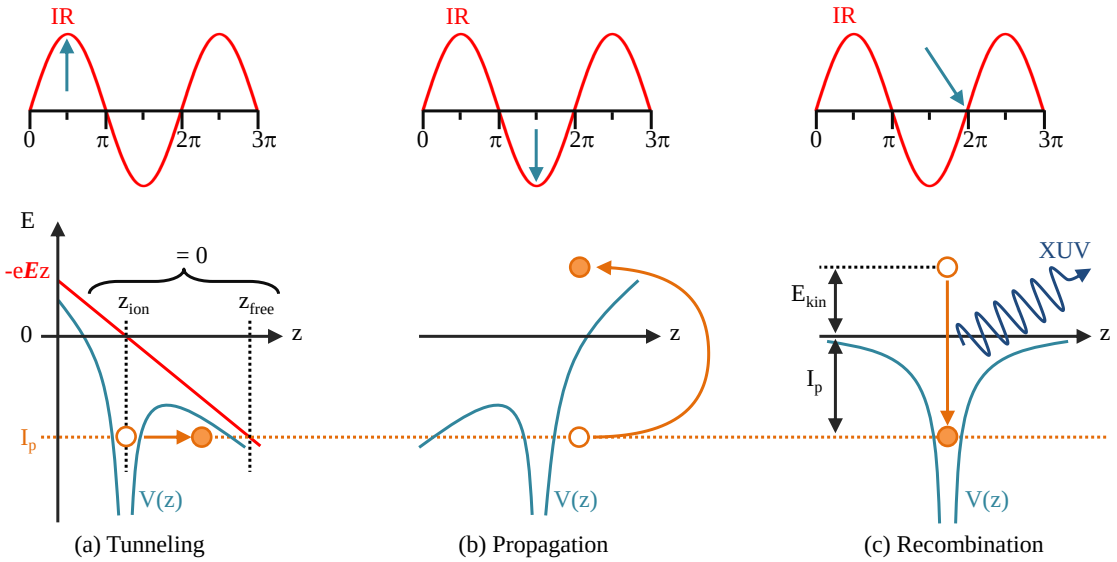

Figure 2.4: Semiclassical model in three steps: (a) Tunnel ionization. (b) Acceleration and propagation of the free electron in the external field. (c) Recombination and emission of an XUV photon.

The semiclassical model, developed by Corkum and Kulander in 1993, describes the generation of attosecond pulses or high–harmonic light in three steps [Cor93], illustrated in Figure 2.4. The following treatment, which is adapted from [Cha11], is performed in one dimension (z) and uses a linear polarized light field in the same direction. Furthermore, the process is analyzed mainly within one or two laser cycles $T_0 = 2\pi/\omega_0$, for which reason the envelope function $F(t)$ shall be considered as constant in time:

$$E(t) \quad = \quad F(t)\,\cos(\omega_0 t) \quad = \quad F_0\,\cos(\omega_0 t) \tag{2.15}$$

In the first step, an electron tunnels through the Coulomb barrier, which is lowered by

the strong field of the fundamental IR pulses at intensities where the Keldysh parameter is below 0.5. Electron tunneling is a quantum process and the properties of the emitted electron wave function must be taken into account; however, for simplicity it is presumed that the tunneling happens instantaneously and that the electron features zero velocity at the position $z \approx 0$. The second step considers the classical motion of the point–like electron in the electric field:

$$\frac{d^2z}{dt^2} \quad = \quad -F_0 \cos(\omega_0 t) \tag{2.16}$$

Assuming that the electron is released at a time t', the integration yields the velocity and position of the particle with maximum values $v_{\max}$ and $x_{\max}$:

$$v(t) = -v_{\max}\left[\sin(\omega_0 t) - \sin(\omega_0 t')\right] \qquad v_{\max} = \frac{F_0}{\omega_0} \tag{2.17}$$

$$z(t) = -z_{\max}\left(\left[\cos(\omega_0 t) - \cos(\omega_0 t')\right] + \omega_0 \sin(\omega_0 t')\,(t - t')\right) \qquad z_{\max} = \frac{F_0}{\omega_0^2} \tag{2.18}$$

In the third step, the electron recombines with its parent ion and emits a photon which contains the energy of the ionization potential and the kinetic energy of the electron, gained by the interaction with the external light field:

$$E_\gamma(t) \quad = \quad I_p + \frac{1}{2}v^2(t) \quad = \quad I_p + 2\,U_p\left[\sin(\omega_0 t) - \sin(\omega_0 t')\right]^2 \tag{2.19}$$

The kinetic energy can be expressed by the previously introduced ponderomotive potential U_p. With this small set of equations it is already possible to explain some general features of the XUV radiation such as spectral and temporal profile and the maximum energy of the photons. Therefore, it is necessary to determine the time t_r, for which the electron recombines with the ion, thus fulfilling $z(t_r) \stackrel{!}{=} 0$ in equation (2.18). Solutions for this problem can be found numerically as well as graphically in the so–called Kramers–Henneberger frame of reference where the parent ion moves periodically such that the electron displacement to it is described as a linear function. To emphasize the significant features, it is sufficient to use the following approximate expression for t_r [Cha11]:

$$t_r(t') \quad = \quad T_0\left(\frac{1}{4} - \frac{3}{2\pi}\arcsin\left(4\,\frac{t'}{T_0} - 1\right)\right) \tag{2.20}$$

The corresponding curve is represented in Figure 2.5 (a). Note that no recombination occurs for electron release times between 0.25 and $0.5\,T_0$. This confinement explains the pulse train structure of the higher harmonics with the generation of single pulses every half cycle of the fundamental laser field.

The photon energy function, presented in Figure 2.5 (b), and the maximum possible

photon energy $E_{\gamma\,\mathrm{max}}$ are obtained by inserting equation (2.20) into (2.19):

$$E_\gamma(t') = I_p + 2\,U_p\left[\sin\left(\frac{\pi}{2} - 3\,\arcsin\left(\frac{2}{\pi}\,\omega_0\,t' - 1\right)\right) - \sin\left(\omega_0 t'\right)\right]^2 \quad (2.21)$$

$$E_{\gamma\,\mathrm{max}} \approx I_p + 3.17\,U_p \quad (2.22)$$

Here, $E_{\gamma\,\mathrm{max}}$ is encountered for electrons with an emission at $t' \approx 0.05\,T_0$ and a recombination time $t_r \approx 0.7\,T_0$. Note, for each XUV photon energy (except for the maximum kinetic energy) there exist an early and a late electron release time, t'_1 and t'_2, which according to Figure 2.5 (a) are connected to a late and early recombination times, t_{r1} and t_{r2}, respectively. This implies two time intervals $(t_{r1} - t'_1)$ and $(t_{r2} - t'_2)$ which are interpreted as a long and a short trajectories. In a HHG experiment, the short trajectories are favorable as the corresponding XUV photons feature less divergence. Moreover, the different trajectories introduce a slight dispersion to the emitted XUV light pulse, though with opposite sign, for which reason a suppression of the long trajectories by phase matching conditions and spatial filtering is usually applied. The attosecond nature of the pulses that

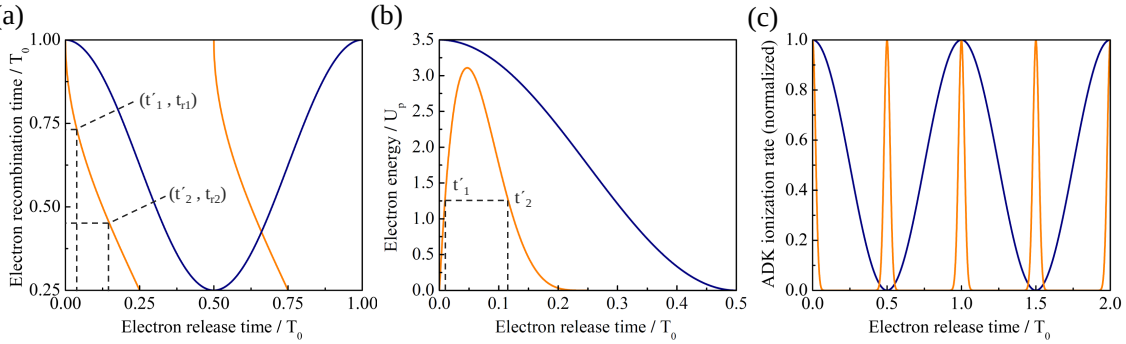

Figure 2.5: (a) Recombination time t_r, (b) kinetic energy of the electron and (c) ADK ionization rate w_{ADK} as a function of the electron release time t'. The normalized cosine electric field is shown as a blue curve in all diagrams.

are confined within one pulse train are described by the ionization rate w_{ADK} in equation (2.14) as a function of the electron release time t', as shown in Figure 2.5 (c). Even though the long trajectories make a larger contribution to the ionization, the interesting events are related to the short trajectories. These are confined to electron release times between $0.05\,\mathrm{T_0}$ and $0.1\,\mathrm{T_0}$. The resulting recombination times t_r are identified as $0.5\,\mathrm{T_0}$ to $0.7\,\mathrm{T_0}$ and, thus, corresponding to 330 as for the generated XUV pulses.

The semiclassical model demonstrates, how short attosecond pulses in the XUV range are generated at every half cycle of the fundamental laser with a temporal spacing of $T_0/2$. Spectral interference finally gives rise to the odd harmonic energies (of the fundamental, XUV–generating laser beam) and their spacing by $2\,\omega_0$. Nevertheless, it must be emphasized that the XUV light emission is a quantum process which is not included in the

semiclassical model, consequently it does not reveal correct amplitudes and phases.

A quantum mechanical, analytical solution for the HHG process was found by Lewenstein et al., using the concept of strong field approximation (SFA) [Lew+94]. The SFA considers a direct electron transition from the ground state to the continuum states without including any resonance processes via excited states. This restriction thus works in the tunneling regime for $\gamma < 0.5$ where the free electron is driven far enough from its parent ion (quiver distance $\sim$ 2 nm), such that the Coulomb potential of the ion is negligible during the acceleration of the electron and the turning point. In this approach, only the light field is treated classically. The generation of the higher harmonics is interpreted as an interference of two components of the electron wave function, a bound and an ionized part, which lead to a fast oscillating dipole moment.

2.4.2 Comparison between high–harmonic generation and free electron lasers

Free electron lasers (FELs) facilities are becoming progressively important in many branches of natural sciences. There are several reasons for this development as the light properties expand the experimental possibilities in many aspects. Especially in comparison to HHG, the FEL pulses provide much higher values for single pulse energy, output power and average as well as peak brilliance, thus enabling multiphoton processes in the XUV range. The tunability of important parameters, such as wavelength and pulse duration is a another evidence for the strength of this technology.

Nevertheless, HHG systems also offer several advantages, of which the most important is probably the synchronization with the generating IR laser. As the phases of the IR and the XUV pulses are correlated inherently by the phase matching condition in the generation process, the possibility to perform pump–probe measurements on a sub–IR–cycle basis becomes much easier. Another pivotal difference is related to the higher repetition rate and the comparatively high reproducibility, concerning the temporal pulse shape, including phase, peak intensity and sub–pulses structures which in most FELs vary from pulse–to–pulse. Furthermore, HHG sources are realized in table–top setups, thus offering longer beam times and higher statistics in the data sets which often is a crucial aspect for measurements with reaction microscopes.

Today, there are several new developments in FEL systems which are able to compensate some of the mentioned drawbacks. A promising concept is to initiate the SASE[1] process with an external co–propagating seed field from an unfiltered HHG source [Hzb]. By this, the electrons are coupled to a stable external XUV–light field and the resulting temporal and spectral profiles of the FEL pulses become more uniform.

[1] The FEL pulses are generated by an electron beam which passes through an undulator with alternating magnetic fields, forcing the electrons on sinusoidal trajectories. Without an external field, the lasing in the FEL is initiated by spontaneous emission of the electrons and the amplification results from interaction between electrons and the emitted x–ray radiation [Lei07].

3 Molecular hydrogen in light fields

In the past, experiments exploring the generation of high–harmonic radiation mainly concentrated on technical aspects, such as increasing the yield and the spectral range or reducing the XUV pulse duration by gating techniques [Sol+06; San+06; Mas+08]. Moreover, interesting features found and studied in atom–light interactions turned out to enable the detailed characterization of the high–harmonic radiation as well as of its generating IR field [MQ05; Tza+03; Pau+01].

Based on this remarkable technological progress, these new XUV–light fields with their unprecedented spectral and temporal properties can now be applied to study small, few–atom molecules opening new possibilities to explore photon–induced ionization or excitation on a time–dependent basis. Particularly interesting in this context are electron–electron correlations and the coupling of correlated electronic motion to the nuclear wave–packet dynamics, which both are also subjects of state–of–the–art quantum calculations. Even small molecules open a huge playground since they exhibit many degrees of freedom with respect to the corresponding transition probabilities. For a simple, diatomic molecule, scheme [3.1] indicates that rotational, vibrational and electronic levels cover large energy ranges from a few µeV up to several eV and the corresponding transition times extend between picoseconds and attoseconds.

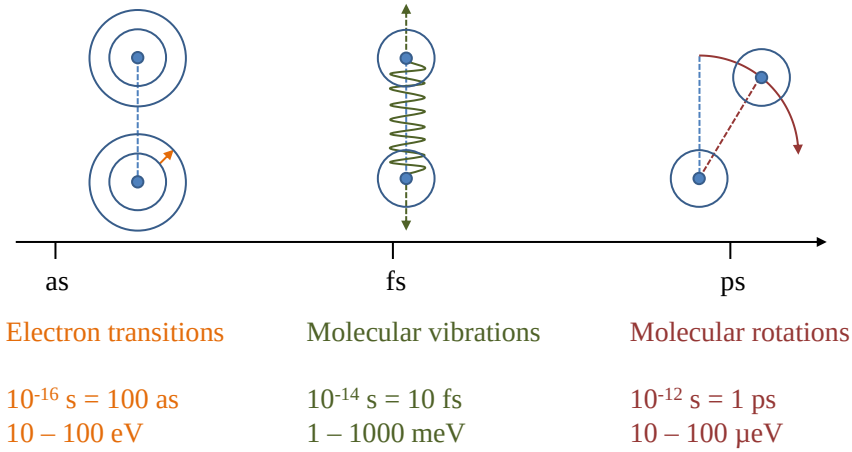

Figure 3.1: Dynamics with typical timescales in simple molecules, containing electronic, vibrational and rotational lifetimes.

The following sections will present some basics about the description of electronic states,

molecular symmetries and photon–induced transitions and apply the concepts on the hydrogen molecule H_2 and its associated ion H_2^+. Furthermore, doubly excited states of H_2 will be elucidated, and associated processes such as autoionization and dissociation.

3.1 Molecular hydrogen

Molecular hydrogen and its corresponding ion are the simplest homopolar molecules and belong to the class of covalent bonded systems. In this section, the basic principles on calculating electron and nuclear wave functions and corresponding energies are introduced. Furthermore, there will be a discussion on dipole–allowed transitions, as well as on the concept of symmetry of states, which represents one of the most powerful tools to theoretically characterize molecular systems.

3.1.1 Born–Oppenheimer approximation and potential energy surfaces

The Born–Oppenheimer approximation is a theoretical method to simplify the Schrödinger equation (3.1) for quantum systems, which contain heavy and light particles; consequently, it is well suited for the theoretical description of molecules [BO27].

$$\hat{\boldsymbol{H}}\,\psi \;=\; E\,\psi \tag{3.1}$$

The simplification is based on the assumption, that the nuclear movement in molecules, consisting of comparably slow vibrational and rotational dynamics, is separable from the electronic motion [Gri05]. Therefore, the core is usually considered to be stationary, while the electronic state adapts to the current nuclear configuration. Following these arguments, the Hamiltonian of the Schrödinger equation for H_2 (equation (3.2)) and H_2^+ (equation (3.3)) can be reduced by ignoring the kinetic energy parts of the nuclei, and evaluating the electronic part of the Schrödinger equation for a parametrically varying geometrical configuration which in the case of diatomic molecules is equal to the internuclear distance $\boldsymbol{R}_{AB}$.

$$\begin{aligned}\hat{\boldsymbol{H}}_{H_2} \;=\; &-\frac{1}{2}\nabla_{e1}^2 - \frac{1}{2}\nabla_{e2}^2 - \frac{1}{2\mu}\nabla_A^2 - \frac{1}{2\mu}\nabla_B^2 - \\ &- \frac{1}{\boldsymbol{r}_{1A}} - \frac{1}{\boldsymbol{r}_{1B}} - \frac{1}{\boldsymbol{r}_{2A}} - \frac{1}{\boldsymbol{r}_{2B}} + \frac{1}{\boldsymbol{R}_{AB}} + \frac{1}{\boldsymbol{r}_{12}}\end{aligned} \tag{3.2}$$

$$\hat{\boldsymbol{H}}_{H_2^+} \;=\; -\frac{1}{2}\nabla_{e1}^2 - \frac{1}{2\mu}\nabla_A^2 - \frac{1}{2\mu}\nabla_B^2 - \frac{1}{\boldsymbol{r}_{1A}} - \frac{1}{\boldsymbol{r}_{1B}} + \frac{1}{\boldsymbol{R}_{AB}} \tag{3.3}$$

Here, A and B denote the two nuclei, positions are defined in Figure 3.2, $\mu = \frac{M_A \cdot M_B}{M_A + M_B}$ is the reduced mass and atomic units (au) with $m_e = \hbar = e = 1/4\pi\epsilon_0 = 1$ are used

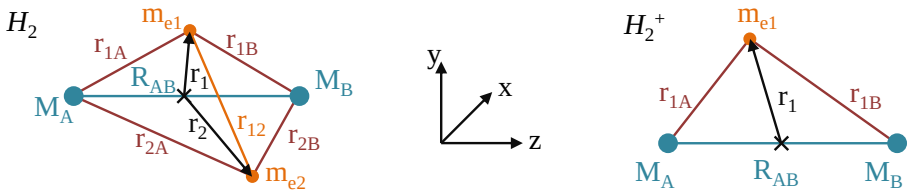

Figure 3.2: Coordinates and masses for the H_2 and H_2^+ molecules. The center of each molecule is marked with **x**.

throughout[1]. The result for each electronic state is a potential energy surface (PES) as a function of the nuclear geometry or in the simple case of H_2 and H_2^+ a potential energy curve which is represented by the electronic energy as a function of the internuclear distance, see Figure 3.3. Such states can be binding and stable, but they can also be repulsive, which means, that the molecule will fragmentize into smaller molecules or atoms. For the molecular hydrogen states, a binding PES exhibits an absolute minimum energy

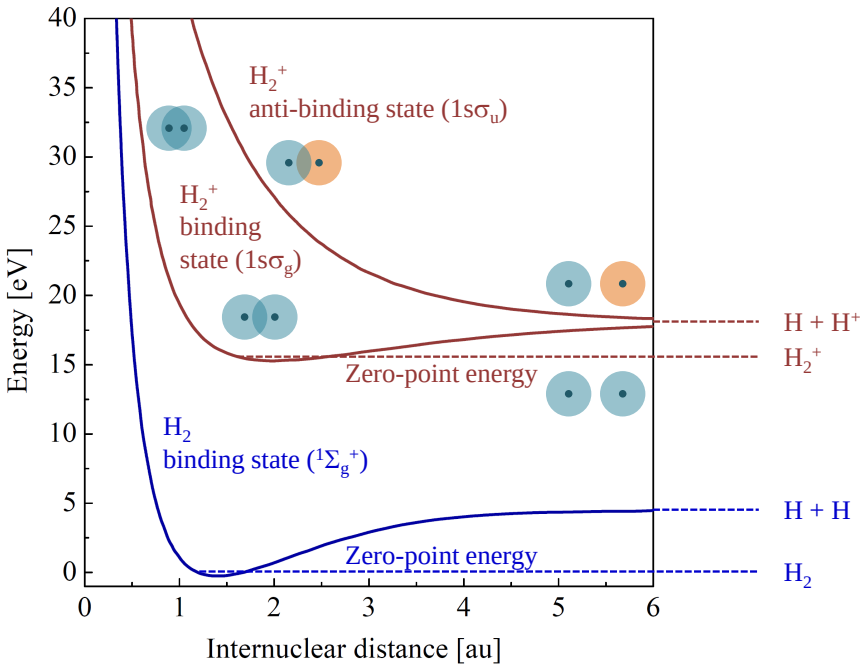

Figure 3.3: A selection of important potential energy curves of H_2 (blue) and H_2^+ (red) as a function of the internuclear distance R_{AB}. Furthermore, the zero-point energy is shown for both molecules, as well as the dissociation limit for large internuclear distances. For completeness, the linear combination of atomic orbitals is indicated for both presented PES of H_2^+ at different internuclear distances.

[1] The relation between SI and atomic units is presented in Table 7.1. Note, e: Elementary charge, m_e: Electron mass, $1/4\pi\epsilon_0$: Coulomb constant, $\hbar$: Planck constant.

at a specific equilibrium distance of the two protons. Larger and more complex molecules often feature multidimensional PES depending on the amount of geometrical parameters and they can exhibit global and local minima, thus giving rise e.g. to isomerization.

It is important to note, that the Born–Oppenheimer approximation allows a separation of stationary or even some time–dependent molecular problems into two independent Schrödinger equations and corresponding wave functions, one for the electrons ψ_{es} and another one for the core dynamics ψ_{v}. It turns out that the electron energy which is represented by a specific potential energy surface, forms the potential, in which the atomic constituents of the molecule move [HS10]. Vibrational energy levels of the cores can thus be found within the the limits of the binding curves. In the case of H_2 and H_2^+, both binding ground state PES feature an anharmonic profile (see Figure 3.3). Thus, the energy spacing between two of the corresponding vibrational states will decrease with increasing energy, in contrast to a harmonic potential. Even if this decrease of level–energy spacing with increasing quantum number is in analogy with the properties of an atomic Coulomb potential, the anharmonic PES only exhibit a finite number of vibrational states, 15 and 20 for the ground state of H_2 and H_2^+, respectively [BHP70; Sha70].

3.1.2 Linear combination of atomic orbitals (LCAO) and molecular orbitals (MO) for H_2 and H_2^+

The Born–Oppenheimer approximation and the neglect of spin–orbit coupling allows the separation of the molecular wave function into a nuclear, an orbital and a spin related part

$$\psi \equiv \psi_{\mathrm{ves}} = \psi_{\mathrm{v}}(\boldsymbol{R}_{AB})\,\psi_{\mathrm{e}}(\boldsymbol{r}_1,\boldsymbol{r}_2)\,\psi_{\mathrm{s}}(\alpha,\beta) \tag{3.4}$$

with the internuclear distance $\boldsymbol{R}_{AB}$, the electron coordinates $\boldsymbol{r}_1$ and $\boldsymbol{r}_2$ (see Figure 3.2) and spin variables where α and β represent spin–up and spin–down. Here, we want to begin with a description of a two–electron orbital wave function $\psi_{\mathrm{e}}(1,2)$ of the hydrogen molecule, using an intuitive ansatz by the generalized representations of Heitler–London [HL27] and Mullikan–Bloch [Mul75]. In both approaches, the orbital wave function $\psi_{\mathrm{e}}(1,2)$ consists of a linear combination of ground–state atomic wave functions $\phi_{A,B}$ of the electrons $(1,2)$ which are indistinguishable and located at the two atomic cores (A,B).

$$\psi_{\mathrm{e}}(1,2) = c\left[\phi_A(1)\,\phi_B(2) \pm \phi_A(2)\,\phi_B(1)\right] \pm d\left[\phi_A(1)\,\phi_A(2) \pm \phi_B(1)\,\phi_B(2)\right] \tag{3.5}$$

In equation 3.5 the three algebraic signs ($\pm$) are independent from each other and denote all possible combinations of the ground–state atomic wave functions. The parameters c and d account for two oppositional configurations, where either each electron is located preferentially around one nucleus ($c > d$) or where both are placed together around one nucleus ($c < d$) [Dem95]. Hereby, the first and second configuration correspond to a covalent and to an ionic bond, respectively [HG05]. This construction of molecular orbitals can be

extended to a linear combination of ground and excited states, provided that the states exhibit the same symmetry with respect to the molecular axis[2].

The next step in the description of the total molecular wave function involves the Pauli principle, which demands an anti–symmetric configuration with respect to an exchange of the electrons. The vibrational part is considered to be symmetric [Eng96], for which reason the two–electron wave function $\psi_{\mathrm{es}}(1,2) = \psi_{\mathrm{e}}(1,2) \cdot \psi_{\mathrm{s}}(1,2)$ has to be antisymmetric.

As $\psi_{\mathrm{e}}(1,2)$ from the expression (3.5) is neither symmetric nor antisymmetric with respect to electron exchange, a modification becomes necessary. In a first approximation, the parameters c and d can be set to 1, enabling a simple rearrangement of the orbital wave function to two purely symmetric (g for "gerade", if the algebraic sign is $+$) or antisymmetric (u for "ungerade", if the algebraic sign is $-$) single–electron configurations.

$$\begin{aligned} \psi_{\mathrm{e}}(1,2) &= \phi_A(1)\,\phi_B(2) \pm \phi_A(2)\,\phi_B(1) \pm \phi_A(1)\,\phi_A(2) \pm \phi_B(1)\,\phi_B(2) \\ &= \big(\phi_A(1) \pm \phi_B(1)\big) \cdot \big(\phi_A(2) \pm \phi_B(2)\big) \\ &= \phi_{g,u}(1) \quad \phi_{g,u}(2) \end{aligned} \tag{3.6}$$

A linear combination of the single–electron orbital wave functions can then be used to achieve symmetric or antisymmetric configurations and fulfill the Pauli principle[3]. As an example, the ground state as well as the first two excited states of H_2 are represented by the following functions, with α and β reflecting spin–up and spin–down, respectively:

$$\psi_{\mathrm{es}}(1,2)\,(^1\Sigma_g^+) = \frac{1}{2}\,[\phi_g(1)\,\phi_g(2) + \phi_g(1)\,\phi_g(2)]\,\,[\alpha(1)\,\beta(2) - \alpha(2)\,\beta(1)] \tag{3.7}$$

$$\psi_{\mathrm{es}}(1,2)\,(^3\Sigma_u^+) = \frac{1}{2}\,[\phi_g(1)\,\phi_u(2) - \phi_u(1)\,\phi_g(2)]\,\,[\alpha(1)\,\beta(2) + \alpha(2)\,\beta(1)] \tag{3.8}$$

$$\psi_{\mathrm{es}}(1,2)\,(^1\Sigma_u^+) = \frac{1}{2}\,[\phi_g(1)\,\phi_u(2) + \phi_u(1)\,\phi_g(2)]\,\,[\alpha(1)\,\beta(2) - \alpha(2)\,\beta(1)] \tag{3.9}$$

It should be mentioned that the first excited state ($^3\Sigma_u^+$) is threefold degenerate, since $[\alpha(1)\,\alpha(2)]$ as well as $[\beta(1)\,\beta(2)]$ are equally valid as symmetric spin wave functions. Ultimately, transitions from the ground state ($^1\Sigma_g^+$) to this particular state are strictly forbidden within the limits of the dipole approximation. The corresponding selection rules as well as the applied spectroscopic notation will both be explained within the next two sections.

3.1.3 Symmetry

As pointed out earlier, symmetry considerations constitute an important concept in the description of molecular orbitals, vibrations, transitions and electron partial waves in

[2] Otherwise the "overlap" integrals, such as $\int \phi_A(1)\phi_B(1)$ become zero and the energy of the state diverges.
[3] Note, the geometrical symmetry properties of molecular orbitals which are denoted with g and u are not the determining factors for the anti–symmetrizing of the two–electron wave function.

ionization processes [HW05]. Especially for large molecules with linear, planar or three–dimensional structures which are invariant under symmetry operations, the theoretical treatment can be simplified drastically; nevertheless, only the H_2 and H_2^+ will be considered here.

The mathematical principle of symmetry is based on group theory, where point groups reflect the symmetry properties of a molecule and the molecular orbitals [Sen09]. These point groups are usually characterized by a set of symmetry operations and corresponding irreducible representations. Homonuclear, diatomic molecules belong to the $D_{\infty h}$ point group and, thus, feature two important symmetry operations which are used to specify the wave function of the states:

- Inversion of the molecule (or an orbital wave function) through the center of the internuclear bond axis, here along the z–coordinate (see Figure 3.2).
- Reflection of the molecule (or an orbital wave function) on a plane containing the internuclear bond axis.

Symmetric and antisymmetric wave functions following from these operations are termed as "gerade (g)" or "ungerade (u)" and, accordingly, "positive ($+$)" or "negative ($-$)". The following definitions (3.11)–(3.13) show the presented inversion and reflection operations together with the corresponding wave functions for homonuclear molecules.

$$\psi_g(\boldsymbol{r}) = +\psi_g(-\boldsymbol{r}) \quad \text{gerade state} \tag{3.10}$$

$$\psi_u(\boldsymbol{r}) = -\psi_u(-\boldsymbol{r}) \quad \text{ungerade state} \tag{3.11}$$

$$\psi^+(x,y,z) = +\psi^+(-x,y,z) \quad \text{positive state} \tag{3.12}$$

$$\psi^-(x,y,z) = -\psi^-(-x,y,z) \quad \text{negative state} \tag{3.13}$$

A key property of this concept is, that all observables as well as the Hamiltonian have to be invariant under operations belonging to the symmetry group. Additional symmetry operations and denominations exist for more complex molecular structures, which is discussed in detail in [Eng96] and [HW05].

3.1.4 Spectroscopic notation and quantum numbers

In general there are two possibilities to refer to a certain electronic molecular state, by assigning all electrons separately a set of quantum numbers or by regarding the complete electron compound. Both description will be presented briefly for H_2 and H_2^+, since they are often used in literature.

In contrast to atoms, linear molecules, such as H_2 and H_2^+, feature a cylindrical symmetry due to the internuclear axis. As a consequence, the Hamiltonian $\hat{\boldsymbol{H}}$ and $\hat{\boldsymbol{L}}^2$ do not commutate and, thus, the orbital angular momentum quantum number l does not fulfill

the properties of a "good" quantum number. This is not the case for the eigenvalues of the projection of l on the molecular axis $l_z = \lambda\hbar$ which is therefore used to characterize one–electron states. Furthermore, the state notation can be completed specifying the (g, u) symmetry of the molecular orbital. The full representation of a single electron state includes the spectroscopic notation of the atomic orbitals that define the molecular state within the frame of LCAO. In that regard, the lowest electronic states in H_2^+ are written as $(1s\sigma_g)$ for the binding and $(1s\sigma_u)$ for the antibinding states. In literature the $(1s\sigma_u)$ is often referred to as $(2p\sigma_u)$, due to its wave function shape which in the limits of combined atoms resembles a $2p$–wave.

A complete spectroscopic notation of the electron configuration in a diatomic molecule includes all electrons and is characterized by the projection of the total orbital angular momentum onto the internuclear axis ($L_z = \Lambda\hbar$). In addition, the combination of electron spins is given by the multiplicity $2S + 1$, denoting, if the corresponding two–electron level is either a singlet or a triplet state. Furthermore, the previously introduced symmetry representations (g, u) and $(+, -)$ are included in the notation of the states. In summary, the electronic states in molecules are expressed as ${}^{2S+1}\Lambda_{g,u}^{+;-}$ and they can additionally be labeled with ascending capital letters $(X, A, B, C, \ldots)$, whereby the ground state is easily identified by a precedent X and doubly–excited states are termed as Q_n.

Classification label	(X, A, B, C, Q_n, ...)
Projection of total orbital angular momentum Λ	(Σ, Π, Δ, Φ, ...)
Symmetry indices	(g, u and $+$, $-$)

As an example, the lowest electronic state in H_2 can be written as $X\,{}^1\Sigma_g^+$ and the two lowest states of H_2^+, introduced in the previous paragraph by the single–electron notation $(1s\sigma_g)$ and $(1s\sigma_u)$ now become ${}^2\Sigma_g^+$ and ${}^2\Sigma_u^+$.

It should be mentioned that a full description also includes the total angular momentum of the molecular system. However, the spin–orbit coupling as well as the coupling to the nuclear spin can be effected in many ways such that a discussion on this goes beyond the scope of this work (the interested reader is referred to the five coupling cases of Hund, explained, for instance, in [Hou]).

3.1.5 Relevant electronic states in H_2 and H_2^+

In Figure 3.4, PES from relevant states of H_2 and H_2^+ are presented in a combined diagram with the typical spectroscopic notation. For the binding states, a few vibrational energy levels are also indicated. Furthermore, some exemplary curves of the two lowest energetic series of doubly–excited states in molecular hydrogen are shown as well. Note, that they are all repulsive.

The dynamics of doubly excited atoms and molecules is very difficult to describe by

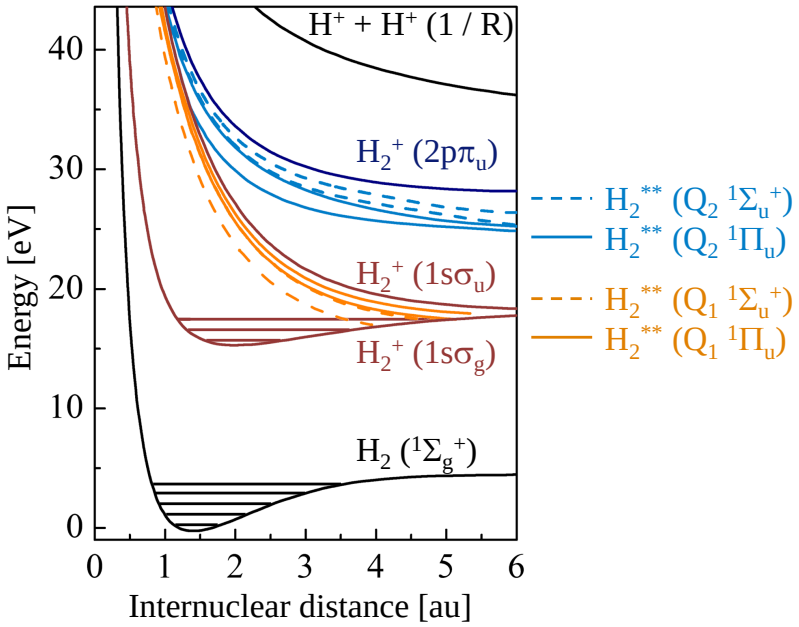

Figure 3.4: PES of H_2 ground state (black), H_2^{**} (orange for Q_1 and light blue for Q_2) and H_2^+ (red for $(1s\sigma_g)$, $(1s\sigma_u)$ and blue for $(2p\pi_u)$). All curves are adapted from [FM09].

theory, because the two excited electrons are highly correlated. In the case of H_2 this is even more challenging, as the nuclear motion, which is manifested in the dissociation of the molecule, must be included in calculations, thus going beyond the Born–Oppenheimer approximation. In ionization processes, doubly–excited states also play an important role as intermediate states in single– and multi–photon absorption [SM97; SM99b], leading to localization effects of electron wave packets, which will be demonstrated in chapter 5.

As indicated earlier, doubly–excited states are combined in classes termed as Q_n which are defined by the lower energetic electron which in the limit of separate atoms would occupy a specific excited state with principle quantum number n. The second electron hereby occupies a state which lies between n and the ionization threshold. Hence, Q_n states can be considered as a Rydberg series or even band like structures. In this context, the $(1s\sigma_u)$ and $(2p\pi_u)$ potential curves denote the ionization limits of the Q_1 and Q_2 series, respectively.

In molecular hydrogen, all doubly–excited states are embedded and coupled to the singly–ionized electronic continuum through electron–electron correlation, for which reason these states autoionize with a high probability [SRM12]. Furthermore, the states are highly dissociative, with fragmentation products including two neutral H atoms, H^- and H^+ ions and a neutral atom together with a proton. During dissociation, both particles usually gain a certain amount of kinetic energy which in literature is referred to as "kinetic energy release" or simply KER. Including autoionization, where an electron is emitted, the

following four channels can be distinguished:

$$
\begin{aligned}
H_2^{**}(Q_n) &\xrightarrow{\text{dissociation}} H + H \\
H_2^{**}(Q_n) &\xrightarrow{\text{dissociation}} H^+ + H^- \\
H_2^{**}(Q_n) &\xrightarrow{\text{autoionization}} H_2^+ + e^- \\
H_2^{**}(Q_n) &\xrightarrow[\text{dissociation}]{\text{autoionization}} H + H^+ + e^-
\end{aligned}
$$

Usually autoionizing states are short lived and, in the case of H_2, their lifetimes τ_{AI} are comparable to the time scale of nuclear dynamics ($2 - 12\,\text{fs}$). In this context they are theoretically described as resonances rather than normal bound states. It is important to note that the autoioniation lifetimes strongly vary with internuclear distances and symmetries, as shown in Figure 7.1 in the appendix. At an internuclear distance of 1.5 au within the so–called Franck–Condon region of H_2 (see section 3.2.3), for example, τ_{AI} for the Q_1 ($1^1\Sigma_u^+$) state is 1.4 fs, whereas for Q_1 ($1^1\Pi_u$) state it corresponds to 92 fs.

For the autoionization events investigated within this work, the H_2 merges from the Q_1 or Q_2 states to the binding and antibinding H_2^+ ground states ($1s\sigma_g$) and ($1s\sigma_u$). In the first case, if the autoionization happens fast with a small associated KER, the molecular ion remains in a stable final state [San+12].

A selection of relevant states in H_2^{**} and H_2^+ are listed in the appendix 7.2 with the corresponding spectroscopic notation. The photo–excitation cross sections of the lowest doubly excited Q_1 and Q_2 as well as H_2^+ states are presented in [GMS05], including the probabilities of possible fragmentation channels. Double excited states of particular relevance, such as the Q_2 ($1^1\Pi_u$) which autoionizes either to ($1s\sigma_g$) or ($1s\sigma_u$), are explained in detail in [SM99a; SM99c].

3.2 Molecules in XUV laser fields

Photons from synchrotrons and, more recently, from free electron lasers and HHG–light sources are widely used in spectroscopy to study the structure and dynamics of molecules, but the resulting spectra are often difficult to interpret, as electron transitions also involve excitations of molecular vibrations and rotations. For molecular hydrogen, the following sections will thus give an overview and explain some of the measured XUV–photon induced effects, presented in chapter 5.

3.2.1 Selection rules for dipole–allowed transitions in H_2 and H_2^+

Single XUV–photon absorption by molecules can be described within the limits of the dipole approximation; however, symmetry considerations must be taken into account to determine if transitions are allowed or not. In addition to explaining possible transitions

to explicit excited or ionic states, the concept of symmetry enables understanding of the emission characteristics of electronic partial waves occuring as a result of photoionization and autoionization [AF05].

According to the Born–Oppenheimer approximation, electronic transitions can be viewed as being instantaneous compared to any substantial vibrational changes, since electron dynamics is usually by many orders of magnitude faster. As described before, under these circumstances it is reasonable to separate the wave functions of H_2 and H_2^+ into an electronic and a nuclear part. Furthermore, it is possible to split the electronic wave function by neglecting spin–orbit coupling, such that the corresponding matrix element for an electronic transition (e $\rightarrow$ e'), including molecular vibration and rotation ($\nu \rightarrow \nu$') and the spin of the electron (s $\rightarrow$ s') can be written as follows:

$$\begin{aligned} M_{\nu\text{'e's'}\,\nu\text{es}} &\sim \langle\, \psi_{\nu\text{'e's'}} \mid \hat{\mu} \mid \psi_{\nu\text{es}} \,\rangle \\ &\sim \langle\, \psi_{\nu\text{'}} \mid \psi_{\nu} \,\rangle \quad \langle\, \psi_{\text{e'}} \mid \hat{\mu} \mid \psi_{\text{e}} \,\rangle \quad \langle\, \psi_{\text{s'}} \mid \psi_{\text{s}} \,\rangle \end{aligned} \tag{3.14}$$

The separation into a product of three wave functions motivates the first selection rule, related to the spin:

$$\langle\, \psi_{\text{s'}} \mid \psi_{\text{s}} \,\rangle \quad = \quad \delta_{\text{s's}} \qquad \Rightarrow \qquad \Delta(S) \,=\, 0 \tag{3.15}$$

A general rule that applies to photon–induced transitions in molecules, is that the total symmetry, containing symmetries of the initial $|\psi_{\nu\text{es}}\rangle$ and final state $|\psi_{\nu\text{'e's'}}\rangle$ as well as of the dipole operator $\hat{\mu}$, must include the fully symmetric irreducible representation of the point group which, in the case of homonuclear molecules, is given by Σ_g^+.

Analyzing the electron transition integral in equation (3.14) shows that the symmetry between ψ_{e} and $\psi_{\text{e'}}$ has to change. This can be seen more clearly in terms of a direct, multiplicative operation of the irreducible representations or state symmetries $\Lambda_{g,u}^{+,-}$, indicated in the following equation:

$$\begin{aligned} M_{\text{e' e}} &\sim \langle\, \psi_{\text{e'}} \mid \hat{\mu} \mid \psi_{\text{e}} \,\rangle \\ &\sim \Lambda_{g,u}^{+,-}(\psi_{\text{e'}}) \quad \otimes \quad \Lambda_{g,u}^{+,-}(\hat{\mu}) \quad \otimes \quad \Lambda_{g,u}^{+,-}(\psi_{\text{e}}) \quad \stackrel{!}{=} \quad \Sigma_g^+ \end{aligned} \tag{3.16}$$

At this point, it is convenient to determine the symmetry contributions of electronic states and of the dipole operator $\hat{\mu}$. As mentioned earlier, the z–projection of the orbital angular part of the wave function, (g, u) and $(+, -)$ define the symmetry of the electronic configuration. But, in order to deduce the symmetry of $\hat{\mu}$, it is important to consider two assigned directions in the system, namely the internuclear axis of the linear molecule and the light polarization. The orientation of these two directions leads to two special cases, specifically, when their axes are either parallel or perpendicular with respect to each other. Here, the two geometrical configurations are labeled as $P_{\parallel}$ and $P_{\perp}$ and their symmetry is given by

the corresponding irreducible representation as follows:

$$P_{\parallel} \equiv \hat{\mu}_{\parallel} \longleftrightarrow \Sigma_u^+ \tag{3.17}$$

$$P_{\perp} \equiv \hat{\mu}_{\perp} \longleftrightarrow \Pi_u \tag{3.18}$$

In dipole–allowed transitions, these two configurations enable the population of completely different symmetry states in the molecular system, which in particular holds for the doubly–excited states that are studied within this work. Some results of these operations are presented in the appendix Table 7.4, for molecular states with total angular momentum Σ and Π.

A general overview is represented in the appendix Table 7.3, where all possible excitations between Σ and Π states are associated to $P_{\parallel}$ and $P_{\perp}$ transitions. Moreover, the appendix Table 7.4 summarizes, how the projection of the angular momentum Λ as well as the symmetry properties g, u and $+, -$ will change under these transitions. Here, it is important to point out, that parallel and perpendicular transitions only access Q_n states with either Σ_u^+ or Π_u symmetry.

$$H_2\,(X\,^1\Sigma_g^+) \xrightarrow[\text{XUV}]{P_{\parallel}} H_2^{**}\,(Q_n)\,(^1\Sigma_u^+) \tag{3.19}$$

$$H_2\,(X\,^1\Sigma_g^+) \xrightarrow[\text{XUV}]{P_{\perp}} H_2^{**}\,(Q_n)\,(^1\Pi_u) \tag{3.20}$$

Most experiments work with unaligned, isotropic samples of molecules which has also been the case in this project. Nevertheless, it has been possible to extract information about the original molecular orientation from the recorded ions as their emission occurs along the internuclear axis within the so called axial–recoil approximation [Laf+03]. Hence, the analysis of photo–induced transitions in molecular hydrogen could be separated into parallel and perpendicular cases.

3.2.2 Photoelectron angular distributions

	$H_2^+(1s\sigma_g)$	$H_2^+(1s\sigma_u)$	$H_2^+(2p\pi_u)$	$H_2^+(2s\sigma_g)$
$P_{\parallel}$	σ_u	σ_g	π_g	σ_u
$P_{\perp}$	π_u	π_g	$\sigma_g + \delta_g$	π_u

Table 3.1: Photoelectron partial waves in parallel and perpendicular transitions for different final ionic states.

In dissociative photoionization, dipole selection rules restrict the total symmetry of the final products $H_2^+ + e^-$ to $(^1\Sigma_u^+)$ for parallel and $(^1\Pi_u)$ for perpendicular transitions, such that the symmetry of the complete process contains the totally symmetric irreducible

representation Σ_g^+. For each ionic state of defined symmetry, the wave function of the photoelectron is described as composed of a limited number of partial waves within the allowed symmetry [HE02]. A list of important photoelectron partial waves which are emitted in parallel and perpendicular transitions to H_2^+ are shown in Table 3.1, concerning four different final states. The notation of partial waves is adapted to the previously discussed scientific syntax of molecular orbitals, see 3.1.4, such that the symmetry properties of $\sigma \leftrightarrow \Sigma$, $\pi \leftrightarrow \Pi$ and $\delta \leftrightarrow \Delta$ are equivalent.

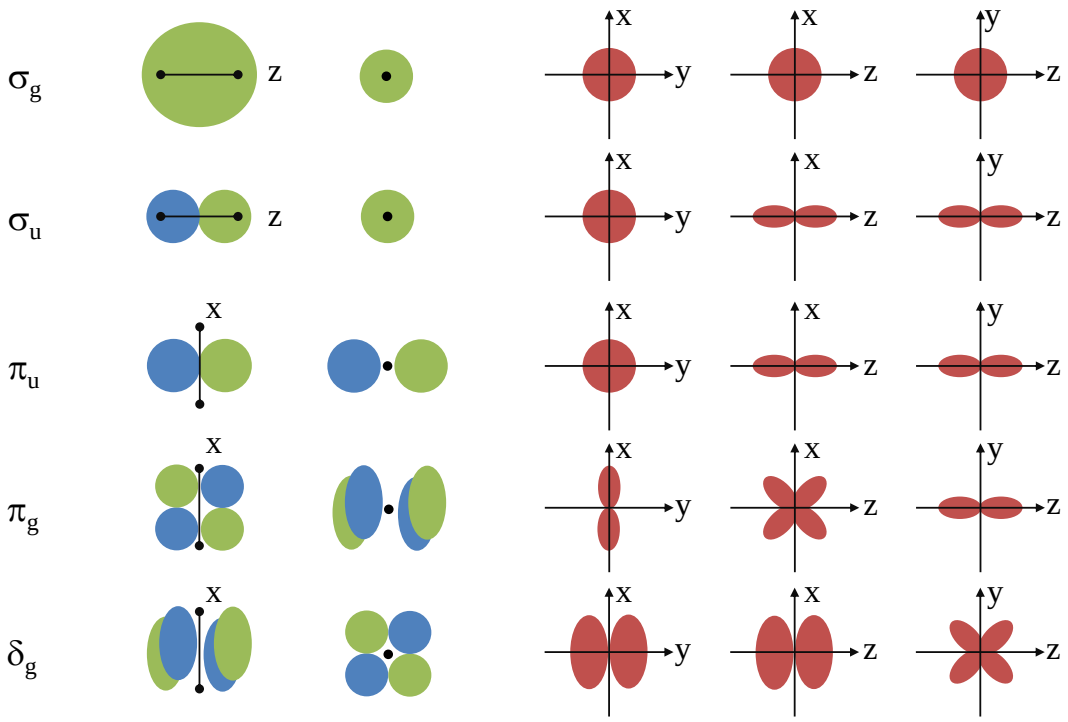

Figure 3.5: In dissociative ionization experiments with XUV light, in particular five different electron partial waves are encountered with σ_g, σ_u, π_u, π_g and δ_g symmetries. Green and blue areas depict parts of the wave function with opposite sign. The right panel represents the expected angular distributions in the two–dimensional subspaces (x,y), (x,z) and (y,z) of the experiment, including the polarization axis (z) and the associated molecular orientation, which is chosen to be (z) for parallel transitions or (x) for perpendicular transitions.

Partial waves exhibit characteristic shapes in the molecular frame of reference which are measurable as three–dimensional angular distributions. In Figure 3.5 both, the partial waves (blue and green) and the two–dimensional projections of the angular distribution (red structures) are shown. The partial waves are illustrated with blue and green elements, denoting parts of the wave function with opposite sign. In order to visualize the three–dimensional shape, the partial waves are presented in two orientations of the parent

molecule.

In the case of σ_g and σ_u the internuclear axis is shown parallel to the (z) direction (laser–polarization), whereas for π_u, π_g and δ_g the molecule is shown parallel to (x). The reason for this representation is that σ_g and σ_u are encountered mostly in parallel transitions where the molecular orientation in the laboratory reference frame is along (z). Similarly, π_u, π_g and δ_g are measured primarily in perpendicular transitions and without loss of generality[4] the molecular axis is set to (x).

This representation of σ_g, σ_u, π_u, π_g and δ_g allows to illustrate the corresponding angular distributions in the way as they are expected in the experiments with the two–dimensional projections (x, y), (x, z) and (y, z) (Figure 3.5). Note, due to a low contribution of the H_2^+ $(2p\sigma_u)$ state, the σ_g and π_g partial waves are also encountered in perpendicular and parallel transitions, respectively (see Table 3.1). In many cases, final energies and momenta of electrons resulting from different ionization channels are very similar and not distinguishable in the experiment such that the measured photoelectron wave functions correspond to a linear combination of the partial waves.

In this work, angular distributions were used exclusively to identify relevant states and autoionization channels within the dissociative ionization of H_2. For that reason, it has not been necessary to perform a quantitative analysis of the measured photoelectron angular emission spectra. Nevertheless, for completeness, the general method is briefly described which usually begins with the following expression:

$$I(\theta, \phi) \sim \sum_{l=0}^{l_{\max}} \sum_{m=-l}^{l} B_{lm} \, Y_{lm}(\theta, \phi) \tag{3.21}$$

Here, $Y_{lm}(\theta, \phi)$ are spherical harmonic functions where the angles θ and ϕ are defined with respect to the internuclear axis [Rei03]. The summation is performed over l up to l_{max} which is the highest orbital angular momentum quantum number of the generated partial waves, thus accounting for the complexity of the molecular structure. Equation (3.21) can be simplified for aligned, linear molecules with cylindrical symmetry into a sum of Legendre polynomials P_k [HE02]:

$$I(\theta) \sim \sum_{k}^{l_{\max}} A_k \, P_k(\cos\theta) \tag{3.22}$$

The coefficients A_k can be specified by the molecular orientation with respect to the polarization axis. For further details and explicit expressions of the A_k coefficients, the interested reader is referred to [Laf+03; Luc+02; HE02].

[4] The MFPAD transition, introduced in section 4.4.6, "rotates" the momentum vector of coincident ion and electrons such, that the internuclear axis of the parent molecule is pointing into the arbitrary chosen (x) direction, within the (x, y) plane.

3.2.3 Single XUV–photon transitions and Franck–Condon principle

So far, the molecular motion, represented by ψ_ν (if rotation is neglected) has not been considered in the discussions on the dipole–allowed electronic transitions in diatomic molecules. Within the frame of the Born–Openheimer approximation, the probabilities of such simultaneous electronic and vibrational transitions are proportional to the overlap of the vibrational wave functions. This can be understood by considering the matrix element of equation (3.14) e.g. for the transition from the vibrational ground state[5] of $H_2\,(^1\Sigma_g^+)$ to $H_2^+\,(1s\sigma_g)$.

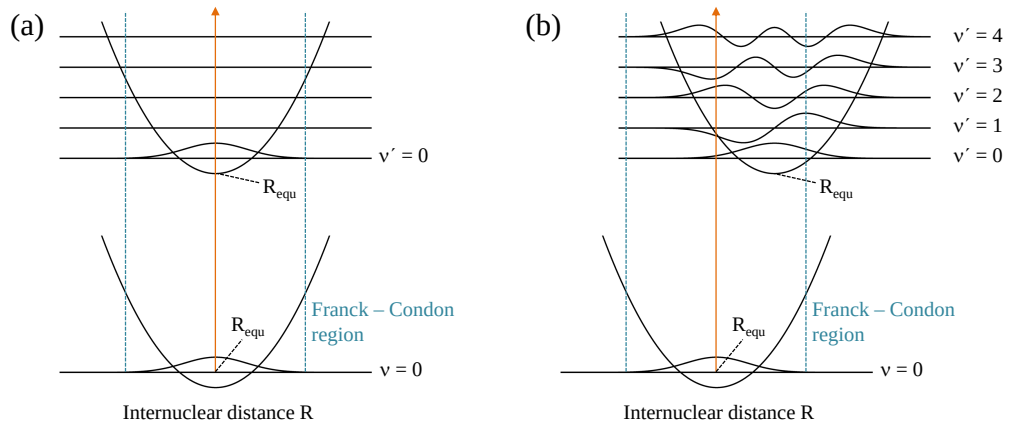

Figure 3.6: The Franck–Condon principle: (a) The PES of the initial and final states are identical. Thus, only the overlap integral between the two vibrational ground states is non zero. (b) Both PES exhibit different equilibrium internuclear distances. As a result, several vibrational states can be excited. The vertical blue lines mark the Franck–Condon region and the orange line represents the photon energy. Adapted from [ME11].

Since the dipole operator only acts on the electronic component, the dipole matrix element can be split into a "selection–rule" dominated term and a Franck–Condon factor which weights the influence of all contributing vibrational levels as well as continuum states.

$$M_{H_2\,H_2^+} \quad = \quad M_{\nu\mathrm{es}\,\nu'\mathrm{e's'}} \quad = \quad \langle\,\psi_{e's'}|\;\hat{\mu}\;|\psi_{es}\rangle \quad \underbrace{\langle\psi_{\nu'}\mid\psi_\nu\,\rangle}_{\text{Franck–Condon factor}} \tag{3.23}$$

In Figure 3.6, this concept, known as Franck–Condon principle, is illustrated for two transition scenarios. In the case of identical PES and equal equilibrium internuclear distances of the initial and final states, only the transition where $\nu = \nu'$ is fulfilled will contribute, since the basis of both vibrational levels are the same. This is different for deviating PES curvatures or equilibrium internuclear distances. Here, the Franck–Condon factors are not

[5] H_2 is considered in the vibrational ground state, since the occupation of higher states at the typical target–jet temperature is in good approximation zero.

vanishing for $\nu \neq \nu'$, as shown in Figure 3.6 (b), because the basis sets of the vibrational states are different in both electronic states.

As shown in experiments, the distribution of populated vibrational states in H_2^+ by the absorption of single XUV photons is qualitatively well described by the Franck–Condon principle and leads to the formation of so–called nuclear wave packets as described in the next section.

3.3 Properties of a vibrational wave packet

This section will present a theoretical background for exploring time–dependent effects in the dissociative ionization of molecular hydrogen investigated by superimposed short XUV and IR pulses. From the previous section we know that an XUV photon can ionize H_2 molecules and occupy, according to the Franck–Condon principle, several vibrational levels $|\psi_\nu\rangle$ e.g. in the bound $H_2^+(1s\sigma_g)$ electronic state. This ionization step can be considered instantaneously, meaning that the nuclear vibronic levels are coherently populated, i.e. have the same initial phase, thus giving rise to interference and the generation of a vibrational wave packet $\psi_{H_2^+}$:

$$\psi_{H_2^+} = \sum_\nu b_\nu \, |\psi_\nu\rangle \, e^{-i\frac{E_\nu t}{\hbar}} \tag{3.24}$$

The Franck–Condon factors b_ν denote the occupation of each state with the corresponding energy eigenvalue E_ν. If the XUV photon is confined within a short pulse (or pulse train) of less than 30 fs duration, a second, delayed, short, IR pulse can be used to probe the motion of the wave packet. Here, the IR laser leads to a transition from the binding $(1s\sigma_g)$ to the antibinding, dissociating $(1s\sigma_u)$ orbital. Since the probability for the IR–induced dissociation is dependent on the location of the nuclear wave packet (at the moment when the IR field encounters the H_2^+ molecule), the yield of measurable H^+ ions varies with delay. Hence, a delay experiment with XUV and IR pulses will resolve the motion of a nuclear wave packet. Note, in literature, such as [Kel+09], the IR–photon induced transition is explained by a strong–field effect, termed as bond softening [RS60; His61; Buc+90]. However, in this work, the consideration of a single–photon transition is sufficient.

For now, we want to continue with the considerations on the properties of the wave packet. In a harmonic potential, such a wave packet would evolve undisturbed in time, since the energy difference between two arbitrary states ν' and ν'' is an integer multiple of the lowest energy spacing $\hbar\omega$ (with ω being the eigenfrequency of the harmonic oscillator). The linearity in the appering energies thus leads to a linear phase relation $\phi \sim t$ and a wave packet that maintains its shape as a function of time. However, due to the fact that the non–dissociative PES in H_2 and H_2^+ correspond to anharmonic functions, the time evolution of the wave packet $\psi_{H_2^+}$ will lead to a de–and rephasing phenomenon.

This is analogous to the dispersion of an ultrashort laser pulse, with the difference that the vibrational wave packet is confined within the boundaries of the anharmonic potential. Hence, the fast and slow oscillating "parts" that contribute to $\psi_{H_2^+}$ will periodically overlap constructively in such way that the wave packet becomes narrow again. These features can be described by evolving the eigen energies E_ν in the superposition (3.24) in a taylor expansion around a specific $\nu_0 >> 0$, if the population density decreases significantly for neighboring $\nu_0 \pm n$ [Rob04]:

$$E(\nu) \;=\; E(\nu_0) \;+\; \frac{dE(\nu_0)}{d\nu}\,(\nu-\nu_0) \;+\; \frac{1}{2}\frac{d^2E(\nu_0)}{d\nu^2}\,(\nu-\nu_0)^2 \;+\; \cdots \tag{3.25}$$

From this we can deduce the time dependence of every single eigenstate.

$$\begin{aligned} e^{-iE_\nu t/\hbar} \;&=\; e^{-i\,(E(\nu_0)\,+\,\frac{dE(\nu_0)}{d\nu}\,(\nu-\nu_0)\,+\,\frac{1}{2}\frac{d^2E(\nu_0)}{d\nu^2}\,(\nu-\nu_0)^2\,+\,\cdots)t/\hbar} \\ &\equiv\; e^{-i\omega_0 t\,-\,2\pi i(\nu-\nu_0)\frac{t}{T_{\mathrm{cl}}}\,-\,2\pi i(\nu-\nu_0)^2\frac{t}{T_{\mathrm{rev}}}\,+\,\cdots} \end{aligned} \tag{3.26}$$

Here, T_{cl} and T_{rev} represent characteristic time scales, corresponding to a classical time and a revival oscillation time, respectively:

$$T_{\mathrm{cl}} \;=\; \frac{2\pi\hbar}{\left|\frac{dE(\nu_0)}{d\nu}\right|} \qquad \text{and} \qquad T_{\mathrm{rev}} \;=\; \frac{2\pi\hbar}{\left|\frac{d^2E(\nu_0)}{d\nu^2}\right|} \tag{3.27}$$

At this point we can specify the potential by an anharmonic morse profile with the anharmonicity constant α and provide detailed expressions of T_{cl} and T_{rev}:

$$E_\nu \;=\; \hbar\omega_0\Big[\,\Big(\nu+\frac{1}{2}\Big) - \alpha\Big(\nu+\frac{1}{2}\Big)^2\,\Big] \tag{3.28}$$

$$T_{\mathrm{cl}} \;=\; \frac{2\pi}{(1-\alpha-2\alpha\nu_0)\,\omega_0} \qquad \text{and} \qquad T_{\mathrm{rev}} \;=\; \frac{2\pi}{\alpha\,\omega_0} \tag{3.29}$$

One can understand T_{cl} as a barycenter period of the wave packet in the potential and T_{rev} representing the time, when all wave–packet components return into phase and reconstruct the original wave packet. The whole process can furthermore involve subrevivals when different fractions of $|\psi_\nu\rangle$ rephase.

For the vibrationally excited H_2^+ ion, it is possible to calculate T_{cl} and T_{rev} and the corresponding quantities are set to: $\hbar\omega_0 = 0.2714\,\mathrm{eV}$ and $\alpha = 0.0256$ [HS10]. The largest contribution to the wave packet is thereby given by $\nu_0 = 9$, as could be verified in section 5.1.2 as well as in previous measurements [SFH00], resulting in the following "model" values:

$$T_{\mathrm{cl}}^{\mathrm{mod}} \;=\; 29.7\,\mathrm{fs} \qquad \text{and} \qquad T_{\mathrm{rev}}^{\mathrm{mod}} \;=\; 596\,\mathrm{fs}$$

This simple model can be tested numerically with a simulation of the wave–packet for-

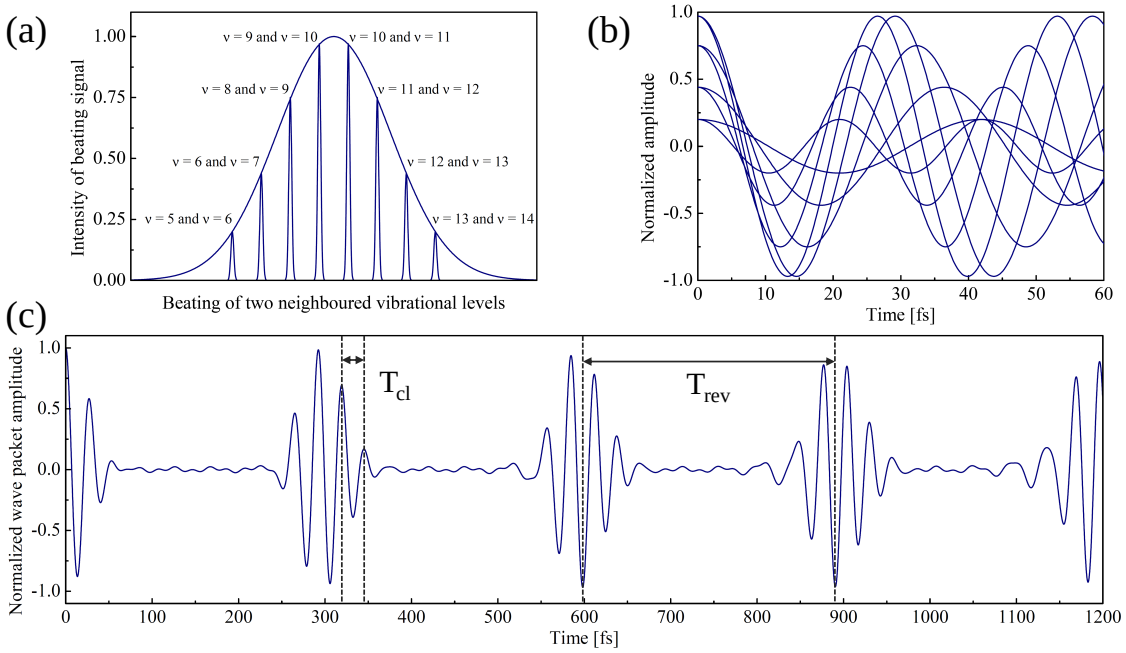

Figure 3.7: Simulation of the wave–packet formation and the revival cycle. (a) Here, only eight beating signals between neighbored vibrational levels with a specific amplitude contribute to the wave packet. (b) The superposition of these waves for the first 60 fs indicate the classical cycle period. (c) Constructive interference of the waves leads to the formation of the wave packet with $T_{\mathrm{cl}} = 27\,\mathrm{fs}$ and $T_{\mathrm{rev}} = 297\,\mathrm{fs}$.

mation and the corresponding temporal dynamics using calculated vibrational energies [BHP70], see Figure 3.7 (c). Fast and slow oscillations are generated by the coherent superposition of sinusoidal beating signals of eight neighbored vibrational levels ($\Delta\nu = 1$). Their distribution is shown in Figure 3.7 (a) as well as the corresponding amplitude which is given by a gaussian envelope function with a maximum at $\nu = 9$. Higher orders of beating, such as $\Delta\nu = 2, 3, \ldots$ are not included as their contribution is expected to be much lower. As a result of this simulation it is possible to specify the following characteristic times:

$$T_{\mathrm{cl}}^{\mathrm{sim}} = 27\,\mathrm{fs} \qquad \text{and} \qquad T_{\mathrm{rev}}^{\mathrm{sim}} = 297\,\mathrm{fs}$$

The values for T_{cl} that are extracted from the model and the simulation are quite similar, though T_{rev} deviates by a factor of 2. The reason for this can be found in the fact that for the H_2^+ molecule $\nu_0 >> 0$ is not fulfilled, which indeed is required in order to obtain correct values for T_{rev} [Rob04]. At this point it is interesting to note that the experimental data obtained in this project are much closer to the results that are calculated in the simulation. Nevertheless, the model provides a qualitative understanding of the underlying processes. More details on the wave–packet dynamics will be given in section 5.1.2.

3.4 Asymmetry and localization effects in the dissociative photoionization of H_2

In the dissociative ionization of diatomic molecules asymmetry effects are observed, if the final state is accessible via different pathways. Usually, the asymmetry parameter is defined by a relation between the electron and ion emission angles or the orientation of the parent molecule; however, in literature, the concept of asymmetry is not always uniform due to its varying appearance and origins. In [Red+12] for example, a study on photoelectron angular distributions in the dissociative ionization of H_2 with synchrotron light was presented, and the asymmetry therein corresponded to an oscillation of the beta parameter[6]. The necessary overlapping and interfering paths were identified to be the two lowest dipole–allowed doubly excited $1Q_1\,(^1\Sigma_u^+)$ and $1Q_2\,(^1\Pi_u)$ states.

In general, asymmetry parameters can be related to several measurable quantities (KER, $E_{\mathrm{kin}}(e^-)$, angles, etc.) and may depend, for the case of laser–induced absorption, on different laser parameters (carrier envelope phase (CEP), τ, etc.) [Kli+06; Kre+09; Fis+10].

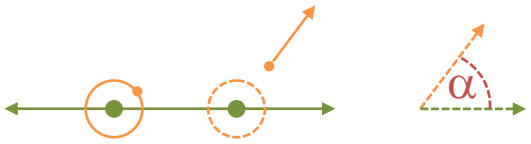

Figure 3.8: The asymmetry or localization is defined by an angle α between the emitted electron and the internuclear axis of the H_2 molecule. The vector of the molecular axis is imprinted in the dissociation direction of the molecule.

In the present work, the asymmetry corresponds to a localization of the fragments that result from the reaction

$$H_2 \quad \xrightarrow{XUV} \quad H^+ + H + e^- \tag{3.30}$$

in the reference frame of the parent H_2 molecule. In other words, the asymmetry is defined by the angle α between the electron and the molecular axis which in turn is measured by the emission direction of the coincident ion, as depicted in Figure 3.8. The quantitative expression is thus specified as

$$A \quad = \quad \frac{N_{\alpha<90} \; - \; N_{\alpha>90}}{N_{\alpha<90} \; + \; N_{\alpha>90}} \quad , \tag{3.31}$$

where $\alpha = |\alpha| < 90$ and $\alpha = |\alpha| > 90$ denote ion and electron pairs emitted into the same or into opposite hemispheres.

[6] The β_2 parameter describes the angular distribution of photoelectrons emitted in single–photon ionization.

Here, the localization of the measurable fragments – ions and electrons – follows, in principle, from the coherent superposition of gerade and ungerade states which in the case of an ionization to H_2^+ applies to the $(1s\sigma_g)$ and $(1s\sigma_u)$ states, both being involved in the dissociation though complex time–dependent population processes. The dissociation along these pathways acquire different relative phases, giving rise to interference and localization, if several conditions are fulfilled: First and most important, both interfering pathways have to lead to $H + H^+ + e^-$. Second, the distribution of the photon energy among ion, electron and atom must be identical in both cases since the resulting fragments would be distinguishable otherwise. Third, it is necessary that both electronic states and both emitted electron partial wave exhibit different symmetries, as illustrated in Figure 3.9.

Figure 3.9: Superposition of photoelectron partial waves in parallel and perpendicular transitions. The result is asymmetric in both cases.

The last condition can be understood by constructing a right–left basis for both, the emitted electron ϕ_R, ϕ_L and the remaining electron in the hydrogen atom φ_R, φ_L. This approach accounts for gerade (g) and ungerade (u) parity, the partial wave of the free electron (σ) and the total orbital angular momentum of the electron in the remaining molecular ion (Σ):

$$\begin{aligned} \phi_\mathrm{R} &= \sigma_g + \sigma_u \quad \text{and} \quad \varphi_\mathrm{R} = \Sigma_g + \Sigma_u \\ \phi_\mathrm{L} &= \sigma_g - \sigma_u \quad \text{and} \quad \varphi_\mathrm{L} = \Sigma_g - \Sigma_u \end{aligned} \tag{3.32}$$

Note, the treatment is adapted to parallel transitions, that is when the molecular axis and the polarization of the light field are collinear. For perpendicular transitions, the partial waves of the emitted electrons feature (π) symmetry and, accordingly, the basis is more complicated. In the presented basis there are two configurations for co– and counter propagating atom–electron pairs[7], respectively:

$$\left.\begin{aligned} |\,\psi_+^1\,\rangle &= \phi_\mathrm{R}\,\varphi_\mathrm{R} = (\sigma_g + \sigma_u)\,(\Sigma_g + \Sigma_u) \\ |\,\psi_+^2\,\rangle &= \phi_\mathrm{L}\,\varphi_\mathrm{L} = (\sigma_g - \sigma_u)\,(\Sigma_g - \Sigma_u) \end{aligned}\right\} \text{Co–propagating ion–electron pair}$$

$$\left.\begin{aligned} |\,\psi_-^1\,\rangle &= \phi_\mathrm{R}\,\varphi_\mathrm{L} = (\sigma_g + \sigma_u)\,(\Sigma_g - \Sigma_u) \\ |\,\psi_-^2\,\rangle &= \phi_\mathrm{L}\,\varphi_\mathrm{R} = (\sigma_g - \sigma_u)\,(\Sigma_g + \Sigma_u) \end{aligned}\right\} \text{Counter–propagating ion–electron pair}$$

[7] Co–propagating atom–electron pairs correspond to counter–propagating ion–electron pairs and vice versa.

The processes, that are specifically considered involve the lowest, direct dissociative state of the hydrogen molecular ion and an indirect path over doubly–excited states, with a delayed autoionization (AI). The corresponding pathways can be summarized and characterized with respect to symmetries as follows:

$$\begin{aligned} &H_2 \xrightarrow{\text{XUV}} H_2^+(1s\sigma_u) + e^- \xrightarrow{\text{dissociation}} H + H^+ + e^- \\ &\Lambda(e^-_{\text{free}}) = \sigma_g \quad \text{and} \quad \Lambda(e^-_{H_2^+}) = \Sigma_u^+ \end{aligned} \tag{3.33}$$

$$\begin{aligned} &H_2 \xrightarrow{\text{XUV}} H^{**}(Q_1(^1\Sigma_u)) \xrightarrow{\text{AI}} H_2^+(1s\sigma_g) + e^- \xrightarrow{\text{dissociation}} H + H^+ + e^- \\ &\Lambda(e^-_{\text{free}}) = \sigma_u \quad \text{and} \quad \Lambda(e^-_{H_2^+}) = \Sigma_g^+ \end{aligned} \tag{3.34}$$

Hence, it is possible to express the full final–state wave function such that the direct and the indirect pathways, involving autoionization (AI), are included with complex amplitudes c_1 and c_2, respectively, that are not further specified in the moment:

$$|\,\psi\,\rangle \quad = \quad c_1\,[\sigma_g\,\Sigma_u] \quad + \quad c_2\,[\sigma_u\,\Sigma_g] \tag{3.35}$$

In the next step, we can project the different asymmetry contributions on the final state and use the orthonogonality of the states:

$$\begin{aligned} |\langle\,\psi_+^1\,|\,\psi\,\rangle|^2 &= (c_1 + c_2)(c_1^* + c_2^*) &&= c_1c_1^* + c_1c_2^* + c_2c_1^* + c_2c_2^* \\ |\langle\,\psi_+^2\,|\,\psi\,\rangle|^2 &= (-c_1 - c_2)(-c_1^* - c_2^*) &&= c_1c_1^* + c_1c_2^* + c_2c_1^* + c_2c_2^* \\ |\langle\,\psi_-^1\,|\,\psi\,\rangle|^2 &= (-c_1 + c_2)(-c_1^* + c_2^*) &&= c_1c_1^* - c_1c_2^* - c_2c_1^* + c_2c_2^* \\ |\langle\,\psi_-^2\,|\,\psi\,\rangle|^2 &= (c_1 - c_2)(c_1^* - c_2^*) &&= c_1c_1^* - c_1c_2^* - c_2c_1^* + c_2c_2^* \end{aligned} \tag{3.36}$$

Finally, we can specify events with co– and counter–propagating particles and "add" them to N_+ and N_-, respectively:

$$\begin{aligned} N_+ &= |\langle\,\psi_+^1\,|\,\psi\,\rangle|^2 + |\langle\,\psi_+^2\,|\,\psi\,\rangle|^2 \\ N_- &= |\langle\,\psi_-^1\,|\,\psi\,\rangle|^2 + |\langle\,\psi_-^2\,|\,\psi\,\rangle|^2 \end{aligned} \tag{3.37}$$

The asymmetry A is then defined by the difference of these events and normalized with respect to the total number of events. As can be seen, only if both dissociation paths exist, or in other words, if c_1 and c_2 are nonzero, an asymmetry is expected to occur.

$$A = \frac{N_+ - N_-}{N_+ + N_-} = \frac{4\,c_1c_2^* + 4\,c_2c_1^*}{4\,c_1c_1^* + 4\,c_2c_2^*} = \frac{2\,\mathrm{Re}[c_1c_2^*]}{|c_1|^2 + |c_2|^2} \tag{3.38}$$

The exact value and the algebraic sign are defined by the phase difference between the emitted particles along both paths and are determined by the properties of the PES.

4 Experimental setup

Within this work, ionization and dissociation processes of hydrogen molecules induced by short laser pulses are investigated. The experiments were carried out using a reaction microscope (ReMi) which allows to detect the momentum vectors of electrons and ions resulting from these interactions in coincidence. The basic experimental setup is presented in Figure 4.1 and can be described in brief as follows: Ultrashort, infrared (IR) pulses are generated in a three–stage laser system, consisting of sub–systems for pulse generation, amplification and compression of the pulse duration. 70 % of the IR intensity is used to create attosecond pulse trains (APT) in the extreme ultraviolet (XUV) regime via the process of high–harmonic generation (HHG). Both light pulses, the remaining 30 % of the IR and the XUV are focused into the reaction volume of the ReMi to interact with single atoms or molecules provided by a cold, supersonic target beam. The ReMi is a combination of a recoil–ion spectrometer (COLTRIMS) and a large solid angle electron–spectrometer including weak homogeneous electric and magnetic fields to guide charged particles onto position and time–of–flight sensitive detectors [Ull+03]. This form of momentum spectroscopy enables the reconstruction of electron and ion trajectories from which the initial three–dimensional momentum vectors of the particles are calculated. Furthermore, the technique allows the separation of different reaction channels, providing complete information about the kinematics and delivering fully differential cross sections for the studied processes. The following sections will elaborate on the entire experimental setup, explained in four main parts:

Laser system: Generation of ultrashort IR laser pulses with a duration of $\sim 32\,\mathrm{fs}$ and a single pulse energy of 1 mJ at a repetition rate of 8 kHz.

Hollow–core fiber: Increase of the spectral width of the IR pulses via self–phase modulation in neon and subsequent compression of the pulse duration to $\sim 12\,\mathrm{fs}$.

HHG in Argon: Generation of ultrashort attosecond pulse trains with photon–energies between 15 and 40 eV.

ReMi: Kinematically complete detection of electrons and ions in photon–induced ionization and fragmentation processes.

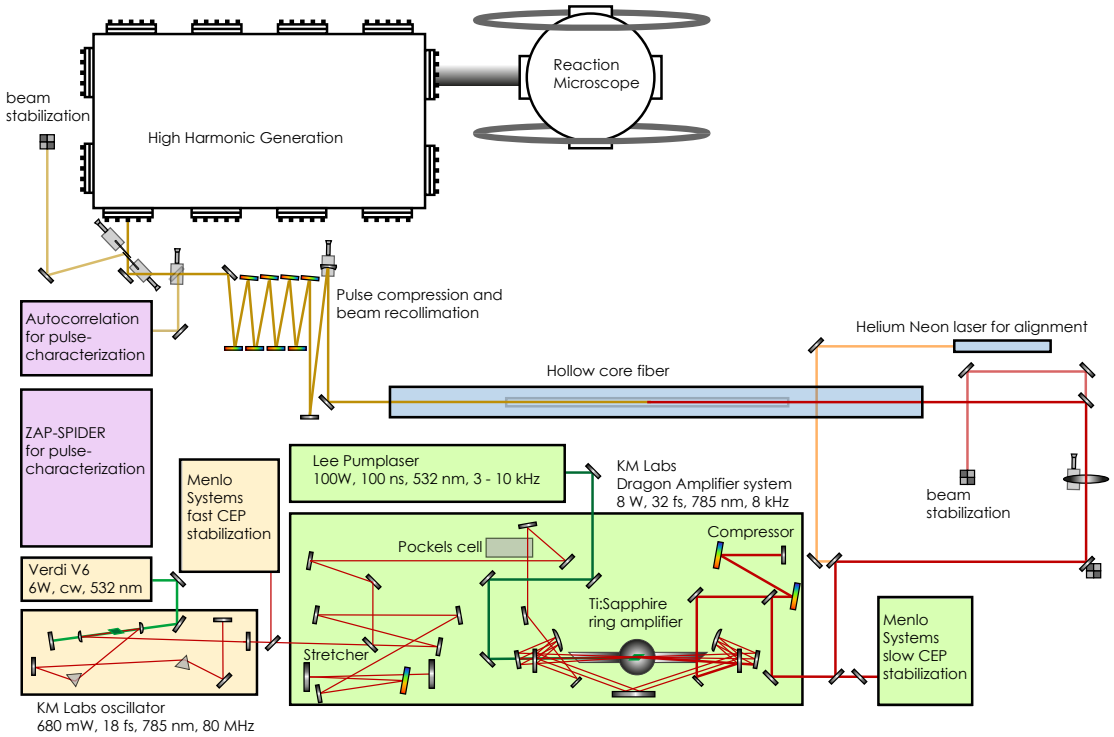

Figure 4.1: Detailed scheme of the experimental setup, divided into oscillator (orange), pulse amplification (green), hollow–core fiber setup (blue), HHG and ReMi (both white). The diagram includes pulse characterization devices (purple).

4.1 Ultrashort pulse laser system

The laser system is based on the chirped pulse amplification technique (CPA [SM85]) and involves an oscillator for the ultrashort pulse generation and an amplifier system to provide sufficient single–pulse energies. The corresponding setups are illustrated in Figure 4.1 including the detailed beam paths and specified values of important output parameters.

4.1.1 Oscillator

A Kerr–lens mode–locked Ti:Sapphire oscillator provides ultrashort femtosecond– and low energetic laser pulses at a repetition rate of 80 MHz. The major components are the Ti:Sapphire–gain crystal, a pump laser, dispersion compensation optics and feedback mirrors that form an optical resonant cavity and determine the frequency comb as well as the repetition rate. With these components and the Kerr–lens effect, it is possible to induce a defined phase–relation between the allowed, longitudinal modes in the resonator, a process referred to as mode–locking. Interference of the oscillating waves finally gives rise to short intensity spikes or laser pulses which is also illustrated in Figure 2.1 in section 2.1.

To enable the Kerr–lens effect, a frequency doubled, continuous wave (cw) Nd:YVO high stability pump laser (5.5 W) is coupled into the resonator and focused onto the Ti:Sapphire crystal, thus initializing a lasing–process in the infrared domain. In this context, there are two important features of the crystal that must be mentioned: First, it is a large bandwidth material, and therefore supports the amplification of a broad spectral part of the frequency comb. The corresponding spectral profile determines the pulse duration and temporal shape. Second, the crystal is a nonlinear material which means that the refractive index is intensity dependent. This fact gives rise to the Kerr–lens effect and can be understood making the following considerations: Imagine an already existing pulse with a Gaussian intensity profile, oscillating in the cavity. For every round–trip of this pulse, the crystal acts as a lens; however, only the high–intensity part will be strongly focused and thus will overlap with the pumped part of the crystal. As a consequence, the wings of the pulses will acquire a lower gain and only the central part of the intensity profile will be periodically amplified during every cycle in the cavity. This corresponds to an automatic phase locking of the amplified frequency components. Since the described process requires existing pulses, their initialization has to be effected by another way. Small intensity fluctuations of the initial radiation in the cavity, induced e.g. by a slight kick on one of the optical components are already sufficient for that purpose.

In view of the amount of dispersive media within the cavity, all oscillator construction types contain dispersive compensation elements, in this case a pair of prisms is installed, which moreover allows to adjust to some extent the bandwidth of the pulses.

In summary, it is possible to produce pulses of 18 fs duration, 63 nm spectral bandwidth and 8.5 nJ single–pulse energy which corresponds to a mean output power of 680 mW. Part of the output can be used for carrier envelope phase (CEP) stabilization.

4.1.2 Amplifier (CPA)

The pulses emerging from the oscillator system are not of sufficient strength as the HHG and the experiments described in section 5 require intensities between 10^{11} to 10^{15} $\mathrm{W/cm^2}$. For this reason, the pulse energies are increased with a commercial ring–amplifier system[1] by a factor of 10^5 to 10^6. It is based on the principle of chirped pulse amplification (CPA) and pumped by a Q–switched Nd:YAG (frequency doubled) 100 W pump laser[2], providing the required energy. The complete setup consists of four modular subdivisions, namely pulse–stretcher, Pockels cell, amplifier ring and pulse–compressor. Their respective operation mode can be explained by following the beam path of an oscillator IR pulse through the system:

In the first stage, the oscillator pulse is stretched to several picoseconds by a folded, highly dispersive double–grating arrangement, as the peak intensity must be kept below

[1] KM Labs, Dragon CPA system.
[2] Lee Lasers Inc.

the damage threshold of the amplifier Ti:Sapphire crystal. Next, it is necessary to reduce the repetition rate of the system by a factor of 10^4, to 8 kHz, in consideration of the maximum output power and pulse energy that the Nd:YAG pump laser provides (100 W, 10 mJ and 100 ns). In this setup the reduction of the repetition rate is realized by a Pockels cell. The pump laser single–pulse energy, together with the conversion efficiency, lead to achievable single IR pulse energies of approximately 1 mJ. Therefore, higher energies can only be obtained by increasing the pump laser output power or by further reducing the repetition rate.

The actual amplification of the IR pulse is performed in a multipass ring configuration. Both, the femtosecond laser pulse from the oscillator and the pump beam are focused, and spatially and temporally overlapped in a cryogenically cooled Ti:Sapphire crystal[3]. The setup is aligned such that the IR pulse propagates thirteen times through the crystal, thus achieving maximum amplification. An adjustable twelve–hole aperture in the Fourier plane within the ring configuration is used to reduce amplified spontaneous emission (ASE).

Finally, the amplified infrared pulse must be recompressed which is realized by another grating compression system. As a result, Fourier limited IR pulses of 32 fs pulse duration are generated. The original pulse duration of 18 fs from the oscillator cannot be achieved due to a gain narrowing effect in the amplification process within the ring configuration. Therefore, it becomes necessary to implement another device for further pulse compression.

4.2 Hollow–core fiber system

In order to achieve shorter pulse durations, a hollow–core fiber setup with a chirped mirror compressor has been implemented after the amplifier system. In this technique, the amplified IR pulses are focused into a gas–filled (neon) hollow–core fiber where the high peak intensities cause several linear and especially nonlinear processes in the gaseous medium. The interplay of these processes leads to a broadened spectral profile of the pulses which according to the time–bandwidth product is consistent with a lower Fourier limit, i.e. shorter achievable pulse durations. With this method, it is thus possible to push pulse durations from the 30 fs into the sub–10 fs, few–optical cycle domain [For+87; Bal+97].

The motivation for creating shorter pulses is given by the time duration of the physical processes that shall be investigated and are analyzed in chapter 5. In particular time–dependent studies of electronic and vibrational transitions in atomic and simple molecular systems, usually in the range between 100 as and 20 fs demand even shorter pulses. Yet another reason is an optimized high–harmonic generation [Nis+02]. Since the HHG is a periodic process, induced every half cycle of the fundamental IR pulse, it is obvious that a shortened pulse, going hand in hand with a reduced number of optical cycles, will lead to

[3] With the cryogenic cooling the crystal is operated below $-200\,^{\circ}C$. At these temperatures, the influence of phonons is reduced and in addition, the heating transportation becomes more efficient.

fewer but more intense pulses within the APT. For a $30 - 35$ fs laser pulse, this translates into an APT containing $20 - 25$ individual pulses with similar intensities. In contrast, the number of pulses within the train is reduced to $7 - 8$ for a 10 fs fundamental IR pulse. This is suitable to apply efficient gating technologies which are widely used in single–attosecond pulse generation [Cha11; Gil+10].

4.2.1 Experimental setup of the hollow–core fiber

Figure 4.2 presents an overview over the hollow–core fiber setup, illustrating main features, such as focusing, the rare gas cell and the pulse compression stage.

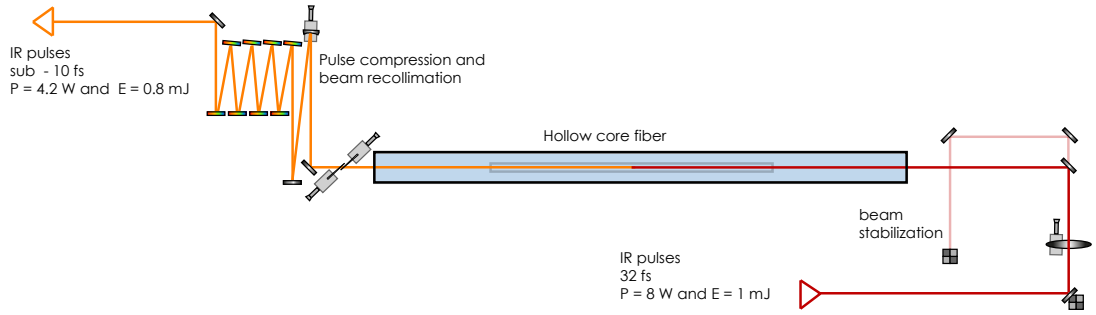

Figure 4.2: The hollow–core fiber setup and the subsequent pulse compression consisting of chirped mirror pairs. The fiber is mounted loosely on a guide rail and filled with neon gas at a pressure of 3.5 bar.

First, the laser beam is guided on an $f = 1500$ mm antireflection coated plano–convex lens which focuses the laser beam into a hollow–core fiber filled with neon gas. The fiber length corresponds to approximately 1 m with an inner core and cladding diameter of 250 µm and 2 mm, respectively.

The interplay between beam waist, focal length and core diameter is crucial, as they determine the losses (output power), the suppression of undesirable hybrid modes (EH_{nm}) and the laser intensity in the fiber. Therefore, the focal length was chosen in view of the beam diameter of 12 mm such that an entrance–to–focus size ratio of approximately 2:1 was reached, which gives the best results [Zro05] and leads to an expected throughput of $55 - 65$ %. In addition, the lens has to be inclined slightly towards the laser propagation direction by an angle of $\sim 10°$ to compensate for laser–inherent astigmatism.

In order to reduce intensity fluctuations and spectral changes in the output, a commercial beam pointing stabilization system of MRC[4] is implemented. This is necessary, as even smallest mechanical changes of optical components, caused for example by temperature gradients within the amplifier system, lead to measurable drifts of the laser propagation direction.

[4] MRC Compact; active beam stabilization for four axis.

Inside the fiber, several nonlinear effects, such as self–phase modulation (SPM) and self–steepening are caused by the gaseous medium due to the high peak intensities of the laser pulses. These processes can also be induced in a gas without using the surrounding fiber; however, the required intensity is only provided within the Rayleigh range[5] along the beam propagation. As the refractive index in gaseous media and the corresponding phase shifts are small in comparison to solids, neglecting plasma and filamentation processes, the resulting spectral broadening is low in that case. This is different, if the laser is confined in the small volume of the fiber, as the interaction distance, where the laser intensity is high enough to induce nonlinear effects exceeds the typical Rayleigh range by almost two orders of magnitude.

4.2.2 Spectral and temporal broadening with the hollow–core fiber

The main objective of the hollow–core fiber system is an efficient spectral broadening; nevertheless, it is also important to achieve minimal losses, a stable spectral profile, small beam pointing variation and a perfect EH_{11} hybrid mode [Nis+97b]. To this end, the choice of the gaseous medium and its associated pressure can be critical. In Figure [4.3] several spectral profiles are presented for varying neon pressures, showing that the spectral broadening becomes larger with increasing pressure. At a certain, upper "pressure limit", several objectionable processes occur, such as plasma formation, dispersion and beam fluctuations, suggesting an optimum neon pressure of 3.5 bar. hollow–core fiber setups

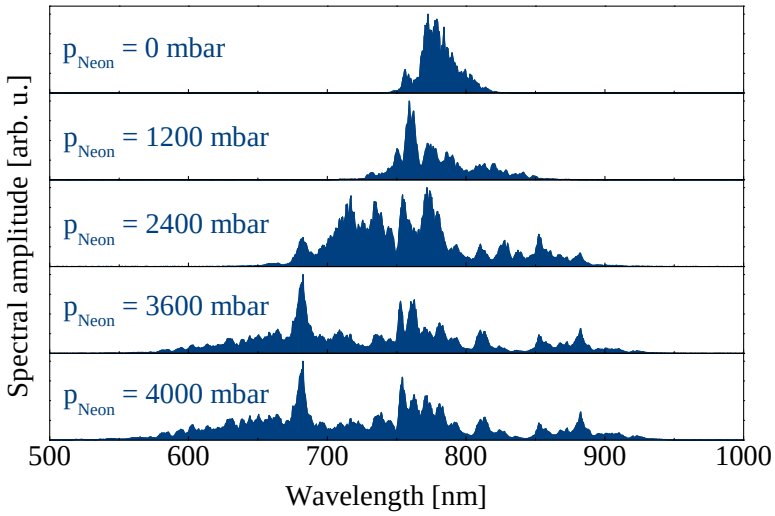

Figure 4.3: Spectral broadening at different pressures in the hollow fiber.

are usually operated with rare gases, especially neon and argon, due to their relatively

[5] The Rayleigh range for the fundamental IR laser beam with $\lambda_c = 785\,\text{nm}$ and the mentioned focusing parameters corresponds to 1.7 mm.

high ionization potentials in comparison to other gases. Nevertheless, even in these gases, plasma formation originating from multi–photon ionization is possible and must be avoided, as it leads to destruction of the fiber material, in particular at its entrance. Furthermore, it can distort the laser mode and reduce the output power.

The following sections will provide an overview of the dominant effects in the medium. The interplay of several linear, and especially nonlinear processes, which occur in the hollow–core fiber can be well explained by theoretical models and numerical simulations considering electromagnetic wave propagation in nonlinear media and strong–field interaction with rare–gas atoms. Nevertheless, the shape of the spectral and temporal profile of the pulses can in principle be understood within a very basic approach by considering only three major effects, including self–phase modulation (SPM), self–steepening and dispersion. Together they lead to spectrally and temporally broadened pulses.

Self–phase modulation

The first and most important effect that leads to spectral broadening is the self–phase modulation. Here, the pulses gain additional spectral components but maintain their temporal profile as presented in Figure 4.4 and, thus, they are no longer Fourier limited. This behavior is understood taking into account the intensity dependence of the refractive

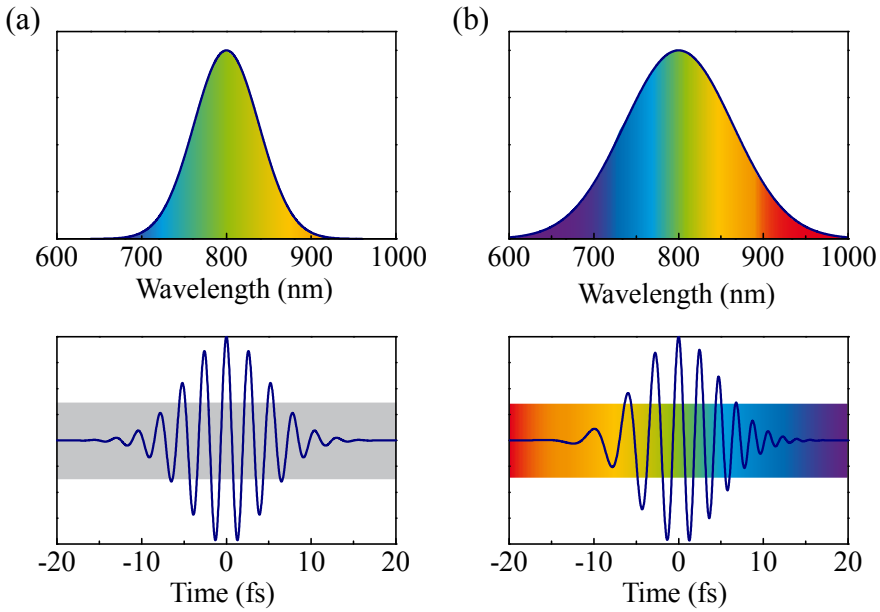

Figure 4.4: Self–phase modulation: Representation of Gaussian shaped pulses in the spectral and temporal domain, (a) before and (b) after SPM, respectively.

index and analyzing the consequences for the temporal pulse–function. In this context, we

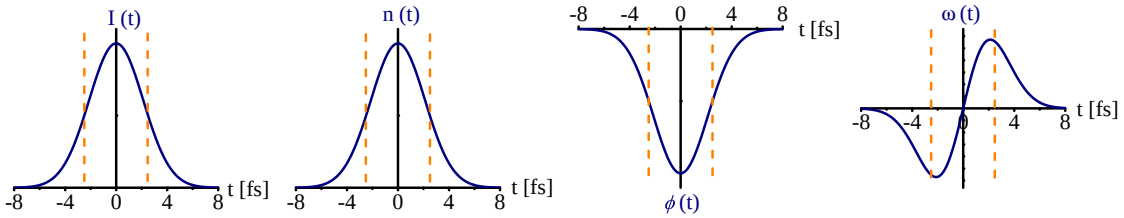

Figure 4.5: Self–phase modulation: Effect of the intensity profile $I(t)$ on the refractive index $n(t)$, the spectral phase $\phi(t)$ and the carrier frequency function $\omega(t)$. The dotted lines mark the FWHM of the pulse profile. Adapted from [Cha11].

begin our considerations with a Gaussian intensity profile in the time domain:

$$I(t) \;=\; I_0\, e^{-4\,\ln 2\,\frac{t^2}{\tau^2}} \tag{4.1}$$

The refractive index of the gaseous medium is split into a constant, wavelength–related part which corresponds to the linear refractive index and a second fraction, associated to the optical susceptibility which is intensity dependent:

$$n(\lambda, I) \;=\; n_0(\lambda) \,+\, n_2(I) \tag{4.2}$$

When laser pulses propagate through a linear or nonlinear medium, their respective temporal phases are connected to the corresponding refractive index of the gas. In this case, as dispersion is neglected, n_2 will simply cause a linear phase shift

$$\begin{aligned} \phi(t) \;&=\; \omega_0 t \,-\, k_n\big(\lambda, I(t)\big)\cdot L \;=\; \omega_0 t \,-\, \frac{\omega_0}{c} n\big(\lambda, I(t)\big) L \\ &=\; \omega_0 t \,-\, \frac{\omega_0}{c}\Big[n_0(\lambda) + n_2\big(I(t)\big)\Big]\, L \quad , \end{aligned} \tag{4.3}$$

proportional to the propagation length L in the material, with the wave vector k_n and c being the speed of light. The carrier frequency function $\omega(t)$ is obtained by the derivation of the temporal phase, and exhibits compressed, as well as stretched waves at the observed pulse wings. In the spectral domain, this is equivalent to the generation of new frequency components arranged symmetrically around the central frequency ω_0.

$$\begin{aligned} \omega(t) \;=\; \frac{d}{dt}\phi(t) \;&=\; \omega_0 \,-\, \frac{\omega_0}{c}\, n_2\, \frac{d}{dt} I(t)\; L \\ &=\; \omega_0 \left(1 \,+\, \frac{2\, L\, n_2\, I_0}{c}\, \frac{t}{\tau^2}\, e^{-\frac{t^2}{\tau^2}}\right) \end{aligned} \tag{4.4}$$

The $1/\tau^2$ dependence in equation 4.5 demonstrates that the spectral broadening is more efficient for shorter initial pulses. For that reason, the IR pulses from the amplifier must be generated with the lowest possible pulse duration. The described intensity dependences

of the refractive index $n(t)$, the spectral phase $\phi(t)$ and the carrier frequency function $\omega(t)$ are illustrated in Figure 4.5.

It should be noted, that the SPM is only a time dependent view of the general Kerr–lens effect which includes additionally the spatial intensity distribution and describes dynamic processes, such as self focusing.

Self–steepening

The self–steepening effect is equally related to the temporal profile of the laser pulse and to the intensity dependence of the refractive index as the SPM. In an intuitive picture, a short pulse is viewed as being composed of several sub–pulses at the pulse wings and in the center as illustrated in Figure 4.6. Relating the intensity–profiles of the sub–pulses to the

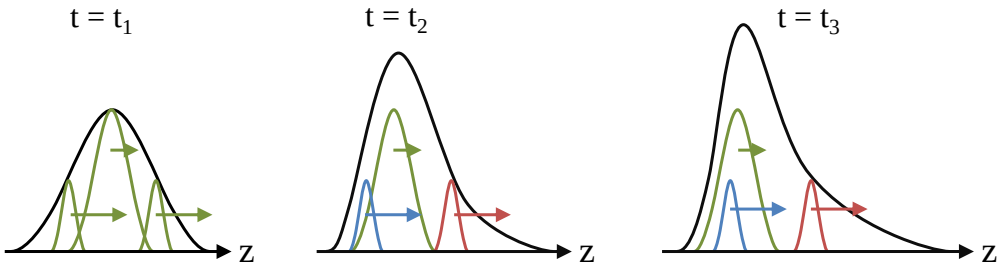

Figure 4.6: Self–steepening influencing the temporal pulse shape at three different times $t_1 < t_2 < t_3$. Central and wing–sub–pulses propagate (in z–direction) with different group velocities, thus reshaping the temporal profile. The color of the sub–pulses reflects the associated frequency spectrum.

refractive index $n_0 + n_2(I(t))$, leads to different group velocities in addition to SPM. Low intensity sub–pulses thus experience a higher group velocity whereas the high intensity central part exhibits a low group velocity. Hence, the temporal pulse shape is affected strongly, as the tail of the total pulse catches up with its intensity maximum, while the front part is running away.

Combining both SPM and self–steepening in a more general perspective explains, why the frequency generation is shifted to higher frequencies, or in other words, why the central wavelength is shifted towards the blue range of the spectrum. To understand this, one has to consider the influence of the SPM on the two sub–pulses. In the SPM, red and blue frequency components are generated on opposite sides of the main pulse which is illustrated in Figure 4.4 (b). As a consequence, the front and the back sub–pulses obtain exclusively red or blue frequencies, respectively (see Figure 4.6). According to the self–steepening, the back pulse propagates into the central part, such that its intensity increases. Hence, the complete pulse is composed of a high–intensity part which contains mainly blue frequencies and a low–intensity part with the red frequency components. The SPM of

course is more efficient for the highly intense part and, as a result, the generation of blue frequencies dominates. For extreme spectral broadening, the measured asymmetric profile can even exceed the full visible range, an ultrashort–pulse phenomenon termed as white–light generation [BH00].

Dispersion

General theoretical aspects of dispersion of short laser pulses are discussed in section 2.2.2. With respect to the fundamental pulses and their corresponding pulse length of 32 fs, it is sufficient to consider the influence of the second–order dispersion, $\varphi^{(2)}$, which is known as the linear chirp. Third- and higher–order dispersion becomes relevant for pulses approaching the sub–8 fs range and, therefore, are negligible within this project.

In general, there are two aspects where the linear chirp is important. First, it must be considered when relatively high gas pressures are applied. Second, the influence of dispersion increases during pulse propagation through the fiber, which can be understood in the context of the previously discussed SPM. This effect does not intrinsically modify the pulse duration; however, the spectral width is increased and, accordingly, the impact of dispersion. Hence, the linear chirp broadens the pulses even more with proceeding pulse propagation and simultaneously reduces the peak intensity and, thus, the efficiency of SPM. For these reasons it is necessary to interrupt the process as soon as the peak intensity becomes too low and re–compress the laser pulses after the spectral broadening.

Active modes

Most fused–silica fiber geometries support up to three different types of transversal modes, transversal–electric TE_{0m}, transversal–magnetic TM_{0m} and hybrid modes EH_{nm}[6]. The specific configuration of the hollow–core fiber, that is the focusing parameters, the fiber entrance area and the fiber length, determine the intensity of each of these modes. In terms of an efficient high–harmonic generation, which strongly depends on the degree of linear polarization, it is necessary to attenuate all nonlinear polarized modes. In this context, the fundamental hybrid mode EH_{11} provides the best properties and, therefore, is usually implemented.

An advantageous fact is related to laser propagation along hollow–core fibers, which can be considered as grazing incidence reflections at the inner wall. By these multiple reflections, losses mostly decrease the intensity of higher modes [Agr01]. In Figure 4.7 vertical projections of TEM_{nm} are presented as they show similarities to the mentioned EH_{nm}. It should be noted, that the favored EH_{11} corresponds to the TEM_{00}. The intensity profile $I(r)$ of the EH_{11} can be described by the following expression, where I_0 is the peak

[6] In this project, the amplifier IR pulses are linearly polarized. As a consequence, only hybrid modes are encountered in the hollow–core fiber [Zro05].

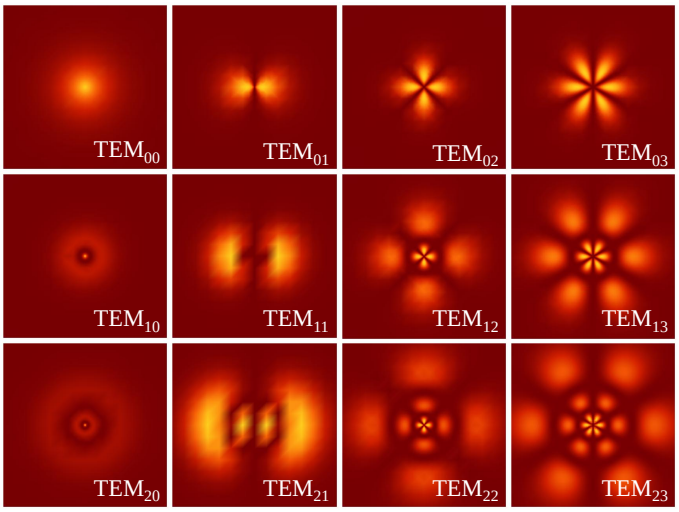

Figure 4.7: Simulated TEM$_{nm}$ modes, which represent a similar structure as the hollow–core fiber hybrid EH$_{nm}$ [MS64].

intensity, r is the radial coordinate, a is the core radius and J_0 is the zero–order Bessel function with its m–null position $u_{1m} = 2.405$ [MS64].

$$I(r) = I_0 \, J_0^2 \, (u_{1m} \frac{r}{a}) \tag{4.5}$$

For every mode there is a real propagation constant β and an imaginary field attenuation coefficient $\alpha/2$, where ν is the ratio of the refractive indices between the fused silica cladding and the gaseous core (1.47). Note, that there is no total reflectivity at the boundary surface like in solid core fibers, explaining the higher mode suppression.

$$\beta = \frac{2\pi}{\lambda} \left(1 - \frac{1}{2} \left(\frac{u_{1m} \lambda}{2\pi a} \right) \right) \tag{4.6}$$

$$\frac{\alpha}{2} = \left(\frac{u_{1m}}{2\pi} \right)^2 \frac{\lambda^2}{2a^3} \frac{\nu^2 + 1}{\sqrt{\nu^2 - 1}} \tag{4.7}$$

For Gaussian pulses, as represented in the equations (2.5), (2.6), it is possible to specify the maximum of the spectral broadening $\delta\omega_{\max}$ as follows:

$$\delta\omega = 0.86 \, P_0 \, \frac{n_2 \, \omega_0}{c \, A_{\text{eff}}} \, \frac{1 - \exp^{-\alpha L}}{\alpha} \, \frac{1}{\tau} \tag{4.8}$$

Here, $A_{\text{eff}} = a^2\pi$ is the effective mode area and ω_0 the center frequency of the laser. Inserting typical experimental values in equation (4.8) leads to a spectral broadening, three times higher than the measured. This is mainly caused by the neglect of dispersion in the fiber [Cha11].

4.2.3 Pulse compression

After generating blue shifted, broadened spectral profiles it is necessary to reduce the pulse durations towards the Fourier limit with a pulse compressor. In this setup, this is achieved by six pairs of chirped mirrors where each mirror introduces a negative second order dispersion value of approximately $-50\,{}^{1}/_{\mathrm{fs}^2}$. In addition to the inherent nonlinear phase induced by the SPM effect, many dispersive elements such as the exit window of the fiber cell (1 mm) as well as the entrance window of the HHG chamber (1 mm) and a beam splitter (0.5 mm) induce temporal pulse broadening and must be pre–compensated. Further optical components such as waveplates, beamsplitters and especially a beam–propagation distance of 7 m in air must be included in these considerations. For this reason, a special dispersion–software, developed by A. Fischer [Fis10], is employed to design an optimal combination of chirped mirrors. Usually, the layer profile of these mirrors involve oscillating $\varphi^{(2)}$, or GDD curves; however, this can be compensated, as indicated, by assembling the mirrors in pairs with inverse phase. The corresponding setup is illustrated in Figure 4.2 exemplary with four mirror pairs which are positioned on opposite sides with respect to each other.

Despite the advantages of the dispersion–software, it is difficult to account for all dispersive elements correctly, as the accuracy in the characterization of the different components varies. Especially the dispersion introduced within the hollow–core fiber setup can only be set to an approximate value of $180\,\mathrm{fs}^2$ [Fem]. In addition, a pair of wedged glasses for fine adjustment is employed in the setup, allowing for introducing slight changes of positive dispersion.

With these strategies, it is finally possible to generate satisfyingly short pulses of 12 fs within this configuration.

4.3 High–harmonic generation

In this section, the technical realization of HHG is explained. To summarize the most important properties of high–harmonic light in form of attosecond pulse trains, APTs, Figure 4.8 presents the main features in the time and frequency domain, such as the $T/2$ and $2\,\omega_0$ spacing, respectively.

In the high–harmonic chamber, ultrashort APTs with photon energies reaching into the XUV range are created. The setup furthermore provides subsequent beam alignment into the ReMi and allows to overlap the APT with a separate part of their generating, fundamental IR pulses. By this, it is possible to perform single pulse as well as one– and two–color pump–probe measurements. Several experimental parameters are adjustable, such as pump–probe delay settings between a few femtoseconds up to 3 picoseconds, a large IR intensity range and the possibility to optimize the beam polarization. Moreover, the setup allows for a modular alignment and optimization of several parts of the system

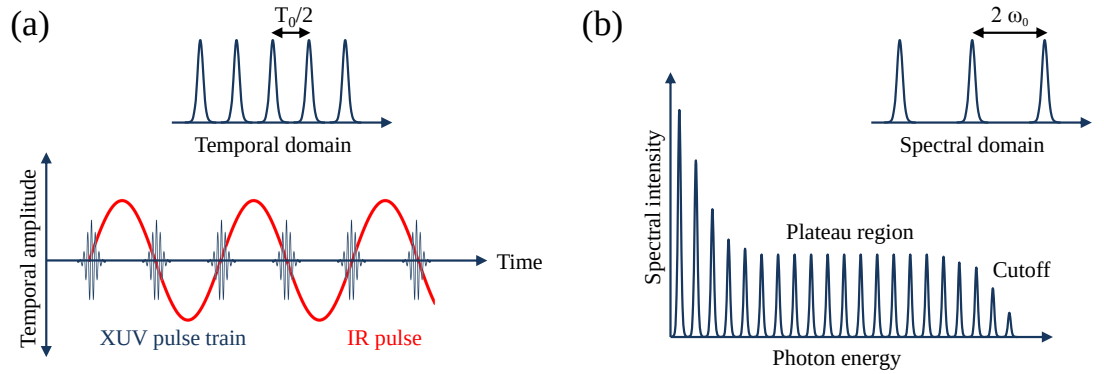

Figure 4.8: Properties of the high–harmonic XUV radiation in (a) the temporal and (b) the spectral domain.

via motorized mirror mounts and translation stages. A high interferometric stability is achieved by vibrationally isolating the complete optical setup from the chamber walls[7] and connecting it to the main optical breadboard of the laser system. The complete chamber is designed to be vented and pumped on a regular basis in order to frequently establish improvements and necessary replacements of filters and target tubes. In the following section important features of the chamber setup will be presented, including details on optical components, alignment requirements and vacuum–pumping techniques.

4.3.1 Experimental setup of the high–harmonic generation

Photons with far UV energies are efficiently absorbed in gaseous media and in glass, making the generation and propagation of the XUV beam in vacuum necessary. Another difficulty arises from losses of the weak HHG beam due to beam guiding and focusing. Those are reduced by using reflections at gracing incidence angles and high–reflective optics with an extremely low surface roughness. As a consequence, the whole XUV path, beginning at the generation and ending in the reaction volume of the ReMi, points in approximately one direction.

Figure 4.9 presents the complete HHG setup and illustrates most of the technical details that are discussed in the following. It is intuitive to explain these details and the functions of the installed elements by following the beam path. But before starting, it must be noted that the main HHG chamber contains two additional inner chambers – termed as target and focusing chamber – which both are pumped independently. This is necessary to achieve a vacuum of high quality in the main chamber as well as in the connection tubes to the ReMi.

Initially, the IR beam enters the chamber through a thin fused silica glass window of

[7] The isolation in particular reduces the influence of the molecular turbo pumps.

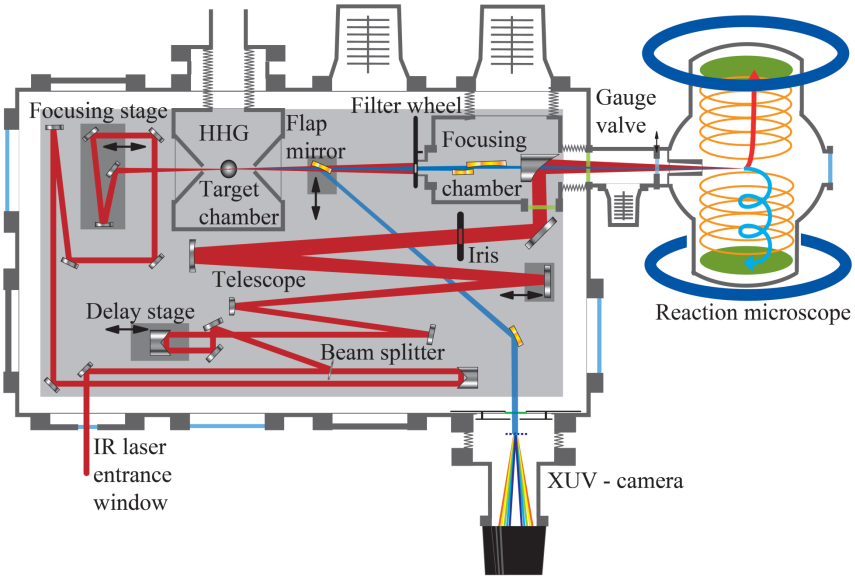

Figure 4.9: Scheme of the HHG chamber, including the XUV generation in the target chamber, focusing of both beams in the focusing chamber and the IR delay stage. The CCD spectrometer / XUV–camera for controlling of the spectral profile is indicated at the lower side.

1 mm thickness and is split into two half–beams in a Mach–Zehnder type arrangement with matching optical lengths (here, the two optical paths will be depicted as XUV and IR path). 70 % of the initial beam intensity is diverted to the XUV path for the HHG, whereas the remainder is guided along the IR path, thus forming the delay and probing section of the experiment.

The XUV generating branch is guided and focused with a 1000 mm focal distance into the target chamber. In this setup, a concave mirror is used instead of a lens to prevent dispersion. It is installed at the lowest possible reflection angle to further avoid astigmatism. The focusing mirror is then followed by a motorized translation stage with three pre–aligned mirrors which determine the overall beamline and allow for optimization of the phase matching condition and the high–harmonic light yield during experiments. The conversion from IR into XUV light takes place in a cylindrically shaped gas cell, positioned on a multidimensional translation stage in the center of the target chamber which is illustrated in Figure 4.10 (a). In Figure 4.10 (b) a detailed view of the gas cell is shown, indicating also the entrance and exit holes for the laser beam. The drilled holes exhibit diameters of 200 µm and 150 µm for the in- and outgoing beam, respectively, in order to keep the gas flow into the target chamber as low as possible and to avoid clipping of the IR and XUV beams. As the gas flow through these 200 µm openings is still high enough to rapidly increase the cumulative pressure, two introversive conical entrance and exit holes

of the internal chamber – large enough for the laser beam – minimize the gas flow conductance into the main chamber. This geometry furthermore reduces the XUV propagation distance in the comparatively high pressure environment thus decreasing absorption of the XUV photons. The gas ballast in the target chamber is removed with a 300 l/s turbomolecular pump, in combination with a side channel pump (on–tool booster), providing pressure values of 10^{-5} mbar in the main chamber and 10^{-2} mbar in the target chamber.

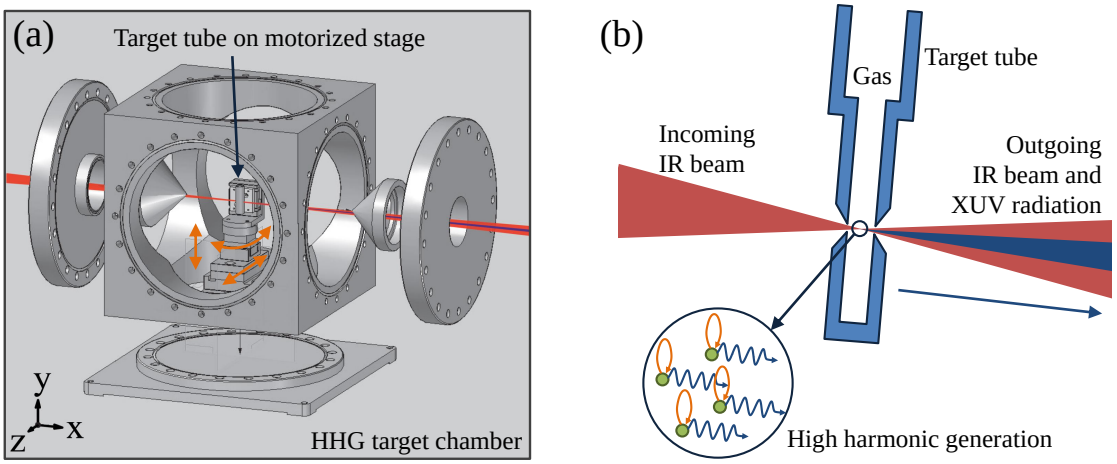

Figure 4.10: (a) Target chamber: HHG is achieved by focusing an intense ($\sim 10^{15}$ W/cm²) laser beam into a rare–gas target confined in a tube with small entrance (200 µm) and exit (150 µm) holes. The target tube mount features three degrees of freedom for alignment optimization. (b) Target tube: The cell is filled with rare gas at constant pressures of 50 – 200 mbar. The diameters of the entrance and exit holes are asymmetric thus leading to an asymmetric gas–flow emittance towards the opposite direction of the laser propagation.

There are several possibilities to optimize the HHG yield. Besides an alignment outside of the main chamber and a pre–alignment via a collinear HeNe-laser this includes adjustable pressures in the gas cell, as well as focal and target capillary positions. The latter involves three dimensions, i.e. torsion and the two axes perpendicular to the propagation direction of the laser.

Following the HHG process, both the XUV and the remaining IR beam propagate collinear towards the second internal, so called focusing chamber which again is independently pumped thus serving as the first of a two–step differential pumping stage. Here, pressures of 10^{-6} to 10^{-7} mbar are achieved. The chamber contains focusing optics for the XUV and IR beam which are mounted on the same breadboard as all other mirror mounts. This mechanical connection is essential for providing stable, well–defined path lengths, enabling two–color delay–dependent precision measurements.

At the XUV entrance position of the focusing chamber a motorized filter wheel with different metallic foils ranging from 200 to 600 nm thickness is implemented. This is nec-

essary to filter out the co–propagating IR light, as the thin foils are transparent for certain wavelengths in the UV range whereas IR light is absorbed. In addition, the filter wheel enables an effective pressure gradient between the main and the focusing chamber. Another purpose is to spectrally clean the XUV beam. The effects of Aluminum filters on the harmonics have been studied intensively [LM+05], showing that a spectral profile between 17 and 70 eV is obtained, which corresponds to the 10th to 40th harmonic. Furthermore, the filtering leads to a temporal reshape of the spectral profile, ideally flattening the spectral phase such that slightly positively chirped attosecond pulses or APTs are achieved [Pau+01]. An off–axis–parabolic curved mirror in the focusing chamber defines the position where the XUV and the probing IR beam are overlapped again. In order to pre–align this overlap temporally and spatially, the IR light from both paths must be used and, therefore, one of the filter positions is left vacant.

Details of the XUV focusing mirrors are given in [Gop09]. Briefly, the combination of a concave mirror with 5000 mm curvature and a cylindrical mirror with 60 mm curvature is implemented in order to focus both the sagittal and meridional rays at the same position in the target volume of the reaction microscope. The mirrors are coated with a highly reflective gold surface and are hit at a 6° grazing incidence angle, resulting in an estimated focal distance of 750 mm. This modified Kirkpatrick–Baez configuration [KB48], allows reflectivity values up to 80 % in a photon energy range between 30 and 50 eV. As a result, it is possible to provide 10^6 to 10^7 XUV photons per pulse in the interaction volume of the ReMi.

The following discussion will consider the IR beam path which is mainly used for the two–color pump–probe measurements. Here, it contains 30 % of the initial intensity. In the first step, the beam is guided to a motorized delay transition stage[8] which allows realizing time delays up to 3000 fs and, moreover, provides the possibility to initialize the time overlap in the ReMi during operation. The setup itself is mounted on a manipulation stage to increase the overlap range in cases where major changes are executed within the optical setup.

The IR path includes a $\lambda/2$–plate to optimize the polarization. Furthermore, the beam diameter is increased to $\sim$ 50 mm diameter in order to ensure a small focal volume in the experimental target. A motorized iris at the end of the path is operated to control the IR intensity; moreover, it determines the spatial IR alignment. As the XUV beam is fixed after the regular optimization procedure the spatial overlap can only be realized by a pair of motorized mirrors in the IR section. The spatial overlap condition is controlled by an image of the focal spot from the experimental target, mirrored by a CCD camera outside of the ReMi. Finally, the IR beam is guided into the focusing chamber through a low–dispersive 2 µm thin nitro-cellulose pellicle – again to maintain the pressure in the differential pumping

[8] PI Physik Instrumente, P–629.1CL PI Hera Flexure-Guided nano positioning Piezo Stage, 1500 µm with capacitive feedback.

stage in the 10^{-6} mbar range. Within the internal chamber the next optical component for the IR beam is the previously mentioned off–axis–parabolic curved mirror of 600 mm focal distance, defined by an exact 90° reflection angle to avoid astigmatism. This mirror exhibits a hole of 3 mm diameter for the XUV path as indicated in Figure 4.9. At this position, both beam paths overlap again and the corresponding XUV and IR lasers propagate collinearly towards the interaction volume of the ReMi. Prior to that, the laser pulses exit the chamber through an additional pellicle – perforated in the center to prevent XUV–photon absorption – into the second differential pumping stage which is operated at a pressure of 10^{-8} mbar.

In this configuration, the XUV and IR pulses remain phase correlated, since both originate from the same fundamental pulse. As a consequence, reasonable pump–probe experiments are feasible without initial CEP–phase stabilization, as changes on the CEP equally affect both pulses[9].

Although one objective of the design of the HHG chamber is high interferometric stability, the relatively large number of optical parts can cause slow drifts on the sub–femtosecond time scale. For measurements where the aimed temporal resolution is of comparable order, inevitable drifts have to be recorded. This has been implemented successfully for sideband oscillation measurements in rare gas atoms, as demonstrated in [Rie12].

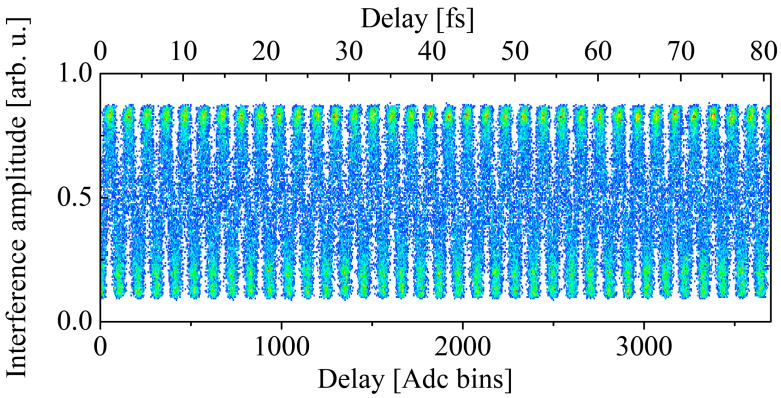

Figure 4.11: Additional delay control by a correlated He–Ne interferometer. The corresponding interference signal is simultaneously recorded with ionization events in the ReMi and provides a quantitative measure of the delay range.

Another feature within the setup is an independent delay-range measurement provided by an additional HeNe interferometer which is connected to the IR delay stage. This device enables a quantitative measurement of the delay range: however, it cannot be used to determine interferometric drifts during an experiment. An example of this additional interferometric signal is given in Figure 4.11. Further details regarding the high–harmonic chamber are represented in [Rie12].

[9] CEP stabilization is unnecessary for pulse durations above 8 fs, such as used in the conducted measurements.

4.3.2 Characterization of the high–harmonic radiation and energy calibration

The higher harmonic light is dispersed by a grating and detected by a high–sensitive XUV–CCD spectrometer[10] mounted at the side of the HHG chamber. The spectrometer is primarily used to optimize the HHG yield and subsidiary to obtain a photon–energy calibration. Information of the XUV radiation is further obtained by the photoelectron–energy spectrum from ionization experiments in the ReMi. The latter method, however, does not represent the exact intensities of the harmonics, since the yield strongly depends on the ionization cross section, and single harmonic peaks may be enhanced by atomic and molecular resonances. In Figure 4.14 four spectral profiles, resulting from both techniques are shown in a combined diagram. Here, the first three rows represent photoelectron–energy spectra, measured in the ReMi for single–photon ionization of argon, neon and helium atoms. The spectra are shifted with respect to each other due to different ionization thresholds of the target species. The last spectrum in Figure 4.14 is recorded with the XUV–CCD camera and the observed discrepancies to the upper profiles will be discussed in the description of the spectrometer setup.

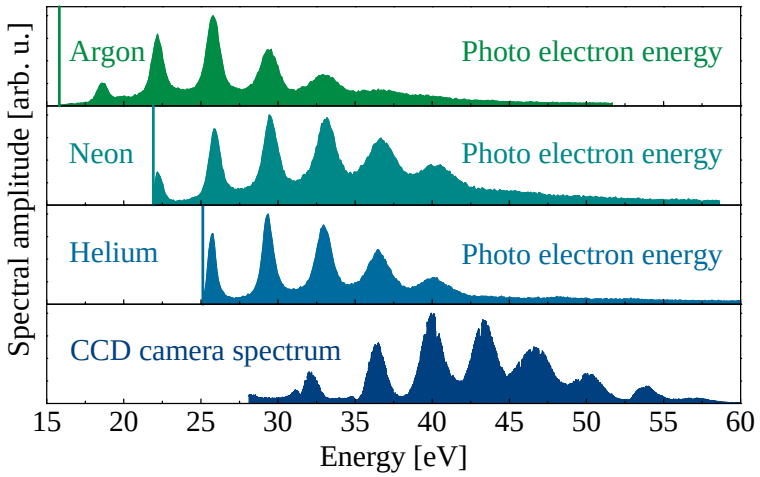

Figure 4.12: Three photoelectron spectra for single ionization of argon, neon and helium atoms in the ReMi. The vertical lines denote the corresponding ionization thresholds. The bottom spectrum is recorded with the XUV–CCD camera.

A motorized flap mirror between the target and the focusing chamber is used to direct and focus the XUV pulses on a freestanding transmission grating into the camera. A 800 nm thick aluminum foil filters the beam from the co–propagating IR and the lower harmonic frequency components. Internal noise can be reduced by cooling the camera chip to −55 °C. The method to extract a complete high–harmonic spectrum is described

[10] Pixis–XO, Princeton Instruments Inc., Trenton, NJ 08619, USA, www.pricetoninstruments.com.

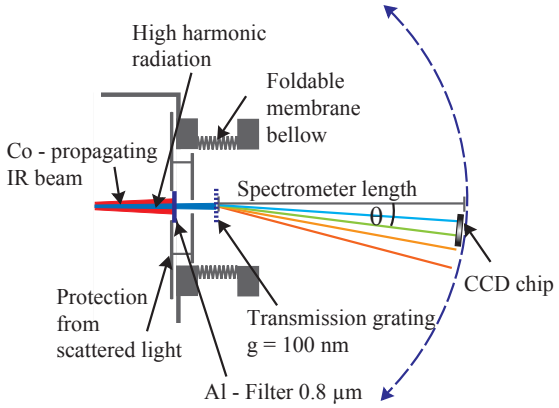

Figure 4.13: Working principle of the high–harmonic radiation characterization via grating and XUV–CCD camera.

in detail in [Rie12]. Briefly, different parts of the harmonic spectral profile are measured by varying the angle of the spectrometer around the grating. Accordingly, the separately recorded spectra must be merged and, therefore, all angles as well as the exact focal–spot position on the grating must be known. While the angular position is precisely determined in daily alignments, the position onto the grating varies, leading to considerable shifts of the harmonic positions (i.e. in the frequency domain). This comprises an exact energy calibration with the camera.

Furthermore, the camera is not sensitive in the low–frequency domain resulting in missing signal at low photon energies between 15 and 25 eV in the bottom spectrum of Figure 4.12. The fact that this energy range is not detected efficiently in the CCD camera can be related to five technical issues:

- The filter properties of the aluminum foil provide a photon–transmission window of approximately $17 - 72\,\mathrm{eV}$.
- The cross section for XUV–photon absorption in the target gas (argon atoms) is high between $15 - 30\,\mathrm{eV}$, thus reducing the HHG yield by 10 %.
- The quantum efficiency of the XUV–CCD chip for photon energies larger than 25 eV is three times higher than for photon energies of 15 eV.
- The gracing incidence reflectivity on silver and gold coated mirrors decreases for photon energies lower than 30 eV.
- The diffraction efficiency of the transmission grating doubles between photon energies of 30 and 60 eV.

The reduction of high–harmonic light yield in the high–energetic part of the bottom spectrum in Figure 4.12 corresponds to the cutoff energy for HHG in argon at given laser

intensities. Usually, the cutoff region is expected to be at larger values[11]; however, due to a high target density, a saturation effect shifts the cutoff to the measured value of 60 eV [Dac+09].

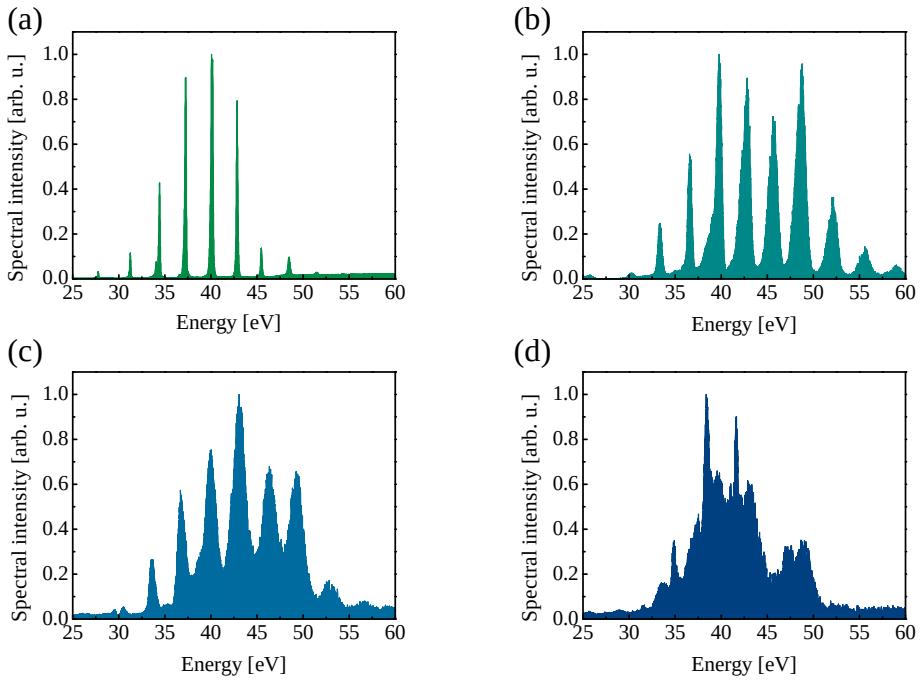

Figure 4.14: Four different HHG spectra. Spectrum (a) corresponds to the fundamental IR spectrum from the amplifier. (b), (c) and (d) belong to hollow–core fiber broadened spectra with glass substrates in the beam path, (b) 2 mm, (c), 0.5 mm and (d) 0 mm. With increasing glass thickness, dispersion increases the pulse duration and thus the high–harmonic peaks become narrower.

The inclusion of photoelectron–energy spectra from ionization events in the ReMi can circumvent the previously mentioned energy–calibration problem with the XUV–CCD camera. As an example, it is convenient to consider two distinct and separated energy peaks E_{e1} and E_{e2} within the photoelectron energy spectrum, where the first one is close to the ionization threshold of the target species. Starting from the atomic ionization potential I_p, consequently the first energy peak will be the signature of the lowest harmonic order n_1, which is able to ionize the atom. The exact energies can be determined because the separation of both peaks as well as the energy position of the first peak must fulfill the

[11] For a laser intensity of $3 \cdot 10^{14}$ W/cm² the cutoff reaches 72 eV.

following equations with ΔE_{HH} being the high–harmonic spacing of $2\hbar\omega_0$:

$$\Delta E_{HH} = \frac{E_{e2} - E_{e1}}{n_2 - n_1} \tag{4.9}$$

$$\Delta E_{HH} = \frac{2}{n_1}(I_p + E_{e1}) \tag{4.10}$$

The result from this indirect calibration method can be further transferred to the recorded harmonic CCD camera spectrum up to an accuracy of $\pm 0.1\,\mathrm{eV}$.

Last but not least, the high–harmonic spectrum allows to retrieve the pulse durations of single attosecond pulses within APTs, as the pulse length correlates with the spectral width of the single harmonics. This is shown in Figure 4.14 for four XUV spectra, generated with IR pulses with different durations.

4.4 Reaction microscope

Studying electron correlation and multi–fragmentations in quantum systems is technically challenging, especially if the full solid angle 4π is to be covered. The main difficulty arises from the different masses and energies of the corresponding particles which demand drastically deviating sets of traditional spectrometers.

A detection system circumventing these problems is the so called reaction microscope (ReMi) allowing coincident and fully differential cross–section measurements of atomic and molecular ionization reactions [Ull+03]. The complete reconstruction of such processes enables the possibility to identify and separate distinct reaction channels and, thus, observe specific quantum dynamical effects.

This technique has already been applied successfully in numerous atomic and electronic collision schemes, as well as in light field interactions with atoms and small molecular systems. The next sections will give a brief description of general properties of ReMis followed by a discussion on energy and momentum resolution for electrons and typical ion species.

4.4.1 Reaction microscope design and working principle

The basic principle of a ReMi is an event–by–event, 4π solid angle, momentum–resolved measurement of all charged particles emerging from an ionization process by the use of superimposed electric and magnetic projection fields. The momentum vectors of the particles correspond to the asymptotic final state of the reaction under investigation [Sch12]. Still, providing sufficient statistics on a certain reaction kinematics of interest, often requires long recording times, in particular if the data is dominated by other processes with higher cross sections. The full three–dimensional momentum of each particle is reconstructed by its impact position on the detector and its time–of–flight (ToF), which is triggered in the

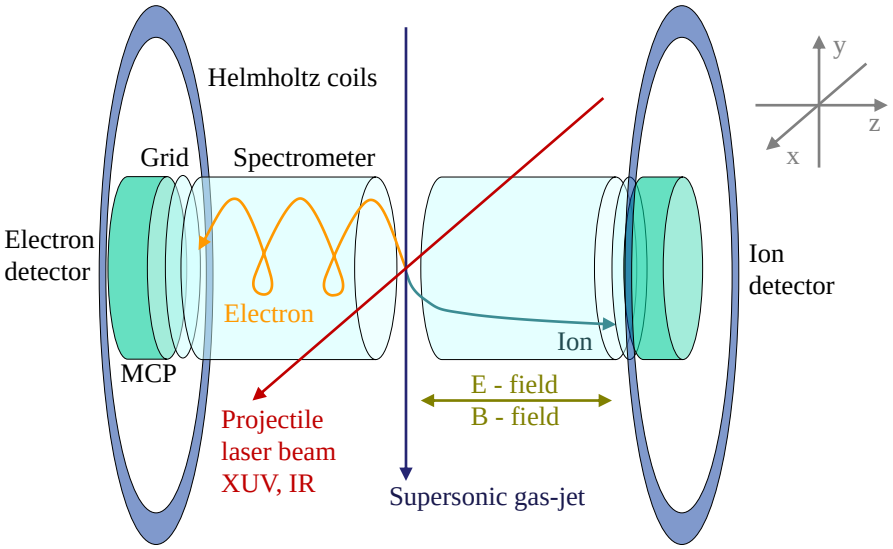

Figure 4.15: ReMi with relevant features and geometries. The laser beam, the spectrometer axis and the supersonic gas jet are perpendicular to each other. A series of spectrometer plates and a pair of coaxial Helmholtz coils provide homogeneous electric and magnetic fields, respectively. Created charged fragments are projected onto position sensitive detectors consisting of MCP stacks and delay line anodes. The three–dimensional momentum reconstruction follows from the time–of–flight and hit–position information.

presented setup by the laser pulse signal on an external photo diode.

Figure 4.15 illustrates the main ReMi components and their orientation in the coordinate system (laboratory frame) used throughout this work. This includes the gas jet ($-y$), the projectile laser beam (x) and spectrometer axis (z).

The detection of electrons and ions is realized by a stack of two charge–multiplying micro–channel plates (MCPs) followed by a crossed pair of delay line anodes. The MCPs are set on a high electric potential, such that charged particles leaving the spectrometer volume are accelerated strongly and eventually hit the front surface of the MCP assembly. Hence, the high impact energy causes the release of secondary electrons which are further multiplied within the channels of the MCPs thus leading to a number of 10^7 to 10^8 electrons. The resulting electron cloud will hit the copper–wire pairs and induce signals that travel to both ends of the delay line anode wires [Jag+02]. The time difference between two corresponding capacitively read–out, pulsed signals finally encodes one of the two position coordinates, as illustrated in Figure 4.16 (a), where the wire pair (Lecher configuration) is depicted as a single wire. Further technical details on the detection, such as signal processing and data acquisition are presented in [Gop09].

In ionization experiments with a ReMi it is important that the initial thermal momentum spread of the target atoms or molecules is small. Furthermore, the interaction volume must

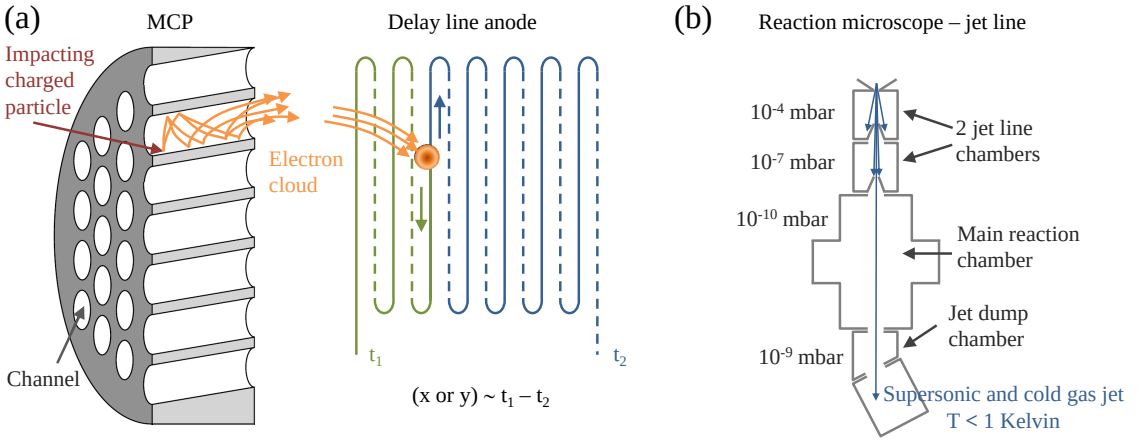

Figure 4.16: Technical schemes: (a) representation of the detector consisting of multi channel plates and delay line anodes (Figure is based on [Pfl08]). (b) The target beam generation is illustrated as well as typical pressure values in the ReMi.

be well localized. Both requirements can be fulfilled using a supersonic gas jet which is generated by the expansion of a gas through a thin nozzle, followed by two skimmers with small apertures. Figure 4.16 (b) illustrates the resulting collimation of the jet by blocking particles with a momentum component perpendicular to the propagation direction. This can be understood as a conversion of the initial three–dimensional Maxwell–Boltzmann distribution into a well defined supersonic gas jet with a one–dimensional motion. In the presented setup, the final diameter of the extending gas beam can be specified to 1.6 mm. For a technical review the reader is referred to the work of [Sch+97] and the textbook by [Mil88] which explains the theoretical treatment of the supersonic gas expansion.

As described in section 4.3.1, the XUV and IR foci are adjusted and overlapped on the gas target, thus defining the reaction volume of the ReMi and initializing ionization and fragmentation processes. Released electrons and ions are then projected onto opposite position sensitive detectors via a homogeneous and stable electric field, provided by 32 spectrometer plates, spaced by 7 mm. An electric field is not sufficient to provide comparable momentum resolution and acceptance for both particles. The reasons for this are the different masses and velocities of ions and electrons. For example, ions and electrons resulting from a single ionization event exhibit the same momentum; however, their kinetic energies ($\sim p^2/m$) differs by 3 to 4 orders of magnitude. As the radial hit–coordinate (x and y) of a charged particle is proportional to $\sqrt{E_{\mathrm{kin}}/U_{\mathrm{extr.\ field}}}$ there is no appropriate extraction field that simultaneously provides an equal momentum resolution for ions and electrons.

A superimposed, constant magnetic field solves this problem by forcing particles with a non–vanishing radial momentum component onto helical trajectories, thus confining them

into a smaller projection area. For magnetic field strengths in the sub 10 G range (and electric fields above 10 V/cm), ion trajectories will remain almost unaffected, whereas electrons show spiral traces in the spectrometer. A drawback of this additional field is the time–of–flight dependence of the transverse (with respect to the spectrometer axis) momentum resolution. The magnetic field in this setup is generated by a pair of coaxial Helmholtz coils positioned outside of the vacuum chamber and centered around the interaction volume of the ReMi, as shown in Figure 4.15.

4.4.2 Calculation of momenta

Momentum spectroscopy with a ReMi is characterized by a large solid angle detection for all charged particles, simultaneously achieving excellent resolution at low energies for all emission angles and reaching reasonable values for large momenta which, however, strongly depend on the emission characteristics. In this context, it is necessary to discuss the reconstruction algorithm for the momenta of ions and electrons i.e. how the three–dimensional momentum of the particles is retrieved from the time–of–flight and impact position on the detector which will be briefly presented in the following section (details can be found in [Jes+04; Fis03; Sen09]). As the basic principle of the ReMi is the projection of charged particles by means of electric and magnetic fields ($\vec{E}$ and $\vec{B}$) the equation of motion, governed by the Lorentz force,

$$m \cdot \frac{d^2}{dt^2}\vec{r} = q \cdot (\vec{E} + \vec{v} \times \vec{B}) \quad \text{, has to be solved.} \tag{4.11}$$

This task can be simplified since the detection geometry suggests to apply cylindrical coordinates for the calculation of the momenta ($p_{\parallel} = p_z$ and $p_{\perp} = \sqrt{p_x + p_y}$), as indicated in Figure 4.15.

Figure 4.17 shows the raw electron and ion distributions from which the momentum components are calculated. The time–of–flight of the ions depends on their charge/mass ratios, as demonstrated in the spectrum. Besides contributions from the target gas, here Ar^+ ions, one observes in the logarithmic plot contamination by ionization of the rest gas, and, interestingly, a peak that is assigned to singly charged dimers that are formed during the supersonic gas expansion. The momenta of the ions along the extraction field ($p_{\parallel} = p_z$) is encoded in the width of the corresponding ToF distribution. p_x and p_y are calculated from the ion position spectrum. Here, the signals from the rest gas and target ions are located in a broad (horizontal) band and a round spot, respectively. Note, the target ions are displaced in the y–direction from the center of the rest gas band due to the jet–momentum propagation along $-y$. In addition to these signal, "dark" counts are observed as well.

Electron ToF and position spectra cannot be intuitively understood due to their complicated motion in the $\vec{E}$ and $\vec{B}$ fields. Furthermore, electrons emerging from different

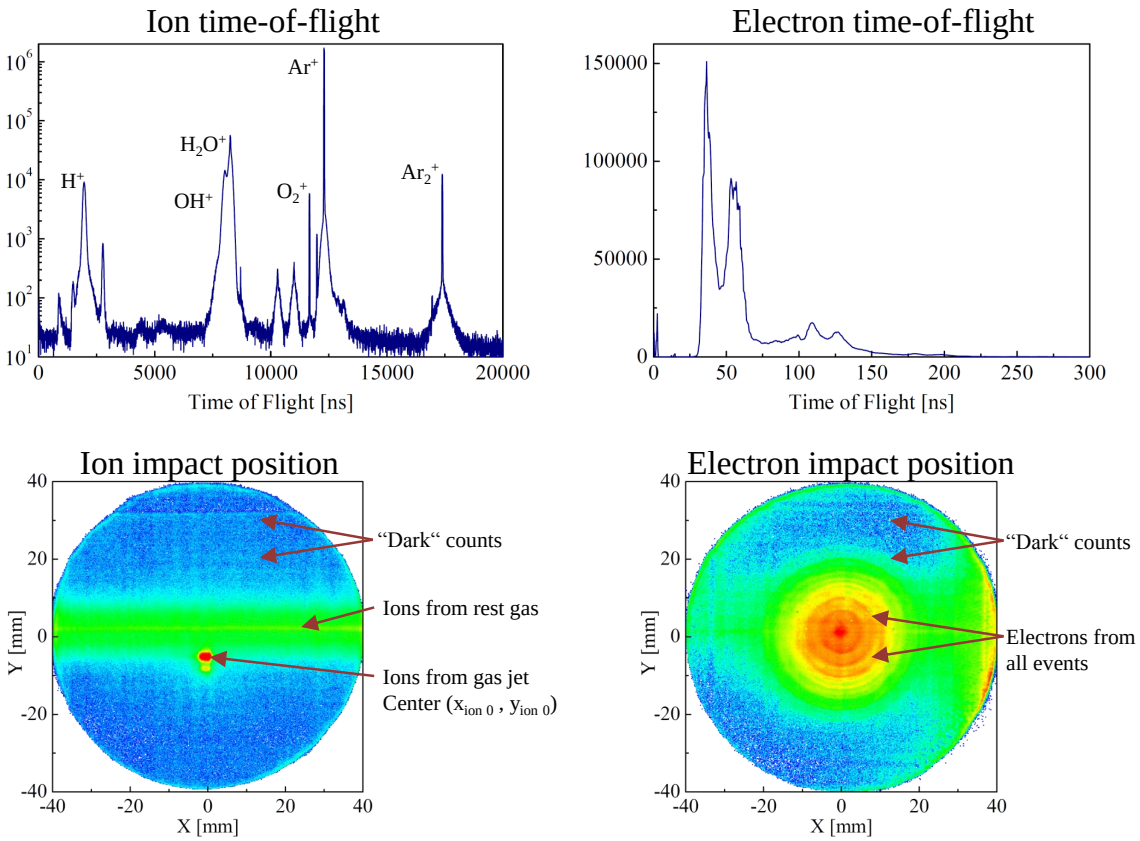

Figure 4.17: Measured ToF and impact position of ions and electrons for single ionization of Argon atoms by XUV photons (see text).

ionic species cannot be distinguished without a coincident detection of the ions. The identification of such correlated ions and electrons is done in a separate evaluation step and will be discussed in section 4.4.5 in more detail. Nevertheless, it is worth mentioning that coincident events are determined, for instance, by their momentum sums $p_{x\,\mathrm{tot}}$, $p_{y\,\mathrm{tot}}$ and $p_{z\,\mathrm{tot}}$, which all must be zero. Note, the momentum sums include charged as well as neutral fragments but not the momentum of the projectile photon, even if the energies are in the XUV range[12]. This further implies that a process with n particles in the final state can still be reconstructed if only $n-1$ are detected.

In the end of this chapter a discussion about experimental resolution and acceptance will illustrate the significance of providing a cold and collimated target beam, taking care for extraction–field homogeneities and a well–considered choice of measurement parameters.

[12] Here, the highest photon energies correspond to $\sim$ 40 eV which equals a momentum transfer of 0.01 au.

Longitudinal ion momentum $p_{\mathrm{ion}\parallel}$

The longitudinal ion momentum $p_{\mathrm{ion}\parallel}$ can be deduced from the time–of–flight t_{ion} which in turn depends on the charge/mass ratio q/M, the initial velocity $v_{\mathrm{ion}\parallel}$ gained in the the generating ionization or dissociation process and the emission direction. In collision experiments with massive particles where the interaction volume is usually considerably large, ReMis incorporate compensating drift regions to maintain the resolution [Fis03]. Here, due to the small laser foci a drift distance is not applied thus leading to a relatively simple equation of motion in longitudinal (z) direction:

$$s_B \;=\; v_{\mathrm{ion}\parallel}\, t_{\mathrm{ion}} \;+\; \frac{1}{2} a t_{\mathrm{ion}}^2 \qquad \text{with} \qquad a \;=\; \frac{q}{M}\,\frac{U}{s_B} \qquad \Rightarrow \tag{4.12}$$

$$p_{\mathrm{ion}\parallel} \;=\; M\frac{s_B}{t_{\mathrm{ion}}} \;-\; \frac{1}{2} qU \frac{t_{\mathrm{ion}}}{s_B} \quad , \tag{4.13}$$

with the acceleration length s_B and the extraction voltage U. Here, a value of the exact field is not important since small deviations can be calibrated using energy and momentum conservation in single ionization by XUV photons of well–known energy.

Transversal ion momentum $p_{\mathrm{ion}\perp}$

Ions which only exhibit a longitudinal momentum hit the detector at a specified and confined position ($x_{0\ \mathrm{ion}}$, $y_{0\ \mathrm{ion}}$) (see Figure 4.17). In principle, the calculation of $p_{\mathrm{ion}\perp}$ involves the magnetic field strength; however, even for low electric fields of 5 to 20 V/cm, the corresponding forces are comparatively small and may be neglected. Hence, for ions with non–vanishing transversal momentum, only the time–of–flight t_{ion} and the relative displacement ρ from ($x_{0\ \mathrm{ion}}$, $y_{0\ \mathrm{ion}}$) are important.

$$v_{\mathrm{ion}\perp} \;=\; \frac{\rho}{t_{\mathrm{ion}}} \qquad \text{with} \qquad \rho = \sqrt{(x_{\mathrm{ion}} - x_{0\ \mathrm{ion}})^2 + (y_{\mathrm{ion}} - y_{0\ \mathrm{ion}})^2} \qquad \Rightarrow \tag{4.14}$$

$$p_{\mathrm{ion}\perp} = \frac{\rho\, M}{t_{\mathrm{ion}}} \qquad \text{or} \qquad p_{\mathrm{ion}\ x} = \frac{(x_{\mathrm{ion}} - x_{0\ \mathrm{ion}})\, M}{t_{\mathrm{ion}}} \qquad \text{and} \qquad p_{\mathrm{ion}\ y} = \frac{(y_{\mathrm{ion}} - y_{0\ \mathrm{ion}})\, M}{t_{\mathrm{ion}}}$$

Note that the ions exhibit a significant momentum in the negative y-direction due to their initial velocity in the supersonic gas jet, leading to a shift in the position distribution with respect to the detector centroid. This is taken care of in good approximation by considering the maximum of the impact position of ions from the jet (see Figure 4.17) as ($x_{0\ \mathrm{ion}}$, $y_{0\ \mathrm{ion}}$), i.e. performing a transformation of coordinates into the moving jet frame.

In view of the molecular frame photoelectron angular distributions which are presented in section 4.4.6, the cartesian momentum components $p_{\mathrm{ion}\ x}$ and $p_{\mathrm{ion}\ y}$ can be used to extract the azimuthal emission angle ϕ:

$$p_{\mathrm{ion}\ x} \;=\; p_{\mathrm{ion}\perp}\cos(\phi) \qquad \text{and} \qquad p_{\mathrm{ion}\ y} \;=\; p_{\mathrm{ion}\perp}\sin(\phi) \tag{4.15}$$

Longitudinal electron momentum $p_{e\parallel}$

Electrons, due to their lower mass, are forced onto helical trajectories by the magnetic field which on the one hand impedes the reconstruction of the correct final momentum but, on the other hand, provides a simple method to confine and, thus, analyze electrons emitted into the full solid angle at moderate electric field strengths that are required for high–resolution ion momentum spectroscopy. Given that $\vec{E}$ and $\vec{B}$ are homogeneous and exactly parallel to the spectrometer axis, the longitudinal momentum calculation will be the same as for the ions, see equation (4.13).

Transversal electron momentum $p_{e\perp}$

In contrast to the ions, the reconstruction of the transversal momenta of the electrons strongly depends on the magnetic field. Furthermore, electron trajectories are much less localized – due to the low electron mass – and may easily sample the entire spectrometer volume. Therefore, $\vec{E}$- and $\vec{B}$- field homogeneities have to be guaranteed over the complete extraction volume. In this context, the Helmholtz coils must be large enough and aligned such that they cancel out the earth magnetic field, or more precise, the perpendicular component with respect to the magnetic field axis (z).

For electrons, the calculation of $p_{e\perp}$ follows from equilibrating centrifugal and magnetic forces:

$$\frac{mv_{e\perp}^2}{r} = ev_{e\perp}B \qquad \Rightarrow \qquad p_{e\perp} = erB \tag{4.16}$$

The radius r of the spiral trajectory is not directly accessible; however, it can be determined, similarly to the ion case, from the position on the detector and the ToF, as illustrated in Figure 4.18 (a). Here, an electron emitted with the transversal momentum $p_{e\perp}$ and the azimuthal emission angle ϕ, will start a cyclotron motion with radius r and angle α which depends on the cyclotron frequency[13] and the electron ToF (t_e) as

$$\alpha = \omega_c t_e = \frac{eB}{m} t_e \qquad \text{such that} \qquad |\sin(\frac{\alpha}{2})| = \frac{R}{2r} \quad . \tag{4.17}$$

Trigonometric considerations then lead to the transversal momentum of the electron

$$r = \frac{R}{2|\sin(\frac{1}{2}\omega_c t_e)|} \qquad \Rightarrow \qquad p_{e\perp} = \frac{ReB}{2|\sin(\frac{1}{2}\omega_c t_e)|} \tag{4.18}$$

and to its azimuthal emission angle $\phi = \phi_{\mathrm{detector}} - \frac{1}{2}\omega_c t_e$. The retrieval of the cartesian x and y momenta then proceeds with ϕ, in analogy to the ion–momentum equations (4.15).

Equation (4.18) indicates that the transversal momentum is ambiguous for ToFs that correspond to an integer multiple of the cyclotron time, or, $\alpha = n \cdot 2\pi$. Here, electrons

[13] In typical experiments, where ions and electrons are supposed to be measured in coincidence, the extraction voltage varies from 40 to 500 V, which corresponds to cycle numbers between 4 and 0, respectively.

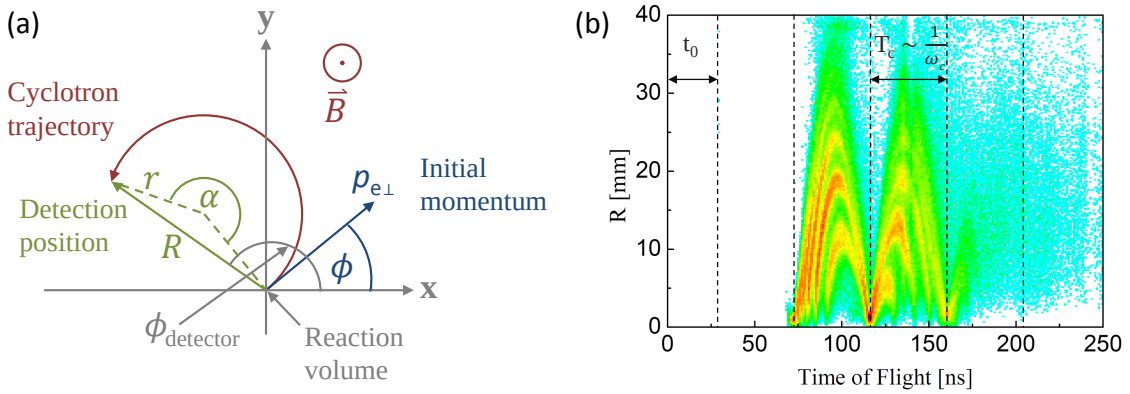

Figure 4.18: (a) An electron trajectory projected onto the detector plane. The cyclotron motion, the original electron emission direction ϕ and transverse momentum $p_{e\perp}$ as well as the detection position R are shown. (b) The correlation between the radial positions and the corresponding ToF values of the electrons provide the cyclotron frequency by analysis of the periodic structure. The experimental offset time zero t_0 can also be deduced and applied to the calculations.

emitted with any $p_{e\perp}$ and ϕ hit the detector at $R = 0$ and, accordingly, the evaluation of equation (4.18) becomes meaningless. These considerations further show that the resolution of the electron transversal momentum is a non–trivial function of R which will be elaborated in the next section. Nevertheless, this obvious drawback can be compensated by choosing $\vec{E}$ or $\vec{B}$ such that momenta of experimental interest are not affected or at least, influenced only on one side of the momentum hemisphere.

The magnetic field can be calibrated by inspecting the appearance of characteristic nodes in the correlated position and ToF spectrum as shown in Figure 4.18 (b). Here, it is possible to measure both, the cyclotron frequency (time–interval in between times with $R = 0$) and a time offset between the recorded ionization event and the laser triggering signal. The latter corresponds to the absolute time zero t_0, where the ionization takes place. It is retrieved by extrapolation of times for $R = 0$.

4.4.3 Acceptance

In contrast to other state–of–the art detection systems, such as velocity–map–imaging [Bor+96; EP97] spectrometers, ReMis are capable of measuring charged particles with completely different charge/mass ratios at comparable resolutions. Despite this immense advantage, there are restrictions connected to the detection design as well as to the choice of parameter settings which will be elucidated in the following.

The spectrometer acceptance is determined by the highest detectable kinetic energies of charged particles originating from ionization events with respect to their emission directions. Here, geometrical parameters are important, such as the acceleration or spectrom-

eter length s_B, the size of the MCP detection area $\pi R^2_{\mathrm{detector}}$ as well as the applied field strengths, as shown in Figure 4.19.

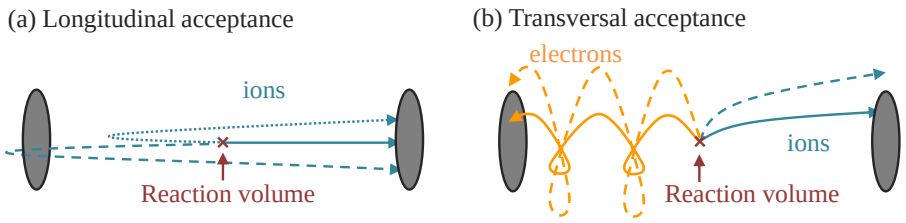

Figure 4.19: (a) Acceptance for longitudinal momenta of the ions (equally for electrons). The particle with the dashed trajectory exhibits a momentum which is too large to be decelerated within the length of the spectrometer at a given electric field. (b) Acceptance for transversal momenta of ions (green) and electrons (orange). Events corresponding to the dashed trajectories are not recorded.

For particles propagating along the spectrometer axis – this includes both, the forward and backward directions with respect to the corresponding detector – only electrons and ions emitted away from the respective detectors, restrict the acceptance. If their energy is too high, the deceleration distance between reaction zone and returning point, given by the electric field, exceeds the available spectrometer range. The longitudinal acceptance for a particle of charge q and mass M in the direction away from the respective detector can therefore be quantified in SI units as follows:

$$E_{\parallel}^{\mathrm{acceptance}} = qU \quad \Leftrightarrow \quad p_{\parallel}^{\mathrm{acceptance}} = \sqrt{2MqU} \tag{4.19}$$

For events where particles are emitted perpendicular to the spectrometer axis, ions and electrons have to be considered separately according to the vastly different magnetic field dependencies of their trajectories. As electrons are radially confined by a given value of B the full acceptance for any azimuthal emission angle ϕ can be expressed as:

$$E_{\perp}^{\mathrm{e^-\ acceptance}} = \frac{(qBR_{\mathrm{detector}})^2}{8\,m_e} \quad \Leftrightarrow \quad p_{\perp}^{\mathrm{e^-\ acceptance}} = \frac{qBR_{\mathrm{detector}}}{2} \tag{4.20}$$

Here, electrons with energies above the acceptance are still measurable as long as their perpendicular trajectory component does not extend the detector radius at the moment when the electron strikes the detector, as represented by equation 4.18.

In most experiments with the present XUV source, the electron energies range between 0 and 24 eV. Hence, it is convenient to set the magnetic field to a defined value of 7.88 G (with the coils aligned such that the earth magnetic field compensation is optimized), corresponding to an acceptance for all ϕ of 21.8 eV.

The perpendicular and longitudinal ion acceptances are both functions of the electric field strength alone. For vertical trajectories the ratio between the detector radius and the

spectrometer length becomes relevant:

$$E_{\perp}^{\text{ion acceptance}} = \frac{qU}{4}\frac{R_{\text{detector}}^2}{s_B^2} \quad \Leftrightarrow \quad p_{\perp}^{\text{ion acceptance}} = \sqrt{\frac{MqU}{2}}\frac{R_{\text{detector}}}{s_B} \tag{4.21}$$

Ions generated in single photoionization usually gain a low amount of kinetic energy. Therefore, low extraction voltages are already sufficient for detection. This characteristic changes drastically in photon–induced fragmentation reactions, i.e. dissociation and Coulomb explosion, where ions may reach up to 10^4 times higher energies.

These observations suggest to set the extraction voltage to extreme values in order to guarantee 100 % acceptance. However, this affects the measurement resolution as the particles are projected to a smaller detector area and their time–of–flight window becomes narrower. In fact it is convenient to select field strengths such that the resolution is maximized, without losing events of interest.

4.4.4 Resolution

The spectroscopic precision in the investigation of ionization processes is limited by several experimental parameters and technical details, some of which are listed in Table 4.1.

Resolution related criterion	Parameter	Influence
Spatial detector resolution	$\Delta R = 0.1\,\text{mm}$	$p_{\perp}$
Time–of–flight resolution	$\Delta t \approx 1\,\text{ns}$	$p_{\parallel}$
Thermal velocity distribution of the gas jet	$\Delta T = \pm 1\,\text{K}$	$p_{\perp}$, $p_{\parallel}$
Target volume (beam area)	$A \approx 1.6\,\text{mm}$	$p_{\perp}$, $p_{\parallel}$
Focal volume (Rayleigh range IR beam)	$z_R \approx 1\,\text{mm}$	p_x
Focal volume (Rayleigh range XUV beam)	$z_R \approx 10\,\text{mm}$	p_x
Focal volume (beam waist XUV and IR beam)	$w_f \approx 30\,\mu\text{m}$	p_y, $p_{\parallel}$
Inhomogeneity (electric field)	$\sigma\vec{E}$	$p_{\parallel}$
Inhomogeneity (magnetic field)	$\sigma\vec{B}$	$p_{\perp}$

Table 4.1: List of criteria influencing the resolution. Several uncertainty values are specified and related to momentum components.

As shown, most factors solely influence specific momentum components. Furthermore, the resolution varies for different ionic species and especially for electrons due to their higher charge/mass ratio.

This is not the case for the first two items in Table 4.1 as they are related to the detection geometry, the corresponding electronic readout and the applied extraction fields,

but not to the properties of the particles. Hence, the uncertainty values in the position ΔR and the time–of–flight Δt in general determine the highest possible resolution to be achieved at given field strengths in experiments. Further degradation of the resolution is then given by uncertainties in the source position, which in turn, is related to the target beam extension, its thermal spread, as well as laser focusing parameters. The reaction volume can be specified by the confinement of the beam waist in the XUV laser focus in y- and z-directions to 30 µm and by the target (1.6 mm) in x-direction, as the Rayleigh range of the XUV exceeds the extension of the target. Therefore, the momentum distribution in the laser propagation direction is expected to be larger; however, this was not observed. In fact, the resolution is constant within the full $p_\perp$ area, suggesting a small rotationally symmetric target volume.

The design and operation of the super–sonic gas jet (see Figure 4.16) provides cold target particles with a defined momentum in the $y-$direction and a small thermal spread of 1 K [MFK03]. Such a cold target beam is necessary as the average ion momentum at room temperature already reaches values of a few atomic units. This is comparable to momenta gained in typical ionization and dissociation processes which would be otherwise indistinguishable. For the electron resolution, the target temperature is of minor importance and can be neglected.

Further resolution aggravation can be assigned to field inhomogeneities which include declined field vectors with respect to the spectrometer axis, as well as gradients in the field strengths. Both factors are minimized by careful design accompanied by electric field simulations, stable power supplies and alignment tests of the Helmholtz coils.

$\Delta p_\parallel(H^+)$	$\Delta p_\perp(H^+)$	$\Delta p_\parallel(e^-)$	$\Delta p_\perp(e^-)$
0.1 au	0.3 au	0.06 au	0.1 au

Table 4.2: Momentum resolution for H^+ ions and electrons from the dissociative ionization experiments presented in chapter 5.

Besides the mentioned difficulties of resolving electron momenta with a well–defined resolution and providing a narrow velocity distribution of the target, it is important to adjust the data evaluation parameters correctly, such that they correspond to the ReMi settings in the experiment. Uncertainties and discrepancies typically arise in parameter settings, such as the spectrometer voltage, the magnetic field, the center of the position distributions and the origin of the time–of–flight t_0. For single ionization with APTs the sharp photoelectron energy peaks completely reflect the high–harmonic spectrum, since the ions retain a negligible recoil energy. As the high–harmonic energies are fixed, it is possible to calibrate the electron energy spectrum to an accuracy of 0.1 eV. The exact procedure is described in section 4.3.2. In dissociation events of two–atomic molecules, the photon energy is equally distributed over electrons and ions; however, the total energy

of the system again shows the clear signature of the harmonic spectrum, enabling a clean energy calibration of both particles. An example for momentum resolution values, obtained in the experiments in chapter 5 are shown in Table 4.2.

4.4.5 Coincidence measurements

After calculating and calibrating vector momenta and energies of electrons and ions separately, the next task consists of an analysis of ion–electron correlations or, in general, of coincident events. In experiments with ReMis there exist several methods to identify coincident events, as shown in Figure 4.20 for three different measurements involving XUV radiation. Figure 4.20 (a) presents a simple approach by investigating the z-momentum sum $p_{z\,\mathrm{sum}}$ of all particles (H_2^+ and e^-) for single photoionization of H_2 molecules. Note, similar plots are provided for $p_{x\,\mathrm{sum}}$ and $p_{y\,\mathrm{sum}}$. In such ionization processes with negligible initial photon momentum, the total momentum of the system is zero. Due to the finite momentum resolution discussed before, the sum values form a narrow distribution around zero, resembling the so called "true" coincidences.

Obviously, the count rate does not completely disappear for $p_{\mathrm{sum}} > |\Delta p_{\mathrm{resolution}}|$ due to "false" coincidences. These events have several potential origins, such as ionization along the laser propagation axis of rest gas atoms in the vacuum chamber, as well as contamination of the target jet. Furthermore, false coincidences can result from false sorting. This is in particular the case when the total ionization rate exceeds the repetition rate of the laser such that electrons and ions generated within the same laser pulse, but emerging from different target atoms or molecules, are correlated with each other. Another problem arises with scattered XUV photons which generate electrons at the spectrometer plates and the detector frame. Although it is possible to exclude parts of these signals by applying conditions, they interfere in the overall electron signal and, accordingly, the number of measured coincident events is reduced. For these reasons, it is necessary to optimize the alignment towards minimized scattered XUV photons, low rest–gas ionization and detection yields significantly smaller than the laser repetition rates.

The momentum sum in Figure 4.20 (a) can also be employed to reconstruct momenta of missing fragments, such as neutral particles, which are not detected. Naturally, this prevents the applicability towards false coincidences; however, it enables access to the full kinematics of the process under investigation.

Another example for a coincidence spectrum is given by the doubly–differential energy diagram in Figure 4.20 (b), showing the Coulomb explosion of D_2 molecules via XUV and strong IR laser fields. The two resulting D^+ fragments gain similar energies during the repulsion. Therefore, true coincidences do not correspond to the horizontal and vertical lines.

A third, self–evident method to identify coincidences is provided by the correlated ToF spectrum, as shown in Figure 4.20 (c) for the Coulomb explosion of Allene (C_3H_4) molecules

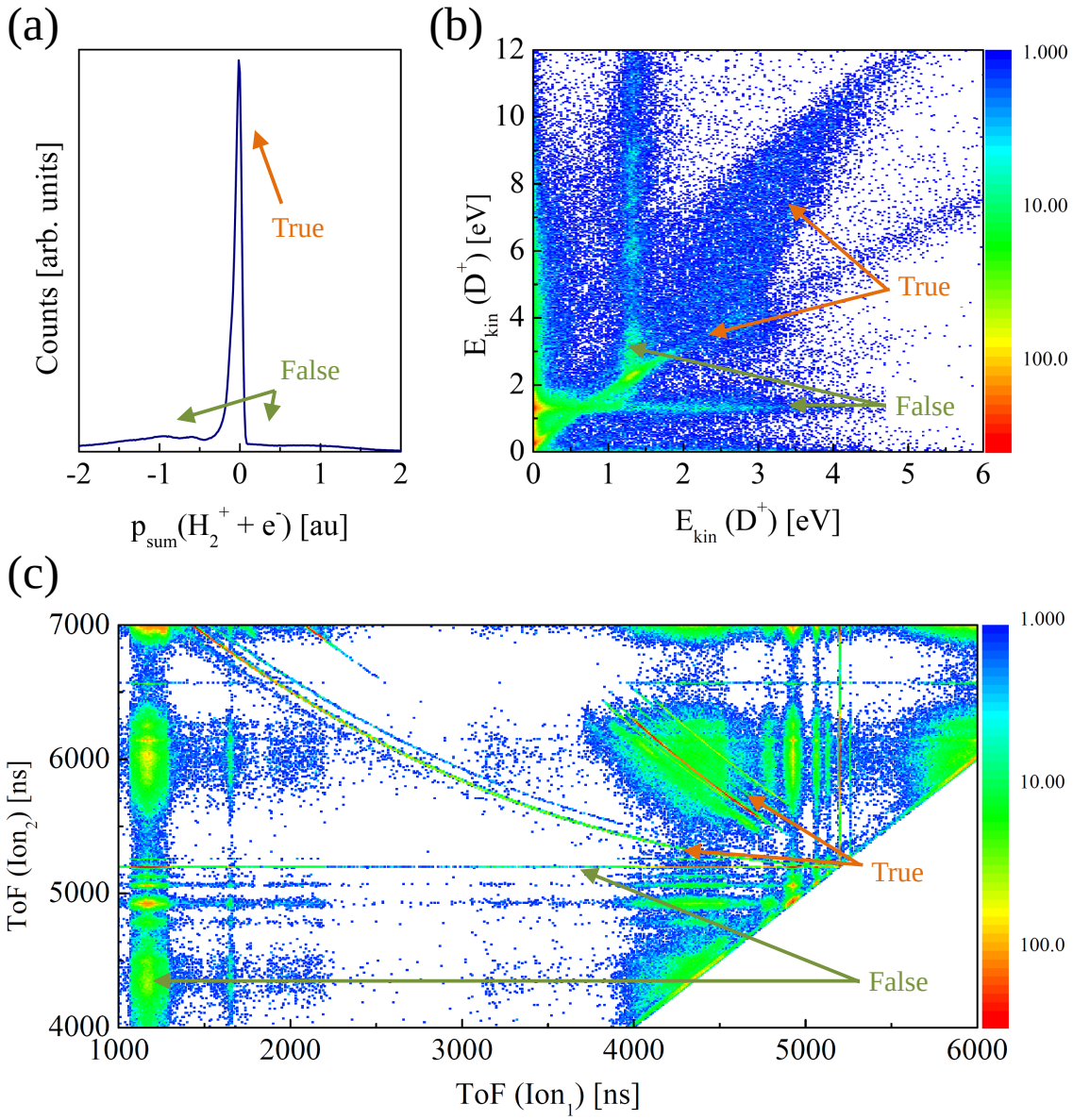

Figure 4.20: Representation of three different experiments tracing coincident events. True and false coincident are labeled with orange and green arrows, respectively. (a) represents the momentum sum of single photoionization of H_2 molecules. Coincident electrons and ions have the same momentum quantity but opposite directions. (b) Energy correlation diagram of a $D^+ + D^+$ Coulomb explosion in a two–color pump–probe measurement. Coincident events appear on diagonal lines. (c) Correlated ToF spectrum for ionization of Allene (C_3H_4) with strong laser pulses [Cör12]. Fragmentation channels with coincident particles are encountered on diagonal lines.

in two ionic fragments [Cör12]. Here, the two coincident ions share equal absolute values for the momentum and are thus distributed along characteristic curves. The diagram exhibits many of these curves due to the number of possible fragmentation channels and final ionic species. In summary, all presented diagrams allow the exclusion of false coincidences by the application of respective conditions and restrictions.

4.4.6 Molecular frame photoelectron angular distributions (MFPADs)

A further step in evaluating coincident measurements, in particular with respect to the fragmentation of molecules, is obtained by an inspection of angular distributions, which initially are represented in the laboratory frame of reference. The ReMi provides the

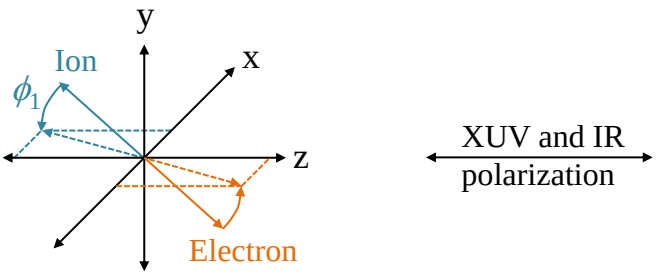

Figure 4.21: Molecular frame transitions for two counter–propagating ion–electron pairs. The particles are rotated onto the $x - z$ plane, thus containing the polarization axis.

possibility to transform the data event–by–event into more suitable coordinates, e.g. the so–called molecular frame. For fragmentation reactions in diatomic molecules, there are two options: The first and most simple method consists of defining a molecular axis by the detected ionic fragments and calculate the angle between the corresponding electron momentum vector and the molecular axis. This provides a one dimensional distribution as it resembles an integration over the symmetry axis of the molecule.

More information can be attained by including an additionally assigned direction, which in the case of laser induced ionization is for obvious reasons, the polarization axis. In the conducted experiments on molecules both polarization directions of the IR and XUV beam have been collinear with the spectrometer axis (z). Therefore, the polarization direction (z) and an arbitrary orthogonal direction, which in this case is chosen to be (x), define a plane into which all molecular fragments (ions and electrons) are rotated, as illustrated in Figure 4.21. The orientation of the molecular axis in the laboratory reference frame is imprinted and reconstructed by the propagation direction of the corresponding ion. This transformation leads to the so called molecular frame photoelectron angular distributions (MFPAD) [Luc+02; Laf+03]. As will be demonstrated in the discussion of the experimental results, these distributions indicate appearing partial electron waves and molecular symmetries.

5 Experimental results: Dissociative photoionization of molecular hydrogen

The experimental branch of atomic and molecular physics has benefited tremendously from the spectacular recent progress in laser technology, as well as from the development of advanced detection systems. Even more important, in this context, is the invention of new fundamental measuring principles which permit deeper insight into various physical processes. For example, the concept of pump–probe spectroscopy, introduced by Ahmed Zewail who was awarded with the Nobel Price in chemistry in 1999, triggered studies on fast chemical reaction kinematics and quantum control [Zew00]. In this method, atoms or molecules are exposed to two subsequent laser pulses with a variable time delay in between to induce and influence particular reactions, including excitations of electronic, vibrational or rotational states as well as molecular fragmentations such as dissociation or Coulomb explosion. The initialization is usually realized with a high–intensity (or high–photon energy) pulse, often referred to as pump–pulse. The second, so called probe–pulse, is used to interrupt, change or inspect the progress of the reaction at a well–defined time after the initialization. Given that the pulses used are shorter than the reaction of interest, it is possible to obtain a time–varying (step–by–step) response, thus revealing time–dependent reaction dynamics including, for instance, the occupation of intermediate states.

In few–femtosecond and attosecond laser spectroscopy, pump–probe measurements have been primarily applied to studies of Auger decays [Hen+01] and vibrational wave–packet dynamics in H_2 and D_2 molecules [Aln+05; Erg+06b; Kel+09; Jia+10]. In particular, measurements with H_2 as a molecular benchmark system often reveal fundamental processes which can be considered as general mechanisms that are also active in more complex molecules. A current example for this is the photon–induced inversion symmetry breaking in H_2 [Mar+07; SV+10].

Molecular hydrogen and its associated ion H_2^+ have been intensively studied theoretically for many years as their relatively few degrees of freedom make it ideal to develop faster and more precise calculations. For this reason, there exist extensive sets of calculated cross sections [YSD98], and potential energy surfaces [Sha70; SM97; SM99b], and new ideas for experimentally testing basic reactions using H_2 molecules are proposed continuously [HCS09].

The present work is dedicated to performing ultrafast pump–probe spectroscopy on small molecules by combining a state–of–the–art XUV laser system based on high–order

harmonic generation (HHG) and a reaction microscope (ReMi), as described in chapter 4. Here, the setup was used to study different reaction channels that lead to dissociative photoionization of molecular hydrogen. In order to explain these channels, it is useful to consider the potential energy curves (PES) of H_2, H_2^{**} and H_2^+ molecules that were introduced in chapter 3. In terms of a general overview, all relevant PES are presented within one term scheme (Figure 5.1).

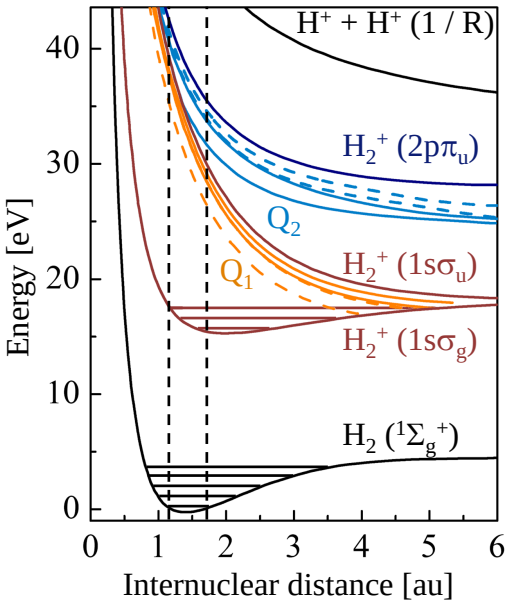

Figure 5.1: PES of the H_2 ground state (black), doubly–excited states H_2^{**} (orange for Q_1 and light blue for Q_2) and H_2^+ (red for $(1s\sigma_g)$, $(1s\sigma_u)$ and blue for $(2p\pi_u)$). Vibrational levels are indicated by horizontal lines in binding PES. The Franck–Condon region is represented by vertical dotted lines. All curves are adapted from [FM09].

Considering available XUV photon energies between 15 eV and 40 eV, as well as given cross sections [YSD98], Figure 5.1 reflects possible photon–induced transitions within the Franck–Condon region. The XUV photons therein access states in H_2^+, such as the bound $(1s\sigma_g)$ and the dissociative $(1s\sigma_u)$, $(2p\pi_u)$ and $(2s\sigma_g)$ as well as doubly–excited states H_2^{**} (Q_n).

The resulting reaction channels are quite numerous and only remain distinguishable if the correlation energy and angular distributions of the coincident particles are considered in the analysis. At this point, we take decisive advantage of the ReMi, that enables for the first time to inspect both of these quantities. Accordingly, the correlated energy and the photoelectron angular distributions will be used throughout the subsequent discussions, and will allow us to separate and investigate in unprecedented detail selected light–molecule interaction phenomena.

The results that have been obtained in this project are presented as follows: First, single ionization of hydrogen molecules and a related process, termed as ground–state dissociation, are discussed. In addition, measurements on the real–time imaging of ultrafast nuclear dynamics in the hydrogen molecular ion are presented. Electron–electron–correlations, doubly–excited states and asymmetry effects are analyzed in the second section. The third part will show results on XUV–pump IR–probe measurements on the population dynamics of doubly–excited states.

5.1 Nuclear wave–packet dynamics

Short XUV laser pulses are used to simultaneously and coherently excite multiple vibrational levels in the hydrogen molecular ion, as described in section 3.3. The superposition of the excited vibrational wave functions give rise to the formation of a nuclear wave packet which can be analyzed with a delayed IR pulse, provided that both pulse durations are short with respect to the vibrational dynamics. Its properties will be explored and presented in the following sections; however, it is appropriate to begin with discussing the single XUV–photon response of the H_2 molecule.

5.1.1 Ground–state dissociation

This section will present results of a process termed ground–state dissociation of H_2^+ via irradiation of hydrogen molecules with XUV pulses. The XUV–photon energy spectrum used in the experiment consists of several peaks, each with approximately 1 eV full width at half maximum (FWHM). They are separated by 3.45 eV and cover the range between 15 and 40 eV. In molecular hydrogen, there are two important energy barriers that must be considered:

- The ionization threshold $I_p = 15.46\,\text{eV}$.
- The dissociative ionization threshold $I_p + I_d = 18.08\,\text{eV}$.

Therefore, one of the HHG–XUV photons with $E_\gamma > 15.46\,\text{eV}$ provides enough energy to non–resonantly ionize H_2 molecules and populate the binding ground state ($1s\sigma_g$) of H_2^+. This particular state consists of 20 vibrational levels [BHP70], and most are populated in a one–photon transition. The reason for this is the difference between the equilibrium internuclear distances of the H_2 and H_2^+ ground states, as represented by the PES in Figure 5.1 and as described in section 3.2.3. As a consequence, the Franck–Condon factors provide non–vanishing contributions for all vibrational levels in H_2^+, even including the continuum. The properties of this instantaneous single–photon induced excitation of vibrational levels in H_2^+ will be discussed in detail in the section 5.1.2.

Previous experiments on the non–resonant ionization of H_2 with XUV photons showed that 98 % of the ionized molecules are bound and vibrationally excited in the $(1s\sigma_g)$ electronic ground state of H_2^+ [BF73]. The remaining 2 % are related to the population of vibrational continuum levels with energies above the dissociation threshold, consequently these ions fragmentize into the two particles: $H^+ + H$. This process is referred to as ground–state dissociation and it is observed in the conducted experiments with single XUV photons.

The ionization to the bound $(1s\sigma_g)$ and the dissociative ionization can be analyzed by the total kinetic energy of all charged fragments, as presented in Figure 5.2. The distribution

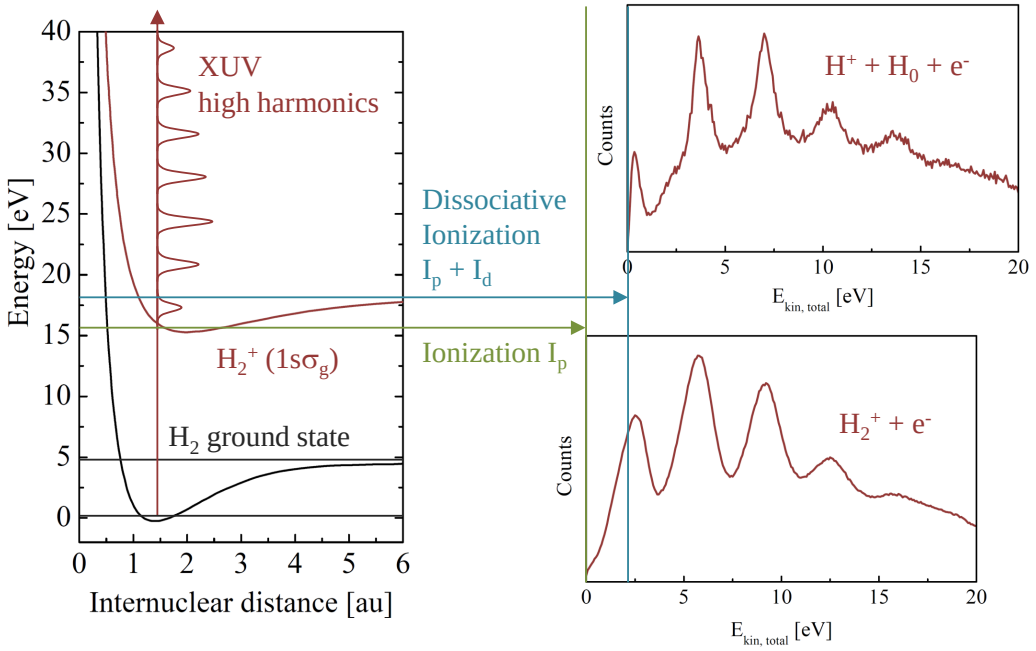

Figure 5.2: Left: The ground state of H_2 is ionized by an XUV pulse with photon energies spaced by 3.45 eV. Right: 98 % of the events lead to direct ionization into H_2^+, with the corresponding threshold, located at approximately 16.0 eV. 2 % of the parent molecules dissociate into $H + H^+ + e^-$ for photon energies above 18.1 eV. This process is termed ground–state dissociation.

of the energies among the charged and neutral constituents is further represented by the following equations:

$$E_{\text{kin, total}}^{\text{bound}} = E_{H_2^+} + E_{e^-} = E_\gamma - I_p = E_\gamma - 15.5\,eV \quad (5.1)$$

$$E_{\text{kin, total}}^{\text{dissociation}} = E_{H^+} + E_H + E_{e^-} = E_\gamma - (I_p + I_d) = E_\gamma - 18.1\,eV \quad (5.2)$$

Both processes reveal, through energy conservation, the typical spectral distribution of the high–harmonic radiation. When inspecting the total kinetic energy of all fragments, one

observes that in both cases, the electrons carry the largest portion of the energy. Still, the two presented energy spectra in Figure 5.2 feature two notable differences which shall be discussed subsequently. First, as the ionization to H_2^+ involves several vibrational levels, the total kinetic energy distribution of those events appears broadened in comparison to the dissociation as well as to ionization of atomic species. Without the precise knowledge of the XUV photon energies it is not possible to resolve the energies of the vibrational levels or provide information about the population density. However, as shown in section 5.1.2, the reconstruction of the vibrational levels can be realized in an XUV–pump IR–probe measurement. In such experiments it is possible to "look" into their distribution by using delayed IR pulses that project the bound molecules into the dissociative continuum. The exact procedure will be elucidated in section 5.1.2; nevertheless, it is appropriate to briefly preview the results on the identified and resolved vibrational levels in order to analyze the spectra in Figure 5.2 (right). Populated vibrational states range between $\nu = 6$ and $\nu = 16$ with the highest contribution at $\nu = 9$. Furthermore, they do not involve the vibrational ground state of H_2^+. A more precise analysis of the energy spectrum of the bound ionic molecules reveals that the lowest occupied state corresponds to $\nu = 2$. This leads to the conclusion that the total kinetic energy distribution of the H_2^+ events is downshifted and, accordingly, the value for $I_p = 15.5\,\mathrm{eV}$ must be corrected to $\sim 16.0\,\mathrm{eV}$.

A second difference, concerning the total kinetic energy spectra of H^+ and H_2^+, is related to the distribution of the incident photon energy between nuclear fragments and electrons. In the case of the H_2^+, $E^{\mathrm{bound}}_{\mathrm{kin,\,total}}$ is mainly given by the kinetic energy of the electrons, as the recoil ions, due to the higher mass, are only comprised of energies in the meV range. In contrast, the dissociation of H_2^+ into H^+ and H transfers up to 0.5 eV into the nuclear fragments.

5.1.2 Nuclear wave–packet dynamics in an XUV–pump IR–probe scheme

To date, XUV–attosecond pulse trains from high–harmonic sources have been used extensively in single–pulse experiments in order to probe the structure of diatomic and even larger molecules, thus resolving the position of the atomic constituents and gaining information on the electron molecular orbitals [Bak+06; Mec+08]. In order to observe the dynamics of excited wave packets, such as their dephasing in time, it is necessary to perform pump–probe measurements that involve two short pulses. Such measurements have been conducted in previous scientific works, using either intense ultrashort IR or XUV pulses in the first excitation step [Erg+06b] and [Kel+09], respectively. In this context, the application of single–XUV photons provides cleaner signals and simplifies the wave–packet characterization, as intensity effects of the pump IR beam do not complicate the interpretation.

In Figure 5.3 the real–time mapping of the nuclear wave packet is shown for three different time ranges spanning 1200 fs, 230 fs and 65 fs between the XUV and the IR pulse.

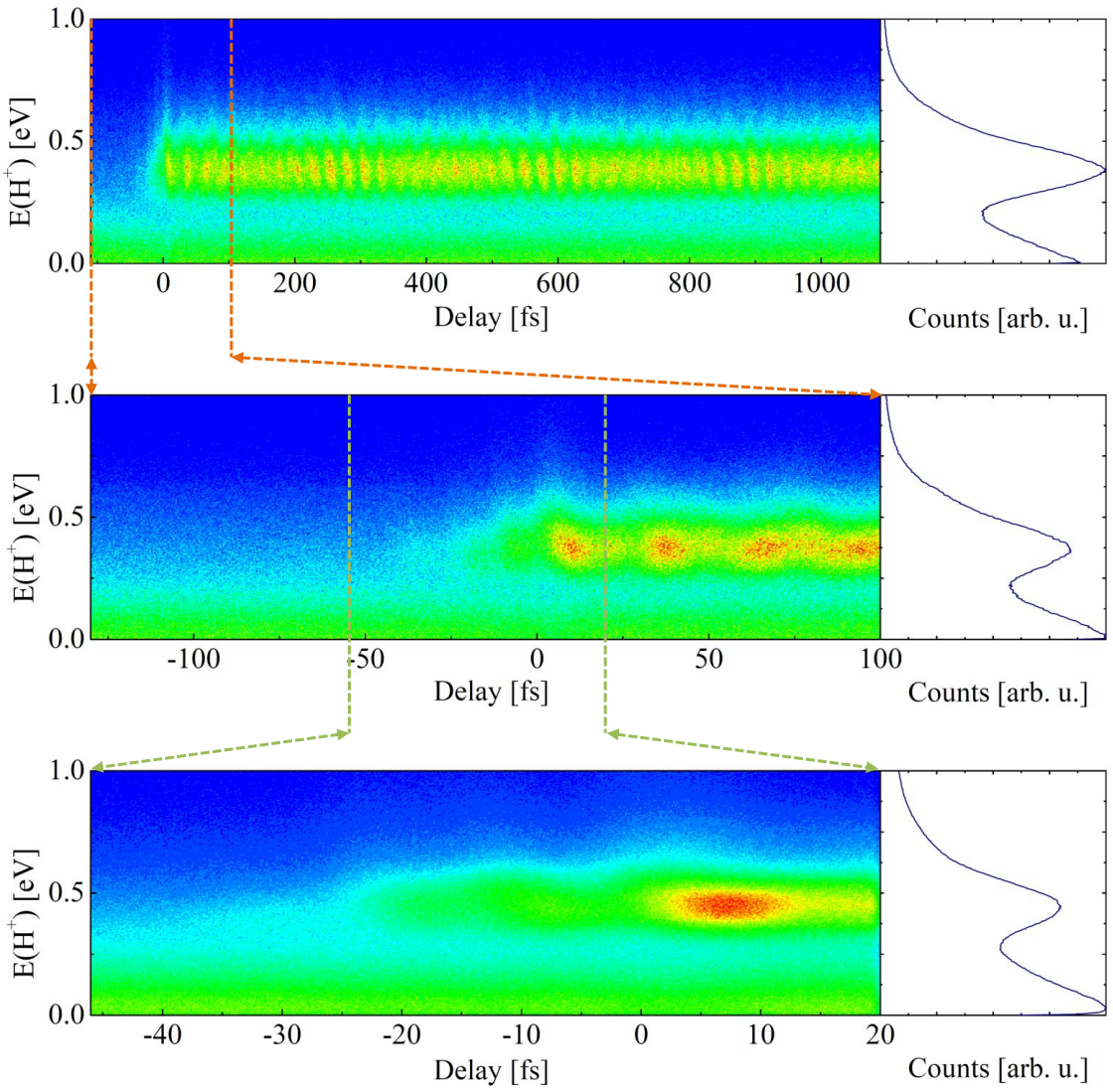

Figure 5.3: Kinetic energy $E(H^+)$ versus delay in an XUV–pump IR–probe experiment on H_2 molecules for three different delay ranges (1200 fs, 230 fs and 65 fs). The oscillating structure around 0.5 eV reveals the nuclear wave–packet dynamics of vibrationally excited H_2^+ ions. At delay–times where the H^+ yield is high, the wave–packet location is close to the potential boundary. At this internuclear distance the IR resonantly couples to the $(1s\sigma_u)$ repulsive PES.

The wave–packet dynamic is imprinted in the oscillation of the ionization yield as a function of the H^+ kinetic energy. Here, the conventional representation of a pump-probe scenario is applied, i. e. negative delays correspond to a situation where the IR pulse interacts with the target before the XUV pulse. In this case, the absolute time zero is determined from a previously measured IR–IR autocorrelation.

From the measurement with the extended delay range of 1200 fs, it is possible to extract two characteristic time scales: A short time T_{cl} of ~ 26 fs, and a long time T_{rev} of ~ 305 fs. In Table 5.1, these quantities are compared to the values that are obtained from the theoretical model and the simulation which are both described in section 3.3. Furthermore, the

	T_{cl}	T_{rev}
Experiment	26.1 fs ± 1 fs	305 fs ± 5 fs
Theoretical model	29.7 fs	596 fs
Simulation	27.0 fs	297 fs

Table 5.1: Comparison of the wave–packet oscillation period T_{cl} and the revival cycle T_{rev} between the measurement, the theoretical model and the simulation from section 3.3.

long–delay measurement contains information about the spectrum of vibrational spacings, as well as population amplitudes and relative phases [Feu+07].

As mentioned in the theoretical discussion in section 3.3, the simulation provides values for T_{cl} and T_{rev} which are consistent with those that were measured. The differences, in particular between the revival periods, can be ascribed to the neglect of beating signals between doubly spaced vibrational states which are actually observed in the experiment, as will be shown subsequently in the Fourier analysis of the delay–dependent spectra. Before proceeding with a detailed discussion, it is useful to explain the underlying process using the hydrogen molecular ion potential curves, illustrated in Figure 5.4.

The dynamics is initiated by the absorption of a photon from the XUV pulse, simultaneously exciting at least nine vibrational states in H_2^+ $(1s\sigma_g)$, ranging from $\nu = 6$ up to $\nu = 16$, with specific amplitudes and initially, identical phases. The corresponding wave functions overlap and form a vibrational wave packet which oscillates within the anharmonic potential of the $(1s\sigma_g)$ state. Here, the boundaries of the potential can be considered as turning points for the wave packet. As explained in section 3.3, the oscillation period of the wave packet – depicted as T_{cl} – is connected to the properties of the molecule, such as masses of the nuclei, the equilibrium position of the internuclear distance and, for larger molecules, structural parameters. Furthermore, T_{cl} depends on the activated vibrational energy levels and their energy spacings.

By means of a second, ultrashort IR pulse, the binding and antibinding states in H_2^+ can

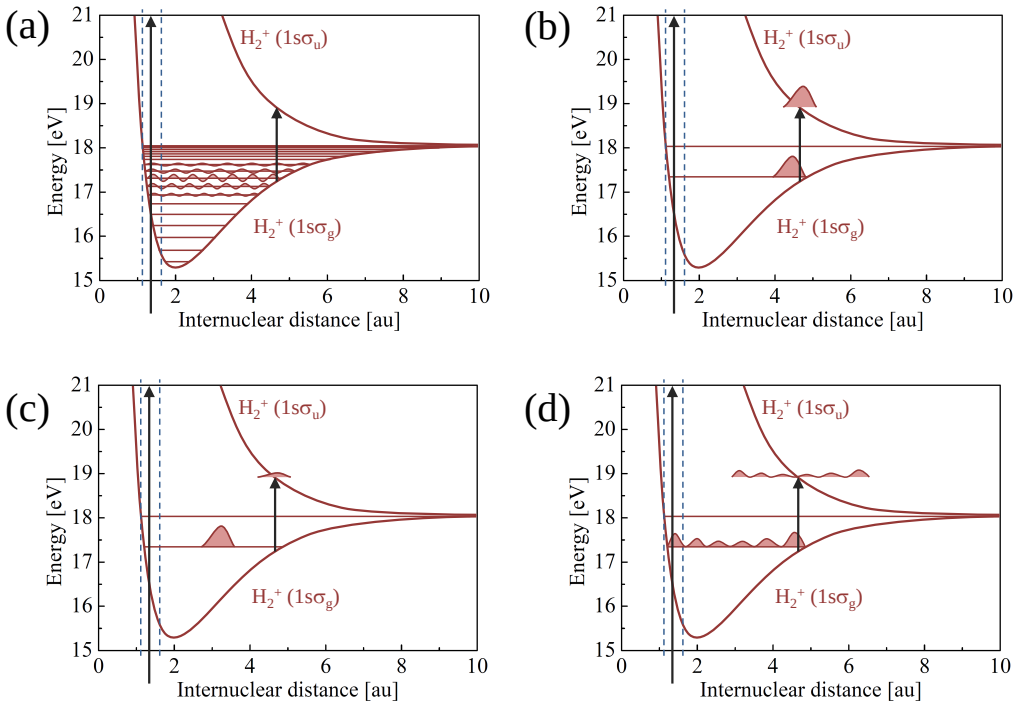

Figure 5.4: Representation of the IR–induced coupling between the $(1s\sigma_g)$ and $(1s\sigma_u)$ states. Figure (a) denotes the simultaneous excitation of several vibrational states in H_2^+, whereby a wave packet is generated. Depending on the localization of this wave packet (b) and (c) illustrate the different resulting dissociation yields. In (d) the dissociation signal of a dephased wave packet in the presence of an IR pulse is demonstrated.

be coupled[1], such that the system is projected onto the dissociating $(1s\sigma_u)$ PES [Kel+09]. This process is also referred to as bond softening [Buc+90; Sae04]. Note, a pulse duration shorter than T_{cl}, implies that the wave packet can propagate freely in the potential before being influenced by the laser. As the nuclear wave packet oscillates between the borders of the potential well, it becomes apparent that the yield of dissociation into $H^+\,(E_{\mathrm{kin}} \sim 0.5\,\mathrm{eV}) + H\,(E_{\mathrm{kin}} \sim 0.5\,\mathrm{eV})$ is dependent on the location of the wave packet. The measurement exhibits a first maximum of the dissociation yields at a delay time of approximately 6 fs between the XUV and IR pulses. This corresponds to the time the wave packet needs to move from the Franck–Condon region to the outer turning point of the potential.

If the $(1s\sigma_g)$ curve would correspond to a harmonic potential, where the levels are equidistant in energy, the vibrational wave packet would feature a constant temporal profile, only determined by the initial excitation. The delay–dependent measurement of the

[1] The laser induced coupling of the binding and antibinding H_2^+ states can be described within the Floquet model. The interested reader is referred to [Shi65; GS+95].

H^+ events would thus lead to a continuous, sinusoidal signal. In H_2^+, the $(1s\sigma_g)$ potential curve is anharmonic which implies that the energy spacing between neighboring vibrational levels decreases with increasing level number ν. This results in a more complex and time–varying form of the total phase of the wave packet. As a consequence, the temporal profile of the wave packet becomes broadened in space and, accordingly, the oscillation in the dissociation yield smears out; however, individual vibrational state contributions of the wave packet return into phase which occurs after the second characteristic time T_{rev}. Within this revival cycle, the wave packet is understood to undergo a de- and rephasing process. In Figure 5.4 the signal dependence of the dissociation yield from the localization of the wave packet, and correspondingly the time delay between the IR and XUV pulse, is illustrated.

Such revival properties have been observed experimentally in [Erg+06b] and [Kel+09] in D_2^+ and H_2^+ molecules and explained theoretically in [Feu+07; FT03; HT10; LTM06]. In [Erg+06a; TNF08] this experimental procedure is expanded to a Coulomb explosion imaging (CEI) technique on deuterium molecules. There, the second pulse is applied with a much higher intensity, reaching the second ionization threshold and, thus, projecting the D_2^+ on the $D^+ + D^+$ repulsive curve. This technique has been further applied to deuterium molecules in a comparably small delay range of 5 fs in the temporal overlap region of the two pulses, suggesting an interference effect between ionization pathways that involve different harmonic orders as well as the laser–induced coupling of the $(1s\sigma_g)$ and $(1s\sigma_u)$ states [Kel+11]. This process is closely related to typical two–color experiments on rare–gas atoms with XUV attosecond pulse trains, which are often referred to as sideband oscillations and are used for a temporal characterization of the XUV pulses.

5.1.3 Fourier analysis of the nuclear wave–packet dynamics

Following the discussion of the general properties of the internuclear motion, a Fourier analysis of the time–dependent spectra provides further insight into the contributing vibrational levels and their coupling. In Figure 5.5, the results are shown, revealing energy or frequency ($E = \hbar\omega$) components between 0.052 and 0.298 eV. These features do not correspond directly to energies of different levels; instead they represent the beating of two, mostly adjacent vibrational states. As the spacing between two of these states differ due to the anharmonicity of the potential, it is possible to deduce the number of beating states from the frequency of visible peaks. Here, the series of peaks in the Fourier spectrum can be related to the beating of states between the $\nu = (15, 16)$ and $\nu = (7, 9)$ vibrational levels in H_2^+. Altogether, at least twelve peaks are clearly identified and the measured frequencies suggest beating levels from $\nu = 6$ to $\nu = 16$, denoted by brackets in Figure 5.5 (a). These values are in agreement with observations made by [Kel+09] and the calculated vibrational energies of the hydrogen molecular ion in [BHP70].

Furthermore, it is necessary to investigate the KER dependencies of the frequency com-

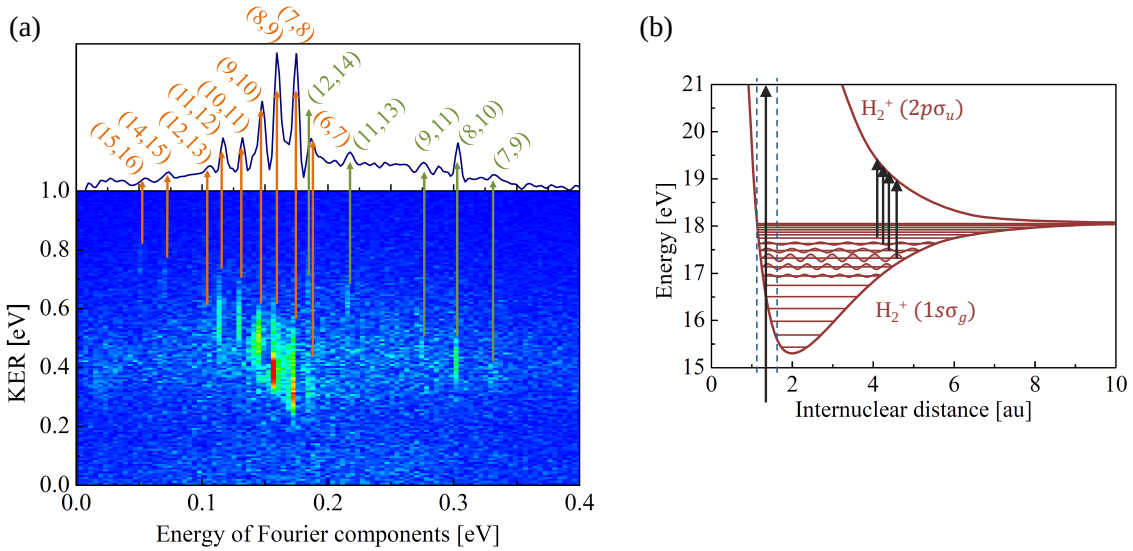

Figure 5.5: (a) Representation of a Fourier analysis, extracted from the $E(H^+)$ vs. delay spectrum of Figure 5.3, and the associated projection, where all identified level pairs are labeled. Here, the vibrational states of the H_2^+ ion that are involved in the wave–packet dynamics, can be identified. The amplitude provides information about the intensity of the interaction and the initial population of the respective states. Between $\sim 0.1 - 0.2\,eV$, the frequency components correspond to adjacent vibrational levels $\Delta\nu = 1$. Higher frequencies can be related to doubly spaced levels which means that $\Delta\nu = 2$. (b) The coupling of different vibrational levels to the dissociative PES leads to different kinetic energies of the dissociation products.

ponents, as they reflect the relation between ionization probability and internuclear distance, R. From both diagrams in Figure 5.5 it can be deduced that the beating signals of lower–lying, adjacent vibrational levels lead to lower kinetic energies of the nuclear fragments and vice versa. This can be understood by considering the IR coupling to the dissociative potential curve ($1s\sigma_u$) and including the vibrational states, as well as the values of the internuclear distance, at which this coupling is possible. As it is illustrated in Figure 5.5 (b) by the arrows, the dissociative ($1s\sigma_u$) curve is in resonance and, thus, is populated at smaller R for increasing ν resulting in increasing KERs. In addition, the transition can occur at shorter and longer IR delays as compared to lower ν being in resonance essentially at the turning point. The arrows, denoting fixed IR photon energies thus demonstrate the generation of hydrogen ions with different kinetic energies.

Another important quantity in the measurement and interpretation of the wave–packet dynamics is the spectral width (FWHM) of the IR photons which amounts up to $\pm 0.15\,\mathrm{eV}$ and is distributed around the center energy of $1.67\,\mathrm{eV}$, ($\lambda_c = 744\,\mathrm{nm}$). The energy spacing between the vibrational states which surround the strongest contributing level, $\nu = 9$, is slightly smaller than the spectral width of the IR field. This leads to the conclusion that

beating signals of $\Delta\nu = 3$ spaced vibrational levels are not expected to be measured, whereas $\Delta\nu = 2$ "beatings" are accessible. In particular for higher vibrational states a small contribution of $\Delta\nu = 2$ is observed in the experiment, as shown in Figure 5.5 (a) (green labeled beating signals).

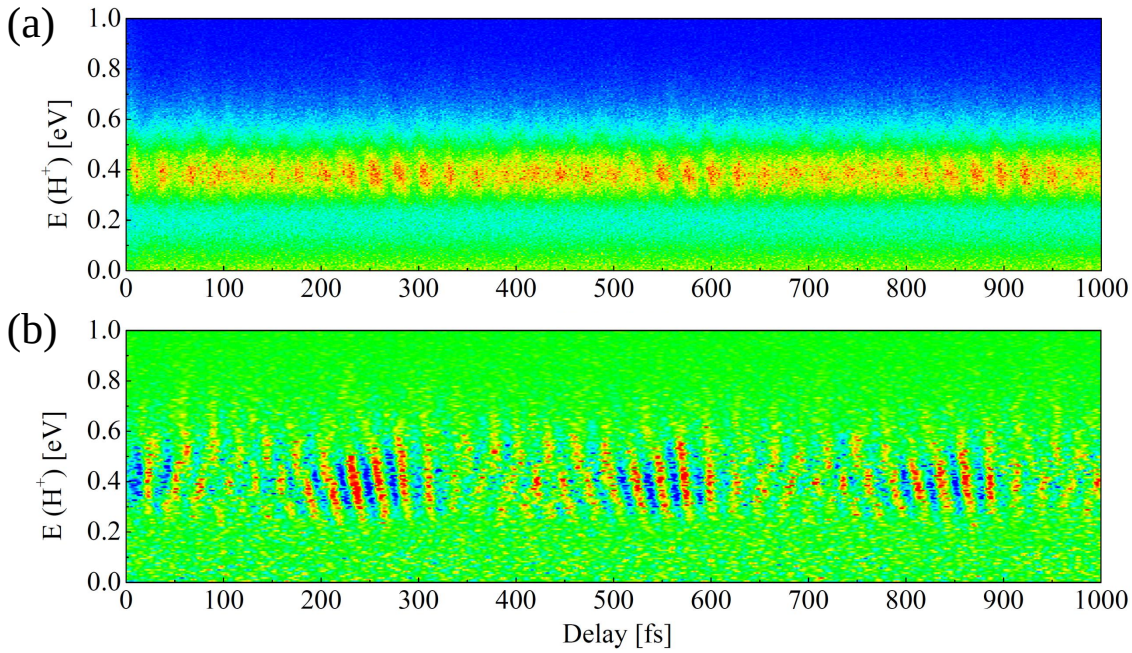

Figure 5.6: Analysis of the nuclear wave–packet dynamics in a delay range of 1000 fs. All figures represent the kinetic energy of the H^+ versus delay. (a) corresponds to the direct measurement, for (b), a broad Fourier filter, including all visible frequency components, is applied. For these frequency components, different revival times pertain.

In order to obtain even more detailed information on the wave–packet dynamics it is advantageous to select the measured frequency components in Figure 5.5 (a), i.e. discard all the background in the frequency spectrum and apply a second Fourier transformation into the temporal domain. This method allows for a significant reduction of the background signal and results in the visualization of sub–revival structures, as shown in Figure 5.6 (b). These sub–revivals are manifested in an inversely–phased structure, positioned at approximately 100 fs, 400 fs and 700 fs. Apart from the inverse phase, these structures are also separated in the kinetic energy of the ions at approximately 0.45 eV, suggesting that the beating frequency components split into two parts. After a half revival period T_{rev}, the two contributions return into phase. The comparison to earlier measurements, such as the one–color IR–IR experiments in [Erg+06c; Erg+06a] shows that fewer vibrational states are involved in this process and therefore lead to a cleaner overall signal.

In conclusion, the wave–packet dynamics has been observed with unprecedented clarity,

suggesting that the applied pulses feature durations in the range of 10 fs. Still, there are indications that the IR pulses include low–intensity sub–pulses which smear out the signal slightly. This can be verified in the middle and lower panel in Figures 5.3 in the overlap region around $\tau_{\text{delay}} = 0$, where the wave–packet signal is visible for negative delays, that is, when the IR pulse arrives first at the molecule. In particular, the short delay scan of 65 fs reveals details and allows the assumption that there are two pre–pulses which are separated by the main pulse by approximately 12 fs and 24 fs, respectively.

5.2 XUV–photon transitions to doubly–excited states

The IR–probing of wave–packet dynamics in H_2^+ is a fascinating method to observe fast vibrational motions in molecules. However, in comparison to the H_2^+ molecule, the neutral "parent" H_2 is in several aspects more interesting to study, especially concerning the correlation of the two electrons. For instance, in the case of H_2, this correlation manifests itself in the existence of doubly–excited states (see section 3.1.5), where both electrons are simultaneously excited during a single–photon absorption event, even though the corresponding photon energy is sufficient to ionize the molecule. These states play a significant role in processes like single- and multi-photon absorption, as well as in electron–impact excitation and electron scattering [SM99b]. Such phenomena are extremely difficult to describe by theory, as the involvement of many different particles including the two nuclei, as well as their mutual interaction leads to a high complexity. In molecular hydrogen, this is particularly crucial, due to the fact that the nuclear dynamics happens on a similar time–scale as the electron correlation[2]. Therefore, potential simplifications, such as the reduction of relevant states (close–coupling–calculations) or of degrees of freedom (one- or two–dimensional treatment), must be chosen carefully. The first described attempt to theoretically treat doubly–excited states in molecular hydrogen was performed by [BD74]; nevertheless, the most reliable data for these resonances were probably calculated by Martín et. al. These calculations have made important contributions to the doubly excited Rydberg series of Q_1 [SM97], Q_2 [SM99b] as well as to Q_3 and Q_4 in [FM01]. The general, computational treatment is based on the Feshbach theory [Fes62] and involves L^2 B–spline integrable functions as a basis set for molecular continuum states, as well as for all resonant states [Mar99].

These theoretical advancements had been necessary to explain the photon–induced dissociation of hydrogen molecules first studied at synchrotrons [BF73; Lat+93] and in experiments with duoplasmatron light [Chu+93]; currently, they have become relevant with respect to coherent XUV–light sources, such as free electron lasers (FELs) and higher harmonics [San+10]. To date, most experiments addressing doubly–excited states of H_2 focus

[2] The molecular vibration is in the order of 10 fs (for small ν), whereas the autoionization decay–times cover a range between 2 fs and $\sim$ 100 fs, dependent on the internuclear distance and symmetry of the state.

on the autoionization properties[3] [Gar+06; Lat+95; IHU96], as well as on the angular distributions of emitted fragments [Luc+02; Laf+03].

An interesting phenomenon that arises from the population of different doubly–excited states Q_n, is the appearance of asymmetry effects, thus far being studied primarily theoretically [PT+09]. These asymmetries are attributed to different dissociation paths which lead to the same final state and, therefore, give rise to interference. Especially in a simple, prototype molecular system, such as H_2, this symmetry breaking can be studied on a very fundamental level, allowing predictions for more complex systems.

5.2.1 Identification of doubly–excited states via the ion–electron energy–correlation spectrum

The PES in Figure 5.7 represents the states of H_2^+ and H_2^{**} that are relevant for single–XUV photon absorption. All states of the H_2^+ molecule, with the exception of the $(1s\sigma_g)$ level, are repulsive and lead, apart from the emitted electrons, to ions and neutral atoms. For doubly–excited states this is equally valid, provided that autoionization occurs during the dissociation of the molecule. The detection of coincident ion–electron pairs with the ReMi thus allows the reconstruction of the originating state by considering the energy distribution of the particles and the energy range of the PES within the Franck–Condon region.

Here, this idea is implemented by means of the energy–correlation diagram between the electron, the ion and the neutral (virtually reconstructed) atom, evaluated separately for each individual event, as shown in Figure 5.8. The spectrum provides the best access to the characteristics of doubly excited and directly dissociating H_2^+ states. The vertical axis represents the sum kinetic energies of ions and atoms, usually termed as KER (kinetic energy release) and the horizontal axis corresponds to the electron energy. Important features of the correlation diagram are the faint diagonal lines which correspond to different energies of absorbed high–harmonic photons, minus the dissociation threshold of 18.1 eV. Coincident events appear along these lines, as the photon energy is distributed among electron, ion and atom. Accordingly, it is possible to identify false coincidences outside of these areas resulting from rest–gas ionization, scattered electrons and the mixing of two coincident but independent dissociation events of different hydrogen molecules. Projecting along the coincidence lines provides the total kinetic energy of all fragments and, in addition, offers a tool to apply testing–conditions in order to select specific final states.

Certain energy regions in the correlation diagram are related to processes which are only accessible by the population of explicit states. Therefore, the spectrum can be considered as a coincidence map of all possible dissociation channels in molecular hydrogen. In order to illustrate this, the spectrum in Figure 5.8 is taken from an XUV–pump IR–probe measurement in H_2, even though the topic in this section pertains only to single XUV–photon

[3] Autoionization probabilities, lifetimes and final states.

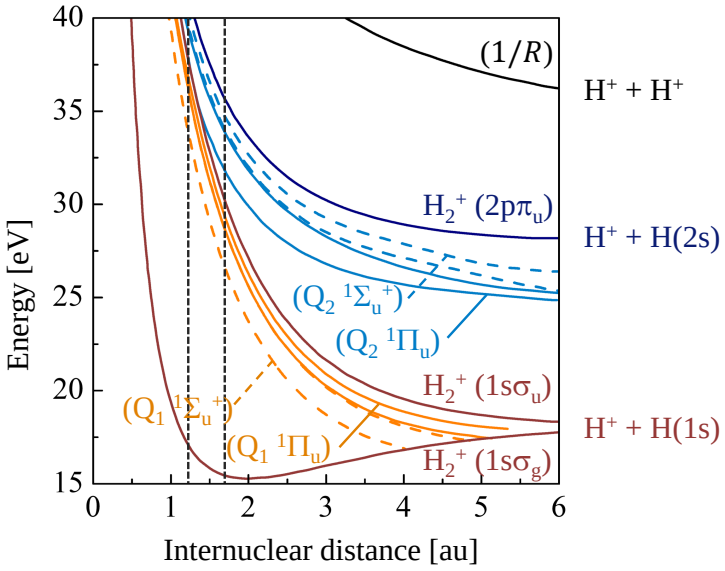

Figure 5.7: Representation of the lowest hydrogen molecular ion states $(1s\sigma_g)$, $(1s\sigma_u)$ and $(2p\pi_u)$, as well as the lowest dipole–allowed doubly excited Rydberg series Q_1 (orange) and Q_2 (light blue). The corresponding symmetries of the Q_n states are represented by full lines for $(^1\Pi_u)$ and dashed lines for $(^1\Sigma_u^+)$. The Franck–Condon region which characterizes the energy range of a possible excitation, is marked with black, dashed lines.

absorption. Here, the area at low KERs, for example, represents the ground–state dissociation $(0-0.8\,\text{eV})$ and the wave–packet dynamics $(0.5-2\,\text{eV})$, studied in the previous two sections.

The afore–mentioned coincidence lines correspond to the population of doubly–excited states Q_1 and Q_2 which are the only Rydberg series accessible with the available photon energies. As these states autoionize with a lifetime of a few femtoseconds, it is possible to observe KERs and electron energies ranging between 0 and 22 eV. Fast autoionizing processes are thus connected to lower KERs, whereas delayed autioionization is related to high KERs. Furthermore, it is possible to excite the Q_n states which dissociate into neutral fragments; however, they cannot be measured with the applied detection technique. In the high ionic kinetic energy region $(\text{KER} = 10-15\,\text{eV})$, an increase of $H^+ + H$ events is observed. This can be attributed to the direct ionization onto the $(1s\sigma_u)$ potential energy surface. Note that this particular state can be populated non–resonantly in all molecular orientations, whereas the doubly–excited states (with specific symmetries) are only promoted by the correct photon energy and the right orientation, with respect to laser polarization.

More information regarding the identification of relevant states is obtained by analyzing the energy–correlation spectrum for different geometrical configurations between the

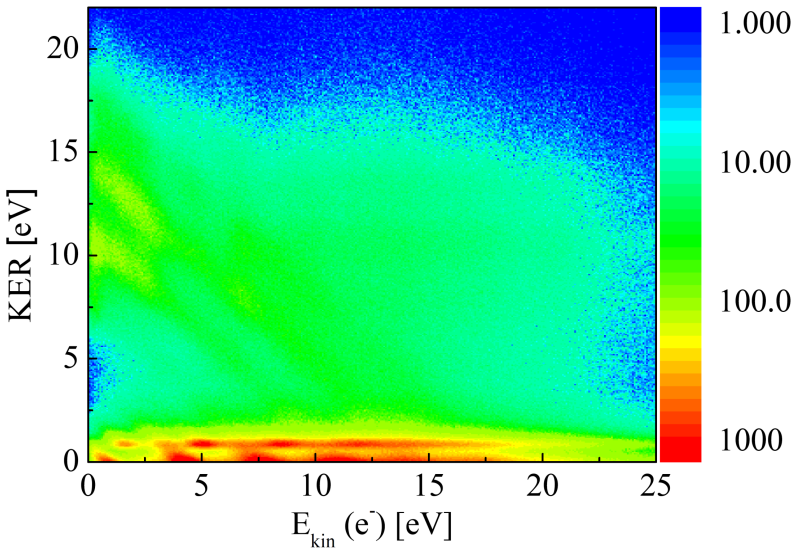

Figure 5.8: Correlated energy diagram in a logarithmic color scale. The lower KER area ($\lesssim 2\,\mathrm{eV}$) corresponds to the ground–state dissociation and the wave–packet dynamic discussed in the previous sections. The faint diagonal lines show the events which result from the doubly–excited states. The earlier it comes to an autoionization the more these events range into the low–KER region. The high–KER events are further enhanced by direct ionization via the $(1s\sigma_u)$ state.

molecule and the laser polarization axis. This method enables us to gain insight into the autoionization properties and symmetries of the doubly–excited states and provides access to angular distributions of the electrons in the molecular frame which can be considered as an unambiguous fingerprint of the originating states, as shown in the next section.

5.2.2 Identification of doubly–excited states via photoelectron angular distributions in the molecular frame (MFPAD)

Quantum mechanically, a photon–induced molecular transition must fulfill symmetry–based selection rules, as described in section 3.2.1. This fact leads to two conclusions: First, in bound–bound transitions[4] the symmetries of the initial state and the dipole operator determine the symmetry of the final state. Second, in ionization and autoionization, the concept of symmetry allows us to predict the composition of partial waves of emitted electrons and to deduce the resulting electron angular distributions. For the experiments on the dissociative photoionization of H_2, the electron angular distributions enable a more precise analysis of the dissociation channels that are identified in the energy coincidence map (Figure 5.8).

[4]Here, the relevant bound–bound transition corresponds to: $H_2 \xrightarrow{\mathrm{XUV}} H_2^{**}$.

In order to extract clear angular distributions, it is necessary to classify the transitions into two geometrical configurations regarding relative orientation between the molecular and the light–polarization axis. These are the parallel and the perpendicular transitions, where the difference in the symmetry refers to the dipole operator (Σ_u^+ for parallel and Π_u for perpendicular transitions) and the final state. In the presented analysis, the classification is realized by the determination of the molecular frame of reference for each measured event (the corresponding method is described in section 4.4.6). The resulting electron angular distributions are therefore referred to as MFPADs (molecular frame photoelectron angular distributions).

Angular distributions in parallel transitions

In parallel transitions $P_\parallel$, the photon polarization and the molecular axis are collinear. Events that fulfill this criterion can be selected by means of the axial–recoil approximation [Laf+03] which claims that the hydrogen molecular axis during photon absorption is close to the emission direction of the ion. A small discrepancy between both directions is given by the recoil energy of the emitted electron which is transferred to the molecular ion; however, the difference of approximately 1 meV is negligible in comparison to the dissociation energy of several eV. The deviation of the momentum vector direction is small as well; nevertheless, for an electron with a large momentum component perpendicular to the molecular axis, and small ionic energies, the angle correction can amount up to 7°.

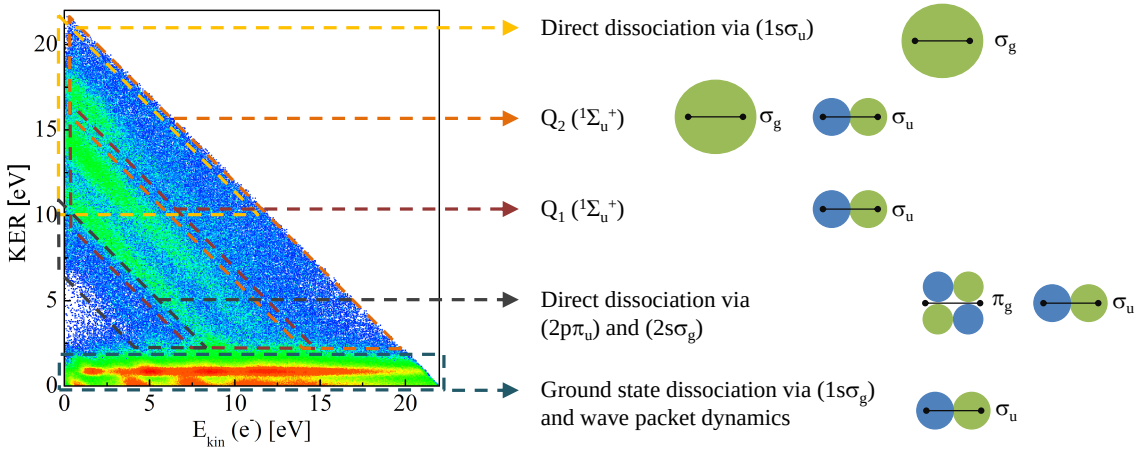

Figure 5.9: Parallel transitions: energy–correlation diagram. The dashed frames represent the energy sections, within which certain processes are expected to occur, such as ground–state and direct dissociation via $(1s\sigma_g)$ and $(1s\sigma_u)$, respectively. Moreover, the events which correspond to the autoionization of doubly excited $Q_{1,2}$ states are shown. The right panel illustrates the correlated electron partial waves, σ_g and σ_u. In the lower energy region, the green marked area denotes transitions to the $H_2^+(2p\pi_u)$ and $(2s\sigma_g)$ states.

In this work, the parallel transitions are defined by an angle smaller than 18° between the ion emission direction and the polarization axis (z). If this selection criterion is applied to the energy–correlation diagram of Figure 5.8, the high–harmonic lines within the doubly excited state section exhibit a very clean shape. The strongest structures correspond to the 17th, 19th and 21st harmonic photon energies.

Within the frame of parallel transitions, it is possible to assign certain areas in the energy–correlation spectrum to specific dissociation processes, those that involve either doubly–excited states, or those that proceed directly via ionization to the $H_2^+(1s\sigma_u)$ state. Here, five areas are marked in the limits of the Franck–Condon region, including ground–state dissociation via $(1s\sigma_g)$ and direct dissociation via $(1s\sigma_u)$, as well as excitation with subsequent autoionization of the lowest dipole–allowed $Q_{1,2}$ states. All of these processes are connected with the emission of electrons which, in the molecular frame of reference, exhibit specific partial waves, see section 3.2.1. In parallel transitions, mostly angular distributions, which are connected to σ_g and σ_u partial waves are expected to be measured. Hence, it is possible to identify most of these processes in the energy map 5.9:

$$\begin{aligned}
H_2 &\xrightarrow{\text{XUV}} H_2^+(1s\sigma_g) + e^- && \Rightarrow \quad \Lambda(e^-) = \sigma_u \\
H_2 &\xrightarrow{\text{XUV}} H_2^+(1s\sigma_u) + e^- && \Rightarrow \quad \Lambda(e^-) = \sigma_g \\
H_2 &\xrightarrow{\text{XUV}} H_2^{**}(Q_n) \xrightarrow{\text{autoionization}} H_2^+(1s\sigma_g) + e^- && \Rightarrow \quad \Lambda(e^-) = \sigma_u \\
H_2 &\xrightarrow{\text{XUV}} H_2^{**}(Q_n) \xrightarrow{\text{autoionization}} H_2^+(1s\sigma_u) + e^- && \Rightarrow \quad \Lambda(e^-) = \sigma_g
\end{aligned} \tag{5.3}$$

Here, $\Lambda(e^-)$ denotes the symmetry of the wave function of the emitted, free electron. This wave function is represented by partial waves, shown for all possible transitions on the right hand side of Figure 5.9. Note, blue and green areas correspond to parts of the wave function with opposite sign. All relevant partial waves and the resulting angular distributions are presented in section 3.2.2.

With photon energies between $\sim 36-43\,\text{eV}$, which are easily achievable with the present experimental setup, it is also possible to directly ionize the hydrogen molecules via the repulsive $(2p\pi_u)$[5] and $(2s\sigma_g)$ states of H_2^+:

$$\begin{aligned}
H_2 &\xrightarrow{\text{XUV}} H_2^+(2p\pi_u) + e^- && \Rightarrow \quad \Lambda(e^-) = \pi_g \\
H_2 &\xrightarrow{\text{XUV}} H_2^+(2s\sigma_g) + e^- && \Rightarrow \quad \Lambda(e^-) = \sigma_u
\end{aligned} \tag{5.4}$$

As the presented PES do not contain the $(2s\sigma_g)$ level, it must be noted that energetically the corresponding curve is positioned approximately 1.5 eV above the $(2p\pi_u)$ PES within the Franck–Condon region. Both states are dissociative and lead to an excited hydrogen

[5] The $(2p\pi_u)$ potential curve actually features a minimum at a internuclear distance of 4.2 au [Sha70]; however, the kinetic energy of the nuclear fragments is too high, to lead to a stable molecular ion.

atom ($H^*(n = 2)$), for which reason the final kinetic energy of the dissociation products is lowered. The energetically higher ($2s\sigma_g$) state, with Σ_g^+ symmetry, provides electron partial waves with σ_u symmetry, similar to those which result from the ($1s\sigma_g$) state. A completely different partial–wave symmetry, in comparison to all other channels corresponding to parallel transitions, is obtained by the dissociative ionization via ($2p\pi_u$), leading to a π_g symmetry.

These results are summarized in Figure 5.10 and represent the three–dimensional MFPADs shown as three two–dimensional subspace spectra (x,y), (x,z) and (y,z). Here, the molecular and the polarization axis are both oriented along the z–direction. It must be mentioned that the MFPADs exhibit an asymmetric distribution along the z–axis which can be attributed to an asymmetric detection efficiency in the ReMi.

In the first row of Figure 5.10, a typical σ_u partial wave is shown for the low–KER region which corresponds to the ground–state dissociation. Note, at slightly higher KER values ($0.8 - 2\,\text{eV}$) the same result for the emitted electrons is obtained. In this energy range, the KER is attributed to the additional absorption of an IR photon; however, the properties of the electron emission only depends on the initial step, the XUV–photon induced ionization to the ($1s\sigma_g$) state.

The second row represents the angular distribution for the region, where mostly direct dissociation via ($1s\sigma_u$) is expected. As one can see from Figure 5.9, this particular section also includes contributions of fast autoionizing doubly excited Q_1 and Q_2 states to the ($1s\sigma_g$) level. As a result, this energy section features a mixed structure of partial waves consisting of a σ_g and σ_u symmetry. Therefore, the MFPAD resembles a circular distribution which is slightly elongated along the z–axis.

In the last row in Figure 5.10, results are presented for events that can be related to the dissociative ionization via the ($2p\pi_u$) and ($2s\sigma_g$) potential curves. As can be verified from the two equations (5.4), the angular distributions are given by a combination between σ_u and π_g partial waves. In other words, this corresponds to the overlap of a club and butterfly shape which finally leads to a butterfly structure, bent towards the z–axis. In fact, this particular pattern is measured and especially visible in the orange distribution, where a slice in the (x,y) plane is selected. Otherwise, the distribution is smeared out (blue distribution) because in parallel transitions, all angular distributions are invariant with respect to rotations around the molecular axis (z).

The photon energies which are necessary to populate the ($2p\pi_u$) state within the Franck–Condon region, correspond to the 21st and the 23rd harmonic (36.2, 39.6 eV) and, for the ($2s\sigma_g$) state, this range is approximately one harmonic energy higher, thus connected to the 23rd and 25th harmonic (39.6, 43.1 eV). Both states provide, within the energy resolution of the experiment, the same dissociation limit which in comparison to all other relevant states in H_2^+, is lifted by the first excitation energy of the hydrogen atom. In other words, since the dissociation products of ($2p\pi_u$) and ($2s\sigma_g$) are identified as $H^+ + H(n = 2)$, the kinetic energy release is reduced by $13.6 \cdot 3/4\,\text{eV} = 10.2\,\text{eV}$, thus shifting associated events

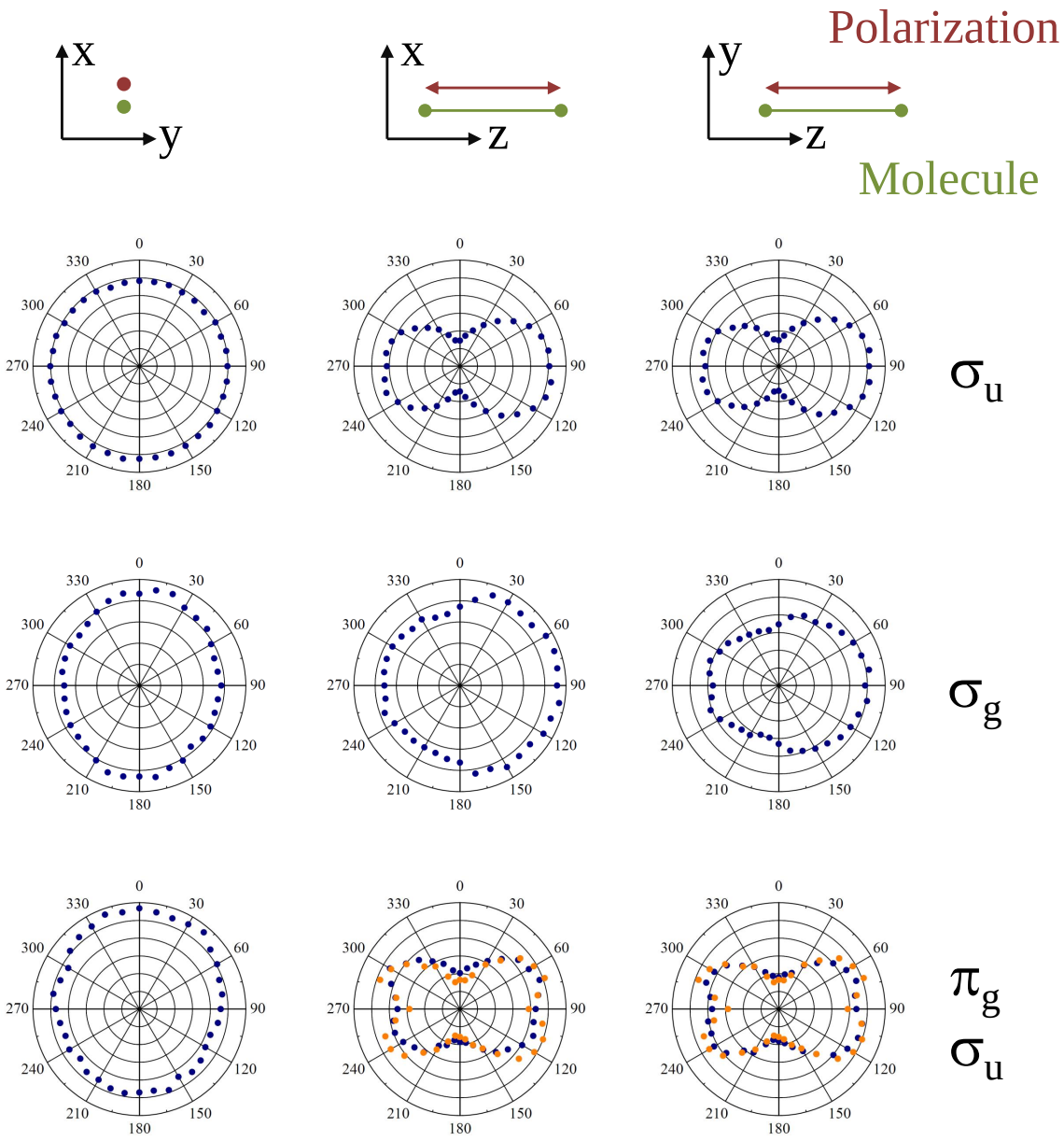

Figure 5.10: Electron angular distributions in parallel transitions for three different sections of the energy–correlation diagram. Row 1: MFPADs for an electron σ_u partial wave for ionization to the $(1s\sigma_g)$ state. Row 2: MFPADs for an electron σ_g partial wave for ionization to the $(1s\sigma_u)$ state. Row 3: MFPADs for electron π_g and σ_u partial waves for ionization to the $(2p\pi_u)$ and $(2s\sigma_g)$ states, respectively. The π_g contribution can be enhanced by selecting slices in the (x, y) momentum plane (orange data points).

to lower values in the energy–correlation diagram. Interestingly, this energy difference only varies by 0.15 eV from the triple spacing of the higher harmonics ($3 \cdot 3.45\,\text{eV} = 10.35\,\text{eV}$). For this reason, events arising from the repulsion via the $(2p\pi_u)$ and $(2s\sigma_g)$ states will likely appear on top of the lower–energetic diagonal lines in the energy spectrum.

Angular distributions in perpendicular transitions

Perpendicular transitions are characterized by a 90° relative orientation between the polarization direction and the molecule, such that the internuclear axis is inside the (x,y) plane[6] with an opening angle of $\pm 23°$. In this configuration, the transition to the molecular frame and the corresponding MFPADs are particularly powerful as there now exist two assigned directions, given by the polarization axis (z) and the molecular axis (x). As a consequence, the angular distributions in the (x,y), (x,z) and (y,z) planes directly correspond to three projections of the electron partial waves, without requiring any further conditions, such as in the case of parallel transitions (see last row in Figure 5.10).

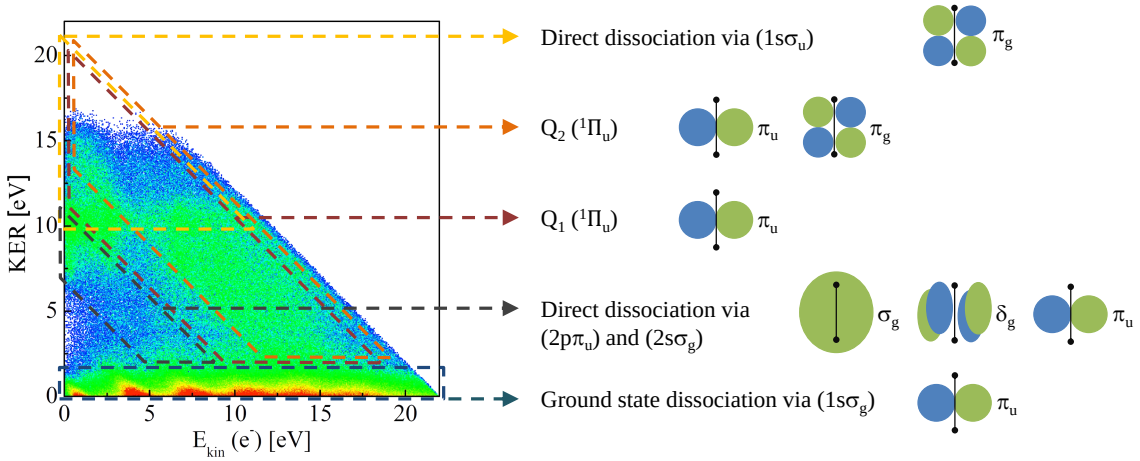

Figure 5.11: Perpendicular transitions: Energy–correlation diagram. The dashed frames represent the energy sections, within which certain processes are expected to occur, such as ground–state and direct dissociation via $(1s\sigma_g)$ and $(1s\sigma_u)$ states, respectively. Moreover, the events which correspond to the autoionization of doubly excited $Q_{1,2}$ states are shown. The right panel illustrates the correlated electron partial waves, π_u and π_g. In the lower energy region, the green marked area denotes transitions to the H_2^+ $(2p\pi_u)$ and $(2s\sigma_g)$ states.

In Figure 5.11 the energy–correlation spectrum is shown for the perpendicular transitions. The labeled energy sections denote the accessible states and present the partial waves that are expected in the emitted electron–wave function. Several differences in the

[6] In comparison to parallel transition the opening angle is chosen to be larger in order to account for an equal solid angle, which in both cases is $\frac{4}{5}\pi$.

energy–correlation spectrum are observed in comparison to the one for parallel transitions. First, the high–harmonic lines which reflect the excitation of Q_1 and Q_2 states are smeared out. Second, the dominant XUV photon energies that populate doubly–excited states in parallel and perpendicular transitions are different. In the case of parallel transitions, the highest contribution is observed for the 17th and 19th harmonic, whereas the 21st harmonic ionization yield is rather low. In perpendicular transitions, the strongest signal is obtained for the 19th and the 21st harmonic which can be related to the large contribution of the lowest dipole–allowed Q_2 state [SM99c]. Third, due to the orientation of the molecule, the ions are ejected perpendicular to the polarization/spectrometer axis, such that their detection efficiency is critical with respect to the ReMi acceptance. This is discernible, as the dissociation yield decreases drastically for KERs higher than 16 eV[7].

As discussed previously, the energy–correlation diagram allows the classification of $H^+ + e^-$ events, according to the populated states. In this context, the lower KER region can be assigned to the ground–state dissociation via $(1s\sigma_g)$, a non–resonant process which is insensitive towards the molecular orientation, such as the direct dissociation via $(1s\sigma_u)$. Note that in this configuration, no wave–packet signal is observed, as the resonant transition between the $(1s\sigma_g)$ and $(1s\sigma_u)$ via an IR photon is only dipole–allowed, if the polarization and the internuclear axes are collinear.

The symmetry of the emitted electrons differs in comparison to the corresponding processes for parallel transitions. Here, the electrons exhibit π_u and π_g patterns instead of σ_u and σ_g, respectively. Such distributions are also encountered, if the dissociation processes evolve over intermediate, doubly–excited states which is illustrated in the following reaction channels:

$$
\begin{aligned}
H_2 &\xrightarrow{\text{XUV}} H_2^+(1s\sigma_g) + e^- && \Rightarrow \quad \Lambda(e^-) = \pi_u \\
H_2 &\xrightarrow{\text{XUV}} H_2^+(1s\sigma_u) + e^- && \Rightarrow \quad \Lambda(e^-) = \pi_g \\
H_2 &\xrightarrow{\text{XUV}} H_2^{**}(Q_n) \xrightarrow{\text{autoionization}} H_2^+(1s\sigma_g) + e^- && \Rightarrow \quad \Lambda(e^-) = \pi_u \\
H_2 &\xrightarrow{\text{XUV}} H_2^{**}(Q_n) \xrightarrow{\text{autoionization}} H_2^+(1s\sigma_u) + e^- && \Rightarrow \quad \Lambda(e^-) = \pi_g
\end{aligned}
\tag{5.5}
$$

Figure 5.12 represents the MFPADs, obtained for different sections within the energy–correlation diagram 5.11. The projections in the first row show the electrons from ground–state dissociation events and provide the same structure as in the parallel case, suggesting the same partial wave in both configurations. However, it must be noted that the molecular axis is now positioned along the x–axis (instead of z), thus explaining the difference between both alignments.

[7] Applying higher spectrometer voltages would increase the acceptance; however, the amount of false coincidences is increased as well, since more electrons which are generated by scattered XUV photons are detected.

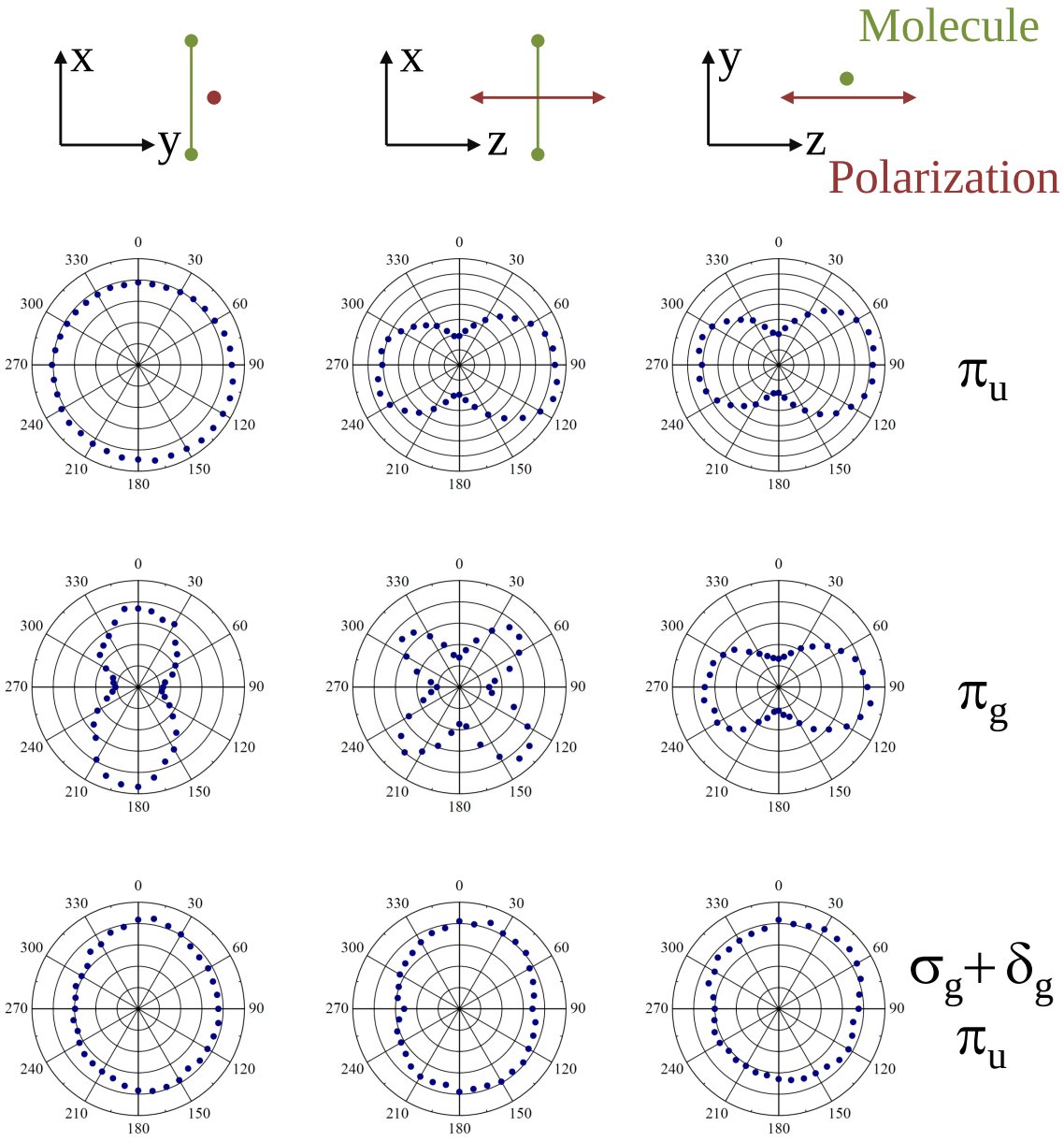

Figure 5.12: Electron angular distributions in perpendicular transitions for three different sections of the energy–correlation diagram. Row 1: MFPADs for an electron π_u partial wave in ionization to the $(1s\sigma_g)$ state. Row 2: MFPADs for an electron π_g partial wave in ionization to the $(1s\sigma_u)$ state. Row 3: MFPADs for electron $\sigma_g + \delta_g$ and π_u partial waves in ionization to the $(2p\pi_u)$ and $(2s\sigma_g)$ states, respectively.

The second row in Figure 5.12 presents the three perspectives onto the π_g partial wave from the direct dissociation events, with $(1s\sigma_u)$ as the final state [DD78]. In the middle image, the typical butterfly structure is extracted which was only partially visible in parallel transitions to the high–energetic states of H_2^+.

In perpendicular transitions it is similarly possible to address the higher H_2^+ states $(2p\pi_u)$ and $(2s\sigma_g)$, populated by the highest harmonic photon energies, resulting in more complex partial waves, with corresponding $\sigma_g + \delta_g$ and π_u symmetries, respectively[8].

$$\begin{aligned} H_2 &\xrightarrow{\text{XUV}} H_2^+\,(2p\pi_u) + e^- &\Rightarrow\ \Lambda(e^-) &= \sigma_g + \delta_g \\ H_2 &\xrightarrow{\text{XUV}} H_2^+\,(2s\sigma_g) + e^- &\Rightarrow\ \Lambda(e^-) &= \pi_u \end{aligned} \tag{5.6}$$

The angular distributions for such transitions in the perpendicular case are shown in the last row of Figure 5.12 and indicate that complex partial waves are involved. However, it is difficult to identify single patterns, and according to the participating channels in (5.6), at least three different partial waves overlap in the distributions.

5.2.3 Asymmetry and localization effects

Within the performed experiments on the XUV–photon–induced dissociative ionization of molecular hydrogen, interference and asymmetry structures are observed in the energy and momentum spectra of the dissociation products. The theoretical basics of this phenomenon are explained in section 3.4. Therefore, only the most important properties of the asymmetry will be discussed here.

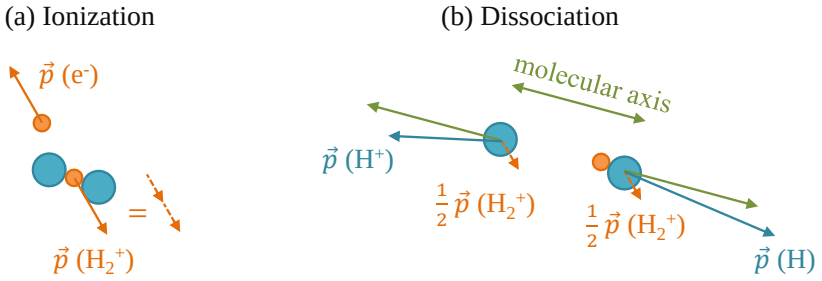

Figure 5.13: A hydrogen molecule is ionized (a) and subsequently dissociates (b) into a hydrogen atom and an ion. The momentum of both fragments are composed of the recoil momentum of the emitted electron and the momentum gained within the dissociation. From the ion and electron momenta the original molecular orientation in the laboratory frame of reference can be reconstructed.

In the dissociative ionization of H_2, it is not possible to detect the neutral hydrogen

[8] The exact representation of the partial wave symmetry is $\Sigma_g^+ + [\Sigma_g^-] + \Delta_g$ and Π_u. In order to distinguish between electron and molecular ion, small letters are used.

atom; however, it can be (virtually) reconstructed from the momentum vector of the H^+ ion, as the ion and the atom carry almost equal masses as illustrated in Figure 5.13. In the reference frame of the parent molecule, both fragments are thus emitted with the same momentum but into opposite directions. It is important to note that the ion–momentum vector must be corrected by the recoil momentum of the electron as depicted in Figure 5.13. Otherwise artificial asymmetry effects are encountered in the analysis, even though the electron momentum is small. Hence, by the measurement of the ion and electron momenta, the reconstruction of the full molecular geometry is possible and, accordingly, a transition between the laboratory and the molecular frame of reference can be conducted (see Figure 5.13 and section 4.4.6). The transition between the two reference frames is necessary in order to resolve any asymmetry effects, as the emission direction of the particles must be analyzed with respect to the original orientation of the molecular axis.

In the present work, the asymmetry is defined by the angle between the electron and ion emission directions in the molecular frame. Here, we define co–propagation (+) if the ion and the electron are emitted into the same hemisphere and counter–propagation (−) otherwise. As an example, this is illustrated in Figure 5.13 (b) for a co–propagating event. Counting respective events $N_+ \rightarrow N_+ + 1$ and $N_- \rightarrow N_- + 1$ for the same data set, we define the asymmetry parameter as:

$$A = \frac{N_+ - N_-}{N_+ + N_-} \tag{5.7}$$

On first glance, it seems counter–intuitive that any asymmetry in the emission of charged particles, i.e. a preference under certain conditions to be emitted into the same or opposite hemisphere with respect to the molecular axis, occurs. This phenomenon, termed "localization" in the literature, is a result of interference, as described in section 3.4.

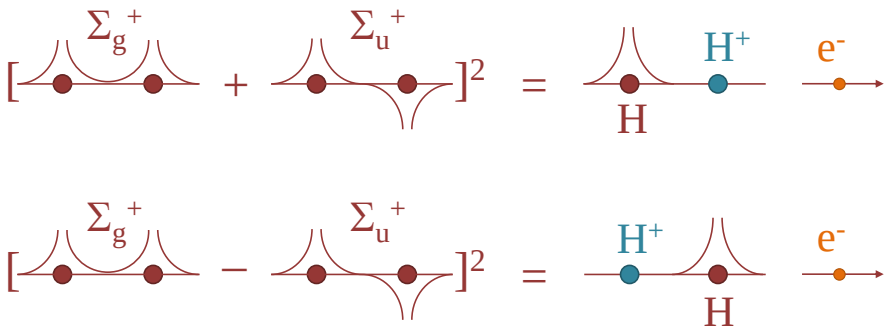

Figure 5.14: Scheme of the electron–ion localization via interference of two wave functions Σ_g^+ and Σ_u^+ symmetries in the final state. The coherent superposition allows two configurations which lead to a localization since the transition matrix element is related to the square of the wave function.

In H_2, the localization is determined by the dissociation into $H^+ + H$ via two possible pathways, the binding ($1s\sigma_g$) and antibinding ($1s\sigma_u$) of the H_2^+ ion. The electrons emitted in these processes exhibit different partial waves which in the case of ($1s\sigma_g$) and ($1s\sigma_u$) correspond to σ_u and σ_g in parallel, or π_u and π_g in perpendicular transitions, respectively. Both states can either be reached in a direct, non–resonant transition or via intermediate, resonant doubly–excited states Q_n, provided an autoionization occurs during dissociation of the involved repulsive Q_n level. Thus, the only constraint for an interference of both paths are equal energies of the fragments in the final state, as different pathways would be distinguishable otherwise. In Figure 5.14 the interference of the binding and antibinding states is illustrated, resulting in the localization of the electron at either one of the nuclei. Note, that an observable corresponds to a symmetric signal, as the transition matrix element is related to the square of the wave functions. As can be seen from the PES in Figure 5.7, a direct involvement of ($1s\sigma_g$) and ($1s\sigma_u$) will barely lead to such an asymmetry, as the energy is inversely distributed between the electron and the nuclear fragments. Ground–state dissociation via the ($1s\sigma_g$) is connected to high energetic electrons and low KERs, whereas direct dissociation via the repulsive ($1s\sigma_u$) results in high–energetic nuclear fragments and comparably slow electrons. The situation changes, when doubly–excited states are populated in an intermediate step, as the autoionization causes kinetic energies to be distributed more equally.

In this study, the asymmetry is analyzed in two configurations, namely where the reconstructed molecular axis and the laser polarization axis are either parallel or perpendicular to each other. This condition enables the distinction between two different origins of the asymmetry, i.e. different interfering pathways.

Asymmetry in parallel transition

In parallel transitions, the 17th and 19th high harmonics, at photon energies of approximately 29.3 eV and 32.8 eV are sufficient to populate the Q_1 state, whereas the 21st harmonic (36.2 eV) mainly contributes in the excitation of the Q_2 level [SM98]. Both series of Q–states feature Σ_u^+ symmetry and both autoionize quickly (see Figure 7.1 (c) in the appendix); however, there exists a pivotal difference concerning the final states. More precisely, Q_1 only autoionizes to ($1s\sigma_g$), while Q_2 attains ($1s\sigma_g$) as well as ($1s\sigma_u$). Insofar, there exist several pathways to ($1s\sigma_g$) and ($1s\sigma_u$) which in principle can all contribute to asymmetry effects in parallel transitions[9]. Figure 5.15 represents the correlated energy spectrum of ions and electrons and shows the measured asymmetry value in the corresponding regions, ranging from -0.6 and 0.6, thus suggesting a very strong localization of the charged fragments in certain energy sections, as compared to localizations previously observed. Red and blue areas hereby correspond to co– and counterpropagating ion–electron

[9] According to [SM99c], the highest contribution in the excitation of a Q_n series is given by the lowest dipole–allowed levels.

pairs, respectively, whereas green marked events show no preferred direction of the particles. As can be seen in Figure 5.15 (b), this localization is particularly strong in the areas

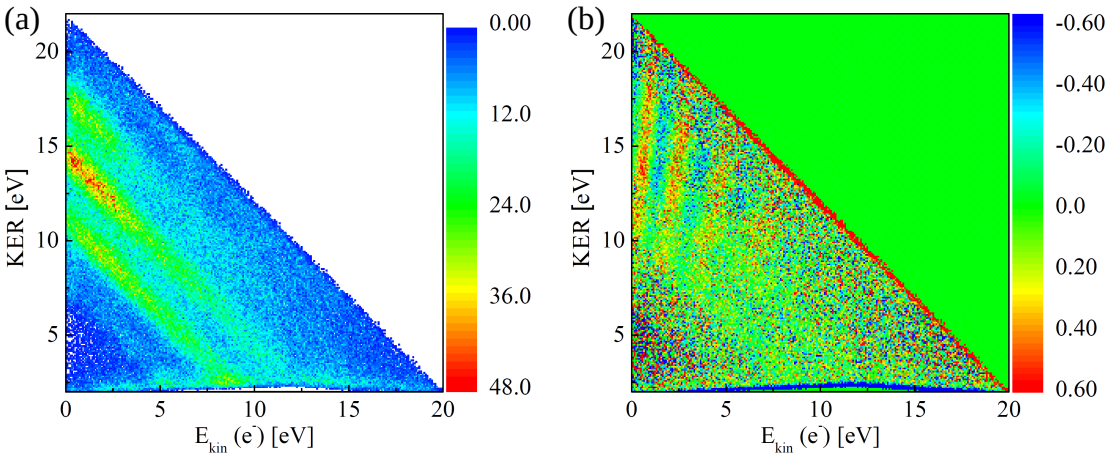

Figure 5.15: Parallel transitions: Energy–correlation diagram (a) and the corresponding asymmetry landscape (b). Left panel (a): The three diagonal lines represent autoionization events along the doubly–excited states and direct dissociation via the $(1s\sigma_u)$ state. Right panel (b): Blue areas mark counter–propagating ion–electron pairs. Red denotes co–propagation.

where the doubly–excited states $Q_{1,2}$ and the direct dissociation via $(1s\sigma_u)$ contribute to the dissociation signal. In the lower KER region, including the ground–state dissociation, as well as the direct ionization via $(2p\pi_u)$ and $(2s\sigma_g)$, the effect disappears completely, such that the following channels are identified to be relevant for the asymmetry:

$$
\begin{aligned}
H_2 &\xrightarrow{\text{XUV, direct dissociation}} && && H_2^+\,(1s\sigma_u) \;+\; e^- \\
H_2 &\xrightarrow{\text{XUV}} H^{**}\,(Q_1) && \xrightarrow{\text{autoionization}} && H_2^+\,(1s\sigma_g) \;+\; e^- \\
H_2 &\xrightarrow{\text{XUV}} H^{**}\,(Q_2) && \xrightarrow{\text{autoionization}} && H_2^+\,(1s\sigma_g) \;+\; e^- \\
H_2 &\xrightarrow{\text{XUV}} H^{**}\,(Q_2) && \xrightarrow{\text{autoionization}} && H_2^+\,(1s\sigma_u) \;+\; e^-
\end{aligned}
\qquad (5.8)
$$

Note that some of the boundaries in Figure 5.15 (diagonal and KER $\sim 2\,\text{eV}$) also show very strong asymmetries; however, this can be attributed to the subtraction of the electron recoil energy from the KER a measure which is necessary, as the evaluation of the asymmetry is referred to the molecular frame of reference. Otherwise, only the emission direction of the electron would be related to the original orientation of the molecule, but not the momentum of the nuclear fragments. This would then cause artificial asymmetry effects, especially in the low KER region. Nevertheless, these features can be identified, since they appear as perfectly parallel or diagonal structures in the energy–correlation diagram. Another

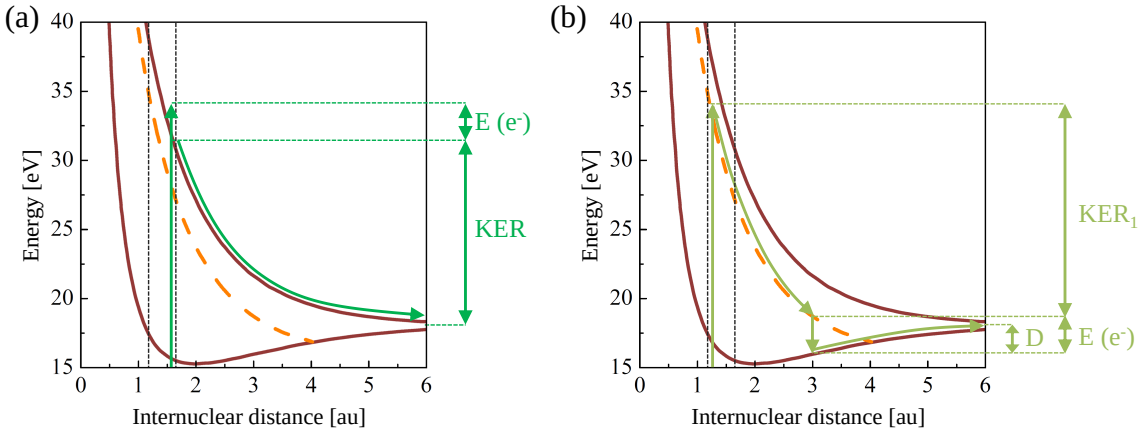

Figure 5.16: Parallel transitions: Illustration of two interfering paths given by (a) the direct dissociation via $(1s\sigma_u)$ or (b) the involvement of the lowest dipole–allowed Q_1 doubly excited state which autoionizes eventually. Note, $\mathrm{KER} = \mathrm{KER}_1 - \mathrm{D}$.

source that could provoke artificial asymmetry is caused by irregularities in the detection efficiency which may happen in measurements involving three–dimensional imaging, such as in ReMis. The influence of this additional effect has been identified and simulated and cannot be related to the measured asymmetry, as it is connected to the laboratory frame of reference.

In Figure 5.16, the origin of ion–electron localization is demonstrated for interfering paths along $(1s\sigma_u)$ and the lowest dipole–allowed Q_1 state which, at a given time, will autoionize to the $(1s\sigma_g)$. The two pictures show the process for one specific, incident photon energy and illustrate, how the final energy distribution between electrons and ions becomes identical in both pathways. This indistinguishability of kinetic energies is a crucial requirement for interference and asymmetry to occur. For the direct dissociation channels via $(1s\sigma_g)$ and $(1s\sigma_u)$ the corresponding ion and electron energies are easily separable, therefore, no asymmetry effect will follow from them.

An approach to represent the asymmetry without subtracting events $(N_+ - N_-)$ is demonstrated in Figure 5.17 using the angle α between coincident ions and electrons and its dependence on the electron kinetic energy. Here, events corresponding to red and blue colored areas in Figure 5.15 appear on opposite sides of the ordinate. The spectrum shows the electron energy in a total kinetic energy band $E_{\mathrm{kin,\,total}} = KER + E_{\mathrm{kin}}(e^-)$ between 12 and 20 eV, thus representing the significantly asymmetric events. Note that the cosine of α is plotted, accounting for a full solid angle correction. Values around $\cos(\alpha) = 1$ denote co–propagating particles, whereas as -1 corresponds to events where ions and electrons are emitted back to back. The asymmetry in this representation can be traced to energy values up to 8 eV which seems correct regarding the limits of the applied photon energies. Even higher photon energies, which are not available within the present high–harmonic

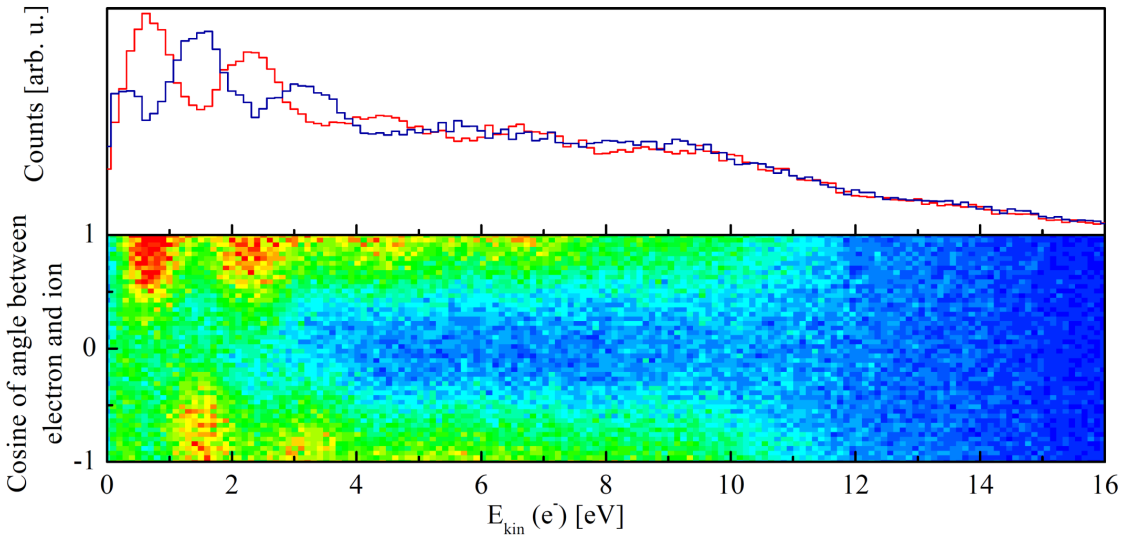

Figure 5.17: The asymmetry in a different representation. Here, the cosine of the angle between the internuclear axis and the corresponding electron as a function of its energy is shown. The energy peaks show a clear $\pi/2$ phase shift between co- ($+1$ and red in the projection) and counter- (-1 and blue in the projection) propagating electrons and ions.

spectrum, would increase the range of autoionizing events and, thus, of electron kinetic energies that interfere with the direct dissociation.

Figure 5.17 further contains two projections onto the electron energy axis – one including the events with $\cos(\alpha) < 0$ and one with $\cos(\alpha) > 0$, showing a clear phase shift of π. The red and blue curves corresponds to electron energies for angles $\alpha < 90°$ and $\alpha > 90°$, respectively.

The following discussion will address the specific structure of the asymmetry within the correlated energy map and explain the origin of the oscillation in Figure 5.15 (b), especially with respect to three additional characteristic features that are clearly visible:

(a) The oscillations depend more on the electron energy than on the KER.

(b) The oscillations broaden with increasing electron energy.

(c) The lines of constant asymmetry are slightly tilted (to the right).

In order to understand these features, a semiclassical simulation of the dissociation along the three PES from Figure 5.16 was performed and is shown in 5.18 (b) [Fis12]. Here, the molecular fragments gain kinetic energy either during the dissociation along the $(1s\sigma_u)$ or along the lowest dipole–allowed Q_1, with subsequent autoionization to the $(1s\sigma_g)$. These two possible, direct and indirect pathways shall be referred to as path 1 and path 2, respectively. In the simulation, the integration over the acquired momentum gives rise to an

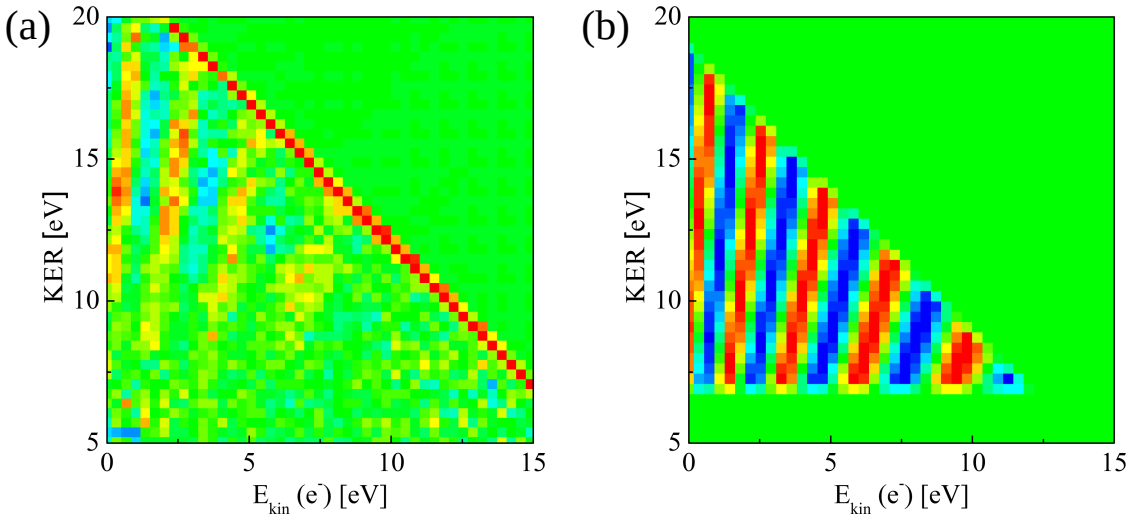

Figure 5.18: (a) Measured asymmetry and (b) semiclassical simulation of the process. All features of the oscillating structure are reproduced and can be referred to the curvature and position of the relevant PES. Here, the main discrepancy is given by the amplitude of the asymmetry values.

accumulated phase in the dissociation limit. This phase depends on the curvature of the corresponding PES, the initial photon energy and the internuclear distance (or position within the Franck–Condon region) where the transition occurs. For the interference of both trajectories, the following points are taken into consideration: First, interfering paths 1 and 2 are initiated by photons of identical energy. Otherwise, the corresponding events are distinguishable (classically) and appear on different "coordinates" in the energy–correlation map 5.15 (a). This further means that interfering trajectories result from different starting positions within the Franck–Condon region. Second, the transitions are chosen such that final electron and ion energies are equal for both pathways. This requirement is fulfilled by adapting the autoionization time in path 2 to the resulting electron energy in path 1; however, with this restriction, the autoionization is no longer a statistical process. Third, the width of the Franck–Condon region determines the triangular shaped area in the energy–correlation diagram where localization is expected.

The result of the simulation is presented in Figure 5.15 (b) and the comparison to the measured asymmetry in (a) shows an excellent agreement. Here, the oscillation in the asymmetry can be explained by the phase difference in path 1 and 2 for all (allowed) combinations of photon, electron and ion energies. The shape of the structure including width, tilt and broadening for higher electron energies can be reproduced and suggests that the position and curvature of the relevant PES are the crucial parameters. A future step in the evaluation would be to describe the amplitudes of the asymmetry and, thus, to determine correct expressions for the coefficients c_1 and c_2 in equation (3.38), section 3.4.

Asymmetry in perpendicular transitions

In perpendicular transitions, where the polarization and the molecular axis are oriented close to an angle of 90° with respect to each other, several asymmetry scenarios are possible. Not all of these asymmetries reveal localization structures as those described earlier, instead they can feature energy spectra with an oscillating amplitude [Mar+07]. A few of these phenomena have been observed experimentally with monochromatized linear polarized synchrotron light in combination with a reaction microscope and were investigated theoretically [Mar+07]; however, the description has not included the correlation between ion and electron energies.

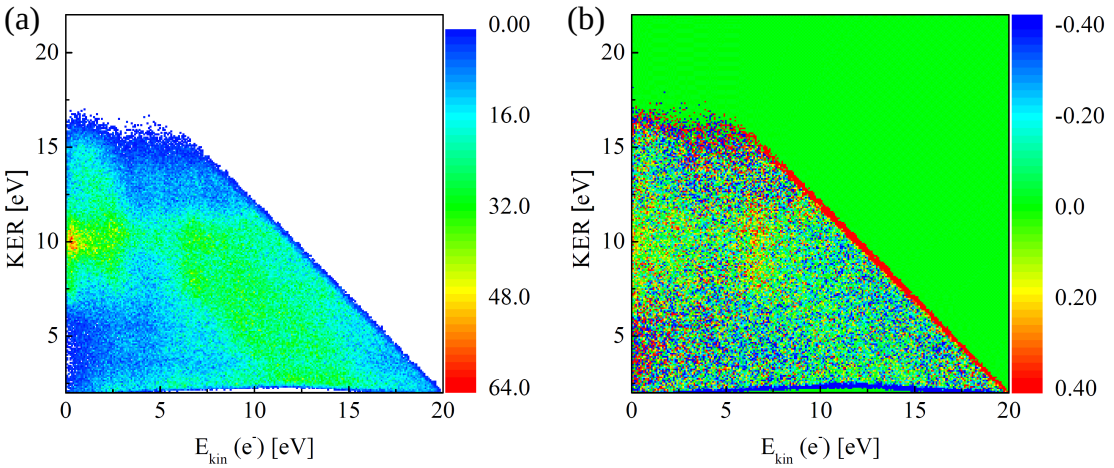

Figure 5.19: Perpendicular transitions: Energy–correlation diagram (a) and the corresponding asymmetry landscape (b) where blue areas mark counter–propagating ion–electron pairs and red denotes co–propagation. The asymmetry is not clear at first view; however, some areas feature an enhanced localization.

In Figure 5.19 the energy–correlation diagram is shown together with the corresponding measured asymmetry. There are a few differences with respect to the parallel transitions which should be mentioned: First, the diagonal lines in Figure 5.19 (a), which represent the autoionization of the doubly–excited states, are less pronounced and cover different photon energy ranges. These can be ascribed mostly to the 19th and 21st high–harmonic photons which populate $Q_2\,^1(\Pi_u)$ states. Second, many events can be assigned to the direct dissociation via the $(1s\sigma_u)$, $(2p\pi_u)$, $(2s\sigma_g)$ and late autoionizing $Q_1\,(^1\Pi_u)$ states[10] and they form an intense and blurred structure in the high–KER and low electron–energy region. Third, the asymmetry profile in 5.19 (b) does not reveal oscillating structures as in the parallel event selection. Nevertheless, there exist areas in the energy–correlation diagram where a considerable amount of localization is observed, and which can be explained by a

[10] $Q_1\,(^1\Pi_u)$ states feature large autoionization times (~ 100 fs) at internuclear distances close to the Franck–Condon region (see Figure 7.1 (d) in the appendix).

simple model with autoionizing Q_2 states as proposed in [Mar+07]. In particular for KER $\approx$ 10 eV and $E_{\mathrm{kin}}(e^-) \approx 7$ eV an enhanced red structure is recorded.

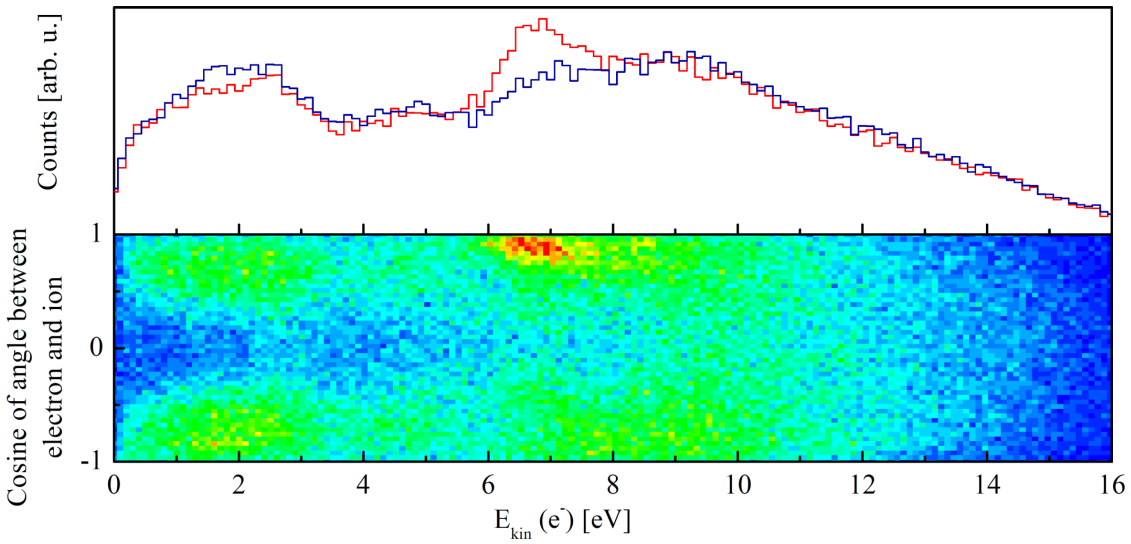

Figure 5.20: A different perspective on the asymmetry, shown by the cosine of the angle between ion and electron in the molecular frame of reference. The projections denote co- (+1 and red) and counter- (−1 and blue) propagating electrons and ions. An enhanced structure is visible at 7 eV.

A better visualization of this feature can be achieved by specifically selecting events where the total kinetic energy corresponds to transitions induced by photons of the 19th and 21st harmonic lines. For these photon energies, doubly excited Q_2 states with Π_u symmetry are effectively populated. The event selection can be rearranged by plotting the electron energy against the cosine of the angle between the emitted ions and electrons. The results are shown in Figure 5.20 and demonstrate a strong signal in the upper half at approximately 7 eV. In this representation, events which are close to $\cos(\alpha) \approx 1$ include ions and electrons that are emitted into the same direction, whereas $\cos(\alpha) \approx -1$ corresponds to counter–propagating particles. The stronger signal of co–propagating ion–electron pairs at 7 eV is also obvious in a comparison between the projections of both halves ($\cos(\alpha) < 0$ and $\cos(\alpha) > 0$). Surprisingly, the projection of both sides does not show any further deviation in the signal amplitude and, accordingly, no asymmetry towards counter–propagating ion–electron pairs.

At this point, it is necessary to explain the underlying process that leads to an asymmetry in the recorded energy range. In [FM09] it is suggested that the interference of two dissociative ionization trajectories, arising from the same doubly excited state, are responsible for such a structure. These mechanism are visualized in Figure 5.21, together with the expected energy ranges of the fragments. Both pathways result from dipole–

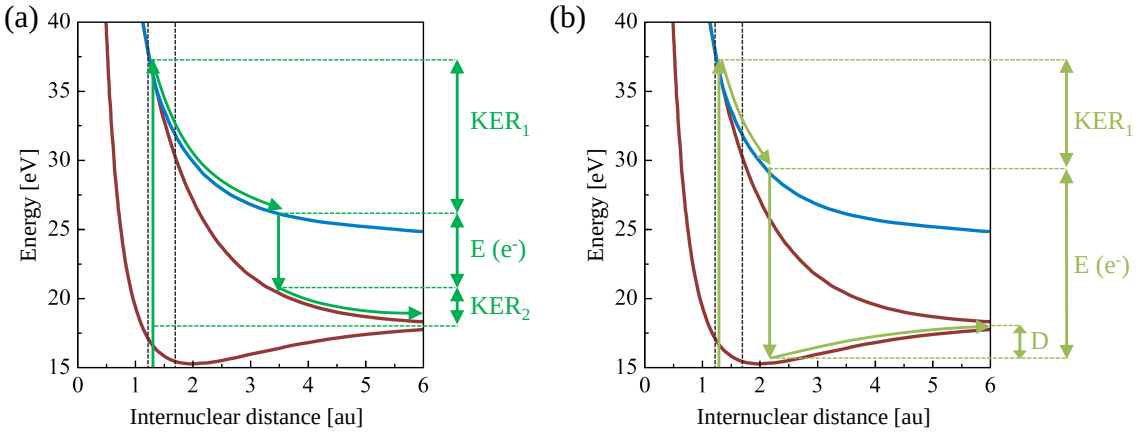

Figure 5.21: Perpendicular transitions: The contribution of two interfering pathways leading to asymmetry, via autoionizing Q_2 states. (a) and (b) represent the autoionization to the $(1s\sigma_g)$ or the $(1s\sigma_u)$ PES of H_2^+, respectively [SM99a].

allowed transitions to Q_2 states which autoionize comparatively slow to either the $(1s\sigma_g)$ state in (a) or the $(1s\sigma_u)$ level in (b) of H_2^+. Note, that the KER in (a) is calculated as $KER = KER_1 + KER_2$, whereas in (b) its $KER = KER_1 - D$. Depending on the autoionization time, the fragments can gain different amounts of energy and, in the case of a fast autoionization, the energy distribution along both paths is rather different, almost as much as in the direct population of the H_2^+ states. Only for late autoionizing events, the energies for electrons and ions are distributed equally in both trajectories which finally results in a sharp localization–effect at approximately 7 eV for the electron energy.

It must be emphasized that the semiclassical view of the different dissociation pathways, based on the trajectories on the respective PES, is insufficient to completely explain the asymmetry [Mar+07]. In a full quantum mechanical treatment, the inclusion of all Q_2 states leads to broad ionic and electronic energy distributions via both channels. Thus, the energy region where localization is expected to occur becomes comparably broad, and a second glance at the asymmetry diagram in Figure 5.19 (b) on the enhanced red structure at KER $\approx$ 10 eV and $E_{\text{kin}}(e^-) \approx 7$ eV confirms this conclusion.

In order to identify and approve the proposed pathways, it is necessary to analyze the electron angular distributions from those events where the asymmetry is observed ($E_{\text{kin}}(e^-) = 7 \pm 1$ eV and KER$= 10.5 \pm 1$ eV). The corresponding two–dimensional MF-PAD projections onto the (x, y), (x, z) and (y, z) are shown in Figure 5.22. Here, the three diagrams reveal a superposition of two partial waves, mainly π_g and less evident π_u. π_g is easily identified by the two–lobe structure in the (x, y) and (y, z) planes and the "butterfly" shape in (x, z) (compare with Figure 3.5 in the theoretical discussion on electron angular distributions, section 3.2.2). In contrast, the existence of a π_u partial wave is only indicated by a "deformation" of the angular distributions. In the (x, y) plane, for instance,

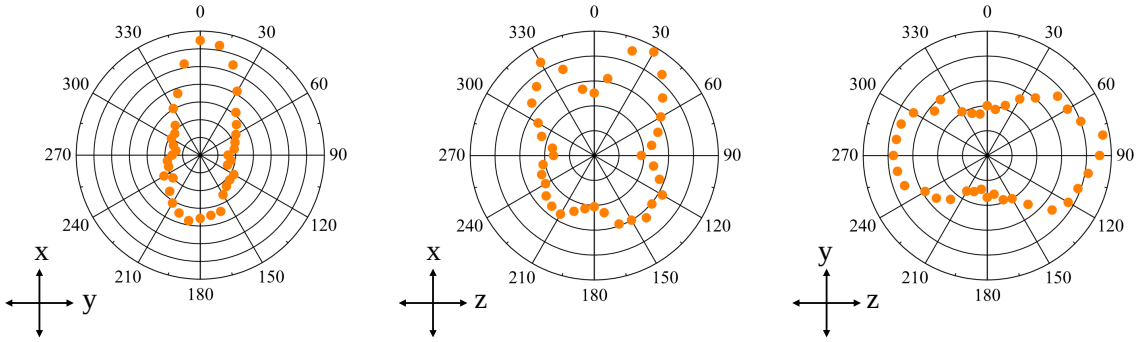

Figure 5.22: Two–dimensional representations of the MFPADs for KER $\approx$ 10 eV and $E_{\text{kin}}(e^-) \approx 7$ eV. The patterns can be attributed to a π_g and π_u partial waves.

the two–lobe structure resembles an ellipsoidal shape and the "butterfly" structure in the (x, z) plane is less pronounced in comparison to Figure 5.12. With these considerations, it is possible to identify the relevant localization channels:

$$\begin{aligned} H_2 &\xrightarrow{\text{XUV}} H^{**}(Q_2) \xrightarrow{\text{autoionization, slow}} H_2^+(1s\sigma_g) + e^- \\ H_2 &\xrightarrow{\text{XUV}} H^{**}(Q_2) \xrightarrow{\text{autoionization, slow}} H_2^+(1s\sigma_u) + e^- \end{aligned} \tag{5.9}$$

Note, all three MFPADs in Figure 5.22 exhibit an asymmetric distribution. In the x–direction this asymmetry corresponds to the discussed localization–effect whereas along the z–axis, the asymmetry is related to differences in the detection efficiency.

5.3 Doubly–excited states dynamics explored by an XUV–IR pump–probe scheme

Time–dependent studies on the photon–induced autoionization and neutral dissociation dynamics of hydrogen molecules have been performed in the last decade, investigating for example the single pulse response of the dissociation yield with varying XUV pulse durations [SBM06]. Hereby it became apparent that different sub–femtosecond pulse durations lead to an extremely diverse set of possible energies of the emitted particles.

In [GC+12] it was shown that in experiments with single–XUV photons it is not possible to coherently control different reaction pathways in the molecules, even by changing parameters such as the pulse duration, the phase or the polarization. Even if a variation of the ionization probabilities with the pulse length is observed, according to the authors of this study, its origin can be related to the spectral properties of short laser pulses instead of their duration. Therefore, the only possible means to access and investigate the autoionization dynamics in doubly–excited states with single photons, as well as reaching

the goal of coherent control of chemical reactions, is the application of pump–probe type laser setups, including one pulse at high photon energies.

A benchmark experiment in this context has been performed by Sansone et al. [San+10; San+12], reporting a localization of the electronic charge distribution in the molecular frame, being dependent on the time–delay between XUV and IR pulses. The measurement has been conducted with single attosecond pulses in a very small delay range of $\sim 20\,\mathrm{fs}$.

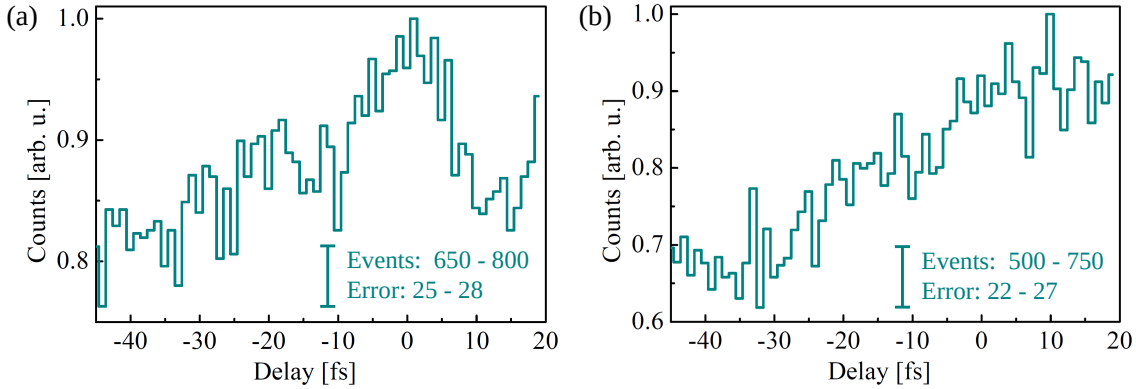

Figure 5.23: Number of events versus XUV–IR delay for parallel (a) and perpendicular transitions (b). In both cases, events from the region of interest are selected from the correlated energy spectrum. The counts are normalized to the maximum peak. Negative and positive delay values correspond to early and late IR pulses, respectively. The maximum error–bar size is shown for completeness.

In the work presented here, the delay range covered 65 fs around the temporal overlap region of the pulses[11]. The experiment contains all previously discussed processes, such as ground–state dissociation, the observation of the vibrational wave–packet dynamics as well as the single XUV–photon induced population of doubly–excited states of H_2 and repulsive states of H_2^+.

The XUV–IR delay–dependent measurement on the population of doubly–excited states is shown for parallel and perpendicular transitions in Figure 5.23. Note, since the nuclear wave–packet dynamics features a strong delay dependency, it is necessary to consider only events with a KER above 3 eV. This condition is applied to Figure 5.23, allowing to resolve the principal temporal features for both transitions: In parallel transitions, the dynamics appears largely confined symmetrically within the temporal overlap region, if the existence of pre–IR–pulses is considered, as discussed in section 5.1.2. These pre–IR–pulses are of lower intensity ($< 20\,\%$ of the main pulse); however, their influence is visible as an enhanced signal between -30 to $-10\,\mathrm{fs}$.

For the perpendicular transitions, the delay dependence resembles a linear increase with

[11] The corresponding delay measurement is shown in the lowest diagram of the wave–packet dynamics in Figure 5.3 in section 5.1.2.

an enhancement near the temporal overlap region at 0 fs. The features in both transition types can be explained by the corresponding doubly–excited states and their properties, including symmetry and autoionization times. This will be elucidated in the following two sections.

5.3.1 Parallel transitions in an XUV–IR pump–probe scheme

In a recent theoretical work by Silva et al. [SRM12], APTs together with short IR pulses were considered to induce dynamical changes in the population of doubly–excited states in a 5 fs delay–range within the overlap region of the pulses. Several interesting findings, such as the appearance of sideband structures in different energy areas were reported, and can be verified with the present data set. The calculations show that in a two–color pump–probe configuration, with parallel polarized laser beams, the main contribution to sidebands is expected in the low kinetic energy region of the ions, where the ground–state dissociation takes place. The total kinetic energy spectra in Figure 5.24, for events inside and out-

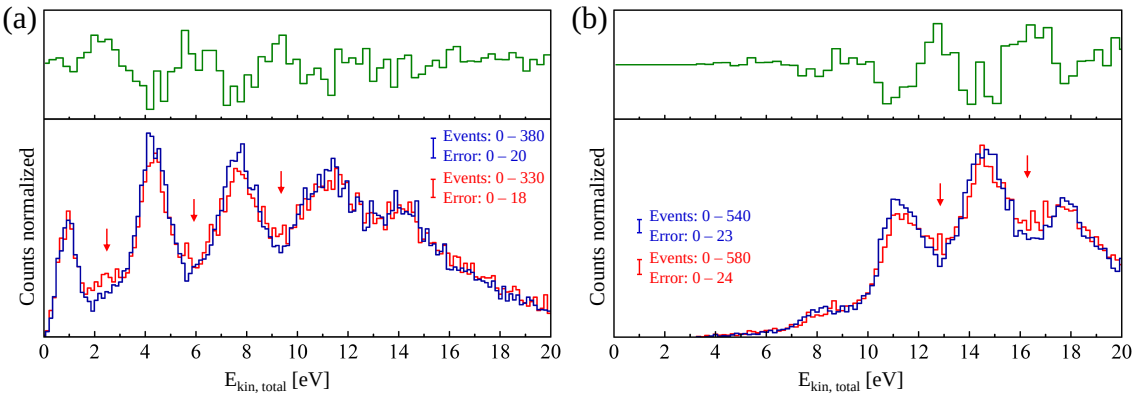

Figure 5.24: Parallel transitions: Total kinetic energy for the low and high KER regions, 5 fs inside (red) and outside (blue) of the pulse–overlap range and the difference of both signals (green). Small sidebands peaks, denoted by red arrows, between the main XUV ionization lines are visible in (a) the ground–state dissociation range (KER = $0-3$ eV) as well as in (b) the doubly–excited states (KER = $3-20$ eV).

side of the overlap interval of the pulses, indicate an enhanced signal between the main ionization peaks of the HHG–XUV photons, suggesting a sideband–oscillation process similar to those measured and theoretically described with rare–gas atoms [Pau+01; VTM96; Mai+03]. This processes can be described as follows: The absorption of single–XUV photons and of two photons (XUV + IR) from the temporally and spacially overlapping APTs and the IR field leads to main ionization peaks and sidebands, respectively. All peaks are energetically separated by ω_0 as the energy spacing of the high harmonics is $2\omega_0$, as indicated in Figure 5.26. Note, for each sideband there are two indistinguishable contributions, where one comes from the absorption of an IR-photon together with a primary

XUV harmonic transition, and the other corresponds to the emission of an IR–photon from the consecutive primary XUV–harmonic transition. Provided that the individual pulses within the APTs are short, i.e. the intra-harmonic dispersion is small enough, the observed sideband intensity as well as the main ionization peaks show a periodic modulation with a period equal to the half–cycle period of the fundamental laser pulse ($\frac{T_0}{2} = \frac{\pi}{\omega_0}$), when the XUV-IR delay is varied [Spe+10].

Figure 5.24 (a) and (b) represent the corresponding results for energy regions corresponding to the ground–state dissociation and autoionization of doubly–excited states, respectively. The IR–induced additional counts between harmonic lines appear in the delay–range, where the temporal overlap is expected; however, the pre–IR–pulses that have been discussed in the previous section 5.1.2, also form sidebands for small negative delays. Together with the fact that a long–term stability of the XUV–IR interferometer is not achievable in this setup, especially not for the corresponding long delay interval, it is impossible to resolve oscillations on a sub–cycle basis.

Nevertheless, the measurement provides the possibility to detect dynamic features in the doubly–excited states, that are encountered in [SRM12]. The comparison of the energy–correlation diagram for two different sections each of 5 fs duration – one where sidebands in the doubly–excited states are expected (Figure 5.25 (a)) and another one where these structures should not appear (Figure 5.25 (b)) – reveals differences that confirm the theory. The diagonal lines in both spectra correspond to autoionizing doubly–excited states. In the areas in between two of these lines, events can be attributed to the simultaneous absorption of an XUV and an IR photon. The overlap region in Figure 5.25 (a) thus features a clear indication for sidebands. In addition, Figure 5.25 (c) represents the subtraction of the two

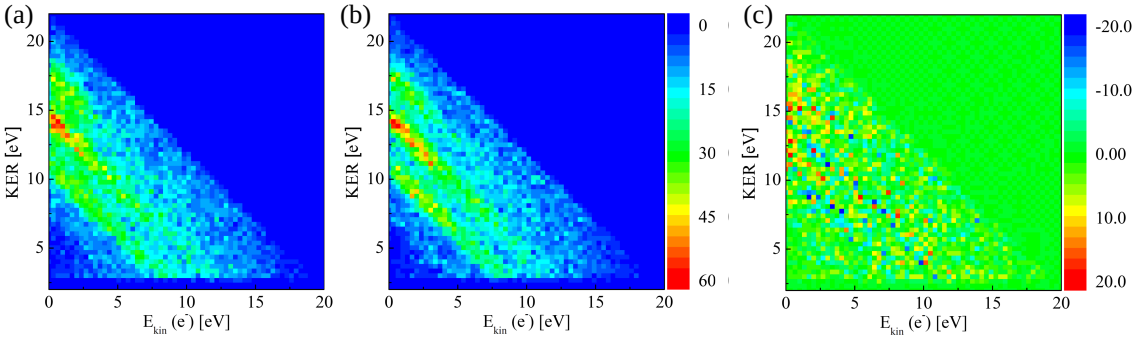

Figure 5.25: Parallel transitions: Correlated energy diagram for delay ranges of 5 fs (a) inside and (b) outside of the pulse–overlap area as well as an (c) subtracted plot of both. In the overlap region, the diagonal lines appear washed out suggesting the existence of sideband structures.

previous plots, revealing a redistribution of events along the sidebands via the absorption or emission of an IR photon. This is encountered in yellow/red diagonal lines which

correspond to signals of sidebands in the overlap region.

According to Silva et. al [SRM12], the additional sideband peaks follow from a "direct" population of doubly excited Q_1 states of $^1\Sigma_g^+$ symmetry via a two–photon XUV–IR absorption, as shown in Figure 5.26. This interpretation does not exclude a sideband–generation process with intermediate states which in the case of H_2^{**} correspond to the single–XUV photon induced transitions to the $Q_1\,^1\Sigma_u^+$ levels; however, the probability for this is low, as two "sequential" resonant transitions are necessary. In summary, this means that the blue and red diagonal lines in Figure 5.25 (c) are related to the autoionization of $^1\Sigma_u^+$ and $^1\Sigma_g^+$ states, respectively. Note, both doubly excited state series, the $Q_1\,^1\Sigma_u^+$ and $Q_1\,^1\Sigma_g^+$, exhibit similar autoionization times which are in the range of a few femtoseconds (see Figure 7.1 (a_1) and (a_2) in the appendix). This is also confirmed by the similarity of the energy distribution between ions and electrons in the sidebands and the main lines, as the red and blue lines in the energy–correlation map in Figure 5.25 (c) show comparable lengths.

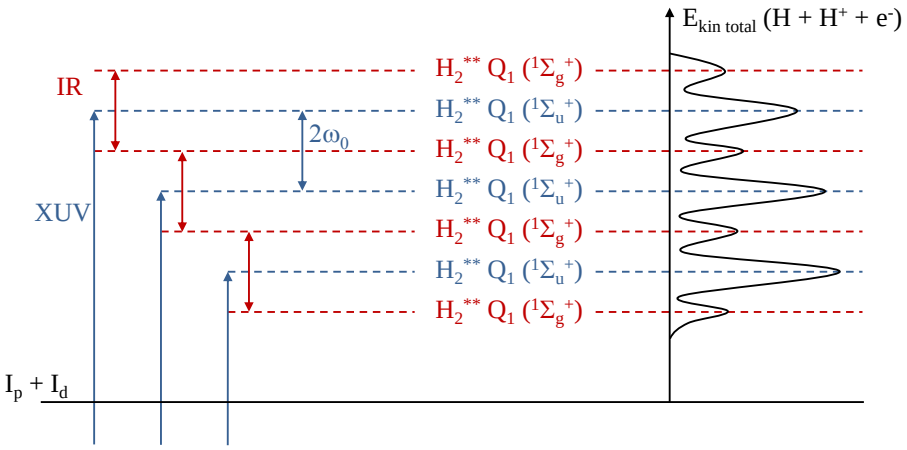

Figure 5.26: Generation of sidebands by two–photon XUV–IR absorption, visible in the total kinetic energy spectrum. Here, $H_2^{**}\,Q_1$ states with $(^1\Sigma_g^+)$ symmetry are populated, in contrast to $(^1\Sigma_u^+)$ states in single–XUV photon transitions.

It is important to mention that the small sideband signal is only obtained within the XUV–IR overlap region, between 0 ± 10 fs, see Figure 5.23 (a). More insight into the dynamics therefore requires a short sub–10 fs scan, as well as an improved interferometric stability, during the experiment. This will be subject to future investigations.

5.3.2 Perpendicular transitions in an XUV–IR pump–probe scheme

The delay dependence in parallel and perpendicular transitions can be attributed to different processes, a fact that is already illustrated by comparing the delay plots in Figure 5.23 (a) and (b). Another indication for this difference is given by the lack of sideband signals

in the perpendicular case, as shown in the total kinetic energy spectra in Figure 5.27. This applies to both, the low– and high–KER region which are related to the ground–state

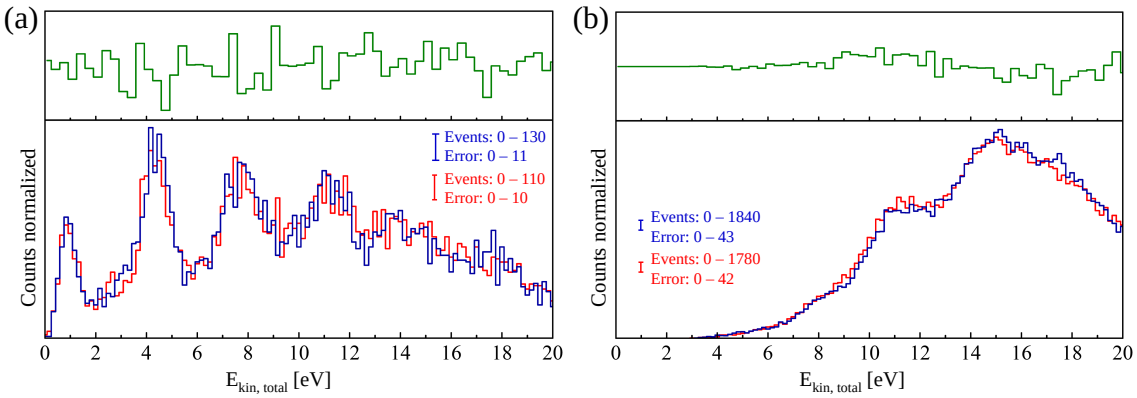

Figure 5.27: Perpendicular transitions: Total kinetic energy for the low and high KER regions, 5 fs inside (red) and outside (blue) of the pulse–overlap range and the difference of both signals (green). Sideband peaks between the main XUV ionization lines are not visible neither in (a) the ground–state dissociation range (KER $= 0 - 3$ eV) nor in (b) the doubly–excited states (KER $= 3 - 20$ eV).

dissociation in (a) and the autoionization of doubly–excited states in (b). However, as the contribution of sidebands in general is rather low, it is not appropriate to consider both total kinetic energy curves as evidence for a non–existing sideband generating process in perpendicular transitions. In particular, Figure 5.27 (b) features comparably broad peaks, such that small sideband–like structures could be covered.

A more significant indication for temporal dynamics is visible in the correlated energy spectra for different delay intervals. In Figure 5.28 (a) and (b) which represent the overlap and non–overlapping region of the pulses, respectively, a visible difference in the yield appears at low kinetic energies of the electrons and values for the KER of approximately 10 eV. This region corresponds to directly ionized and dissociating hydrogen molecules via the $(1s\sigma_u)$, $(2p\pi_u)$ and $(2s\sigma_g)$ states, and in addition, to late autoionizing events from doubly excited Q_1 $(^1\Pi_u)$ states. However, the afore–mentioned arguments referred to processes that involve only single XUV photons. In order to verify if further energy regions are relevant concerning XUV–IR temporal dynamics, it is important to generate a subtraction diagram, as shown in Figure 5.28 (c). It can be inferred that IR pulses mostly transfer Q_1 doubly excited hydrogen molecules non–resonantly to the $(1s\sigma_u)$ where they dissociate and emit electrons of low energy.

It is clear, the Q_1 states are not sufficient to describe the enhanced population in the alleged $(1s\sigma_u)$ region, as their minimum resulting KER $= 10.5$ eV, whereas the signal covers values down to approximately KER $= 6$ eV. A similar process can be found in the XUV–induced excitation of Q_2 states which are promoted by an IR pulse to the dissociating

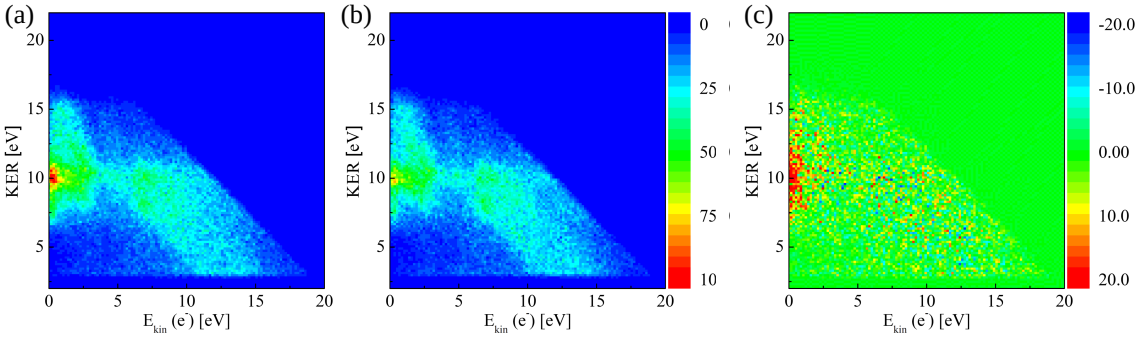

Figure 5.28: Perpendicular transitions: Correlated energy diagram for delay ranges of 5 fs (a) inside and (b) outside of the pulse–overlap area as well as (c) a subtracted plot of both.

$(2p\pi_u)$ state. The dissociation limit of the corresponding PES is 10.2 eV higher than the $(1s\sigma_u)$ PES which results in lower kinetic energies of the ions and neutral atoms. Such events are expected between $4 - 12$ eV, thus covering the lower part of the delay dependent region in the energy spectrum. In the high–energetic fraction of the structure (KER $\sim$ 15 eV), the decreasing ion–detector acceptance reduces the amount of recorded events, so that the full dynamic range is possibly not visible. In summary, it is possible to extract the two–color pump–probe relevant channels for perpendicular transitions which are listed in Table 5.2.

State transition			Energy range of Q_n states	Total energy
$Q_1(^1\Pi_u)$	$\xrightarrow{\text{IR}}$	$H_2^+(1s\sigma_u)$	$28.5 - 37$ eV	$10.5 - 19$ eV
$Q_2(^1\Pi_u)$	$\xrightarrow{\text{IR}}$	$H_2^+(2p\pi_u)$	$32 - 40$ eV	$4 - 12$ eV
$Q_2(^1\Pi_u)$	$\xrightarrow{\text{IR}}$	$H_2^+(2s\sigma_g)$	$33 - 41$ eV	$5 - 13$ eV

Table 5.2: Overview of the energy range of $Q_n(^1\Pi_u)$ states in possible perpendicular transitions, involving an infrared photon (IR). The expected total kinetic energy of the three particles (H^+, H and e^-) is also presented, in order to provide comparison with the correlated energy spectrum.

5.3.3 Discussion and outlook

The XUV–IR delay–dependent measurements on the population of doubly–excited states have revealed interesting features, such as sideband oscillations in parallel transitions and the depletion of doubly–excited states in perpendicular transitions. In particular, for $Q_1(^1\Pi_u)$ states this setup allows one to study the dependence of the autoionization time

from the internuclear distance of the molecule. These states feature very long autoionization times of approximately 100 fs in the Franck–Condon region of the H_2, as illustrated in Figure 7.1 (d). After populating $Q_1(^1\Pi_u)$ states with short XUV pulses, the repulsion of the nuclear fragments leads to larger internuclear distances and the autoionization times decrease to values of a few femtosecond. This property can be studied by probing the doubly excited molecules with short IR pulses in the positive delay range. To date, such information has been obtained only indirectly by spectroscopic methods, investigating the fluorescence light emission of doubly excited, (neutral and autoionizing) dissociating H_2 molecules [GM+10].

Nevertheless, the experimental conditions have to be improved in order to increase the cross section for IR–probing of doubly–excited states as in all spectra the dominant signal is connected to single XUV–photon absorption and only a few events can be related with high probability to XUV + IR absorption.

The following discussion will address a few technical difficulties. In general, the effect of a delayed IR pulse on the decay–dynamics of the doubly–excited states is very difficult to measure and, in comparison to the previously discussed wave–packet dynamics, the corresponding signal is much lower. The relatively strong IR dependence of the wave–packet dynamics can be explained by the fact that 98 % of all events result in bound, but vibrationally excited H_2^+ molecules, of which some are forced to dissociation by an absorbed IR photon via bondsoftening [Buc+90; GS+95]. These events then provide a considerable additional signal to the XUV induced fragmentation alone, thus suggesting a strong IR coupling and a good spatial overlap in the reaction volume of the hydrogen target. Measuring an XUV–IR delay dependence in the energy region of doubly–excited states is less probable and only small signatures have been observed.

Another technical issue that has been already discussed in section 5.1.2 is the contribution of an infrared pre–pulse in the KER versus delay spectrum, a circumstance that has to be considered for any delay–dependent analysis. The influence of the additional substructure only provided a small background signal in the nuclear wave–packet dynamics which did not compromise the results. This could be verified in a simulation with two overlaid datasets with the same amount of spectral components.

A third consideration concerning the time–dependent measurement arises from the fairly long delay range of 65 fs which has been necessary in order to exploit the dynamics in perpendicular transitions; however, this reduces the statistics within the overlap region. Furthermore, sub–cycle structures are washed out, as it is impossible to maintain a long–term interferometric stability in the high–harmonic generation chamber until delay–dependent structures become visible. In a short delay range around the overlap region, for example 10 fs, it is often possible to compensate small interferometric drifts by means of a post analysis [Rie12].

6 Summary and outlook

In this work, experiments on one– (XUV) and two–photon (XUV + IR) induced dissociative ionization of molecular hydrogen have been analyzed and the results include various interesting processes and phenomena. It was possible to observe these effects with a high degree of distinguishability using the technique of coincident three–dimensional momentum spectroscopy with a reaction microscope. The measurements have been carried out with ultrashort, XUV–attosecond pulse trains and femtosecond IR pulses. Both, the laser system and the reaction microscope were implemented in a table–top setup at the Max–Planck–institute for nuclear physics in Heidelberg.

The experimental results were classified in four different processes, depending on the light sources (XUV or XUV + IR), the energy range of the detected ions and electrons as well as the corresponding angular distributions which are strictly connected to specific states and pathways. In addition, it was possible to reconstruct the original orientation of each molecule with respect to the polarization direction of the laser and, thus, to differentiate between different geometrical configurations. Following these considerations, the measurements were categorized into four subjects, all presented in chapter 5:

- XUV $\rightarrow$ Ground–state dissociation, section 5.1.1.
- XUV + IR $\rightarrow$ Wave–packet dynamics, section 5.1.2.
- XUV $\rightarrow$ Doubly–excited states and asymmetry phenomena, section 5.2.
- XUV + IR $\rightarrow$ Temporal dynamics of doubly–excited states, section 5.3.

The dominant process in the interaction of H_2 molecules with XUV photons from the HHG–light source is the single ionization which leads to bound and vibrationally excited H_2^+ ions in the $(1s\sigma_g)$ electronic state. A few (2%) of these molecules are excited to vibrational continuum states (above the threshold of 18.1 eV) and fragmentize into low–energetic H atoms and H^+ ions, an effect referred to as ground–state dissociation.

By means of a two–color XUV–IR delay–dependent measurement it was possible to analyze the bound H_2^+ molecules further. Initially, the absorption of an XUV photon from an attosecond pulse train leads to an instantaneous and coherent excitation of vibrational levels which overlap and form a nuclear wave packet. The motion of this wave packet within the boundaries of the binding $(1s\sigma_g)$ potential could be investigated by irradiating the molecule with short, delayed IR pulses. Thereby, the crucial point was that the yield

of IR–induced dissociation into $H + H^+$ depended on the localization of the wavepacket within the potential. This finally led to the observation of an oscillation of the nuclear wave packet as well as a de– and re–phasing as a function of the XUV–IR delay. In a measurement covering a delay range of 1200 fs, the analysis of the wave–packet dynamics revealed two characteristic time scales, a classical oscillation time of $T_{\mathrm{cl}} = 26.1 \pm 1$ fs and a revival time $T_{\mathrm{rev}} = 305 \pm 5$ fs. Both values were in excellent agreement with a simulation where the superposition of beating vibrational levels was considered.

The particularly "broad" spectral profile of the HHG–XUV light was used to resonantly populate repulsive, doubly–excited H_2 states of the Q_1 and Q_2 series. Energetically, these states lie above the ionization threshold which gives rise to an autoionization process where one electron is emitted and the other is transferred to a lower electronic state in H_2^+. Doubly–excited states play an important role in the dissociative ionization of H_2 as intermediate transition states since the autoionization happens on the same time scale as the repulsion of the nuclei. Here, it could be shown that this fast autoionization of the doubly–excited states induced an oscillating asymmetry in the emission direction of correlated free and bound electrons. However, since the bound electron is confined in the neutral H atom, it cannot be measured with the reaction microscope and only the coincident detection of charged H^+ and e^- reveals the asymmetry. This form of ion–electron localization was studied for parallel and perpendicular transitions, allowing to distinguish between different origins of the asymmetry. In the first case, where the molecular and the light–polarization axes were parallel with respect to each other, the asymmetry corresponded to an interference of a direct ionization pathway via the $(1s\sigma_u)$ state and an indirect trajectory which includes the population of $Q_1(\Sigma_u^+)$ series, autoionizing to the $(1s\sigma_g)$ level. A semi–classical simulation of the XUV photon–induced dissociative ionization in parallel transitions perfectly reproduced the asymmetry profile in the correlated ion–electron energy spectrum. For the perpendicular case, the localization was obtained from interfering pathways, both resulting from a doubly–excited $Q_2(\Pi_u)$ state. Here, the asymmetry was expected and consequently only measured for electrons with a kinetic energy of ~ 7 eV as the autoionization to either the $(1s\sigma_g)$ or $(1s\sigma_u)$ states led to identical energies of the particles. In summary, all of these channels were identified by the energy distribution of coincident charged particles and, in addition, by the angular distributions of the emitted electrons which can be considered as a fingerprint of involved electron transitions.

The last section of the experimental results reported on the probing of doubly–excited states with delayed IR pulses. Even though the measured effects were small they allowed several important conclusions to be drawn. In parallel transitions, for instance, the IR coupled populated Q_1 levels with (Σ_u^+) symmetry with $Q_1(\Sigma_g^+)$ states which are not accessible in a dipole–allowed single–XUV photon absorption. The $Q_1(\Sigma_g^+)$ states autoionized fast due to their short lifetime and provided additional peaks, so–called sidebands, in the total kinetic energy spectrum of the charged fragments. To the authors' knowledge, this direct observation of the autoionization of $Q_1(\Sigma_g^+)$ states has been achieved for the first

time. A different IR–delay dependence was measured for perpendicular transitions. Here, long–living $Q_1(\Pi_u)$ states were populated by single XUV photons; however, as they feature a long life–time, a considerable contribution led to neutral dissociation. An additional IR field non–resonantly ionized these molecules by promoting them onto the $(1s\sigma_u)$ level, thus generating nuclei with a high KER and low–energetic electrons.

The conducted experiments on the double excitation of H_2 molecules revealed interesting processes not only for the single XUV–photon absorption but also for XUV–IR delay–dependent studies. Nevertheless, it should be the aim in future experiments on molecular hydrogen, to improve a few technical and operational aspects in the setup. Some suggestions shall be given in this summary, starting with some experimental ideas:

- Here, the wave–packet dynamics was observed in a 1200 fs delay range. An option to extend the resolution towards rotational states could be established by increasing the delay range to the maximum possible traverse path of 3 mm, corresponding to 10 ps. In such a measurement it would be possible to visualize ro–vibrational dynamics from the nuclear–wave packet time evolution. Of course, these settings are accompanied by extremely long recording times, but the laser system is capable of generating a stable high–harmonic yield for more than 150 hours.

- The implemented measurements on doubly–excited states revealed fast dynamics for parallel transitions which occur during the temporal overlap region of the pulses. Therefore, a smaller delay range should be chosen in order to resolve temporal oscillations of the sideband structures in the corresponding energy range, as expected in [SRM12]. Accordingly, the delay range has to be reduced to approximately $5 - 10$ fs.

- The same measurement can be analyzed in view of IR–induced asymmetry effects as they are observed in [San+12]; however, the results can be extended to the full energy range of correlated ions and electrons and distinguished for different molecular orientations.

- In contrast, the pulse delay settings for perpendicular transitions have to be much larger, as the autoionization via Q_1 doubly–excited states with Π_u symmetry exhibit long autoionization times. In order to probe and observe this, it is recommended to choose a delay range of at least 150 fs.

- Rest gas, in particular water molecules that are photo–fragmentized into OH^+ and single protons produce a considerable background signal on top of the interesting events, especially for the perpendicular case. A convenient avoiding could be established by the application of a D_2 gas jet in the reaction microscope. However, in order to study time–dependent autoionization in parallel transitions, H_2 represents a more rational target, as the core movement during fragmentation is much faster at comparable autoionization times. As a consequence, the autoionizing events are

rather distinguishable from direct dissociation by the kinetic energy of the ions. In summary, H_2 is should be the target for studies of parallel transitions, whereas D_2 is considerable for perpendicular transitions.

In addition to the experimental ideas on XUV–pump IR–probe measurements on molecular hydrogen there are other possibilities to exploit the advantages of the laser and detection system, involving high photon energies, short pulse durations, high degree of coherence and fully differential spectra. These include a decay study of doubly–excited states in homo– and heteronuclear molecules [Luc+12] as well as pump–pump–probe schemes with one XUV and two IR–pulses [NTM12].

Any experimental setup features some limitations and problems which also applies to the present setup and in particular to the HHG beamline. Regarding the discussed experiments and the quality of the results, there are several conceptions for technical modifications in order to improve the current settings and to enable more insight into the dynamics of doubly–excited states in H_2 as well as into electron–electron correlations in other gaseous species.

For example, the spatial overlap of the XUV and IR laser has not been optimal, even if the delay–dependent results on the wave–packet dynamics suggested the contrary. As the XUV–light generation and focusing are difficult tasks, it is reasonable for future experiments to revise the IR beam in focal size and position within the reaction volume.

Moreover, measurements with this setup usually proceed for several tens of hours, since they are based on an event–by–event recording with a detection rate of approximately 1500 Hz. Over such long measuring times it is difficult to maintain the interferometric stability in terms of sub–cycle resolution. Besides a rather difficult implementation of an additional, co–propagating HeNe laser beam, providing an interferometric reference signal, there are two other options to overcome these obstacles. A simple solution would be given in agreement to an improved XUV–IR overlap in the reaction volume. Then, the simultaneous detection of 2 % H^+ and 98 % H_2^+ ions could reveal sideband oscillations in H_2^+ within the temporal overlap region. A temporal drift of such oscillating signals in H_2^+ can be compensated in a post analysis, and applied to the H^+ events, revealing all delay dependences in doubly–excited states for parallel transitions. Recently, the necessary sideband oscillations in H_2^+ and D_2^+ molecules were presented in [Kel+11] and there exist examples for other molecular species, such as for N_2 in [Hae+09] and O_2 (not yet published [Lei11]). Another possibility would be to check the interferometric stability throughout the measurement by periodically performing IR–IR autocorrelations in the reaction microscope for one traverse path. During that time, the XUV pulses have to be blocked, whereas the blocking of the XUV–generating IR beam has to be abrogated. The required implementation is not difficult as the aluminum filter has to be replaced with a anti–reflex coated, 2 µm pellicle, which simply spoken has the opposite filtering properties. Such an operation has to be automized in order to be applicable for long measurement times.

7 Appendix

Atomic units

In atomic physics literature it is common to express dimensions in atomic units. Referring to typical scales in the hydrogen molecule they are defined by setting 4 fundamental constants to unity. These are the electron mass m_e, the elementary charge e as well as the Planck constant $\hbar$ and the Coulomb force constant $1/(4\pi\epsilon_0)$. The speed of light however is not equal to one but instead transforms into $1/\alpha = 137$. The following table [7.1] represents some basic dimensions in atomic units together with the corresponding quantity in the metric SI system and gives associated expressions.

Dimension	Symbol	1 au Metric SI equivalent	Information and expressions
Charge	Q	$1\,\text{au} = 1.6022 \cdot 10^{-19}\,\text{C}$	Elementary charge e
Mass	m	$1\,\text{au} = 9.1095 \cdot 10^{-31}\,\text{kg}$	e^- mass m_e
Time	t	$1\,\text{au} = 24.189 \cdot 10^{-18}\,\text{s}$	$\hbar/E_H$
Length	r	$1\,\text{au} = 5.2918 \cdot 10^{-11}\,\text{m}$	e^- ground state Bohr–radius a_0
Velocity	v	$1\,\text{au} = 2.1877 \cdot 10^{-6}\,\text{m/s}$	αc
Energy	E	$1\,\text{au} = 4.3597 \cdot 10^{-18}\,J$	Hartree energy ($E_H = 27.211\,\text{eV}$)
Momentum	p	$1\,\text{au} = 1.9929 \cdot 10^{-24}\,\text{kg m/s}$	$\sqrt{E_H m_e}$
Ang. mom.	L	$1\,\text{au} = 1.0546 \cdot 10^{-34}\,\text{Js}$	Reduced Planck constant $\hbar$
Elec. field	E	$1\,\text{au} = 5.1421 \cdot 10^{11}\,\text{V/m}$	$E_H/(ea_0)$
Intensity	I	$1\,\text{au} = 6.4364 \cdot 10^{15}\,\text{W/cm}^2$	$E_H^2/(\hbar a_0^2)$

Table 7.1: Atomic units related to their metric SI values. In the right column some common expression are given to calculate the quantities.

State notation in H_2 and H_2^+

In Table 7.2 several relevant molecular states of H_2 and H_2^+ are listed. These comprise the H_2 and H_2^+ ground states, as well as several singly–excited and doubly–excited states. The notation is given for single electrons and the complete molecular orbitals. Note, all listed states except of the ground states of H_2 and H_2^+ are not stable and lead to a dissociation into specified fragments. For doubly excited states the probability that autoionization occurs is high; nevertheless, only neutral fragments are listed here.

Molecule	Molecular states	e^- states	Dissociation product
H_2	$X\,^1\Sigma_g^+$	$1s\sigma_g$, $1s\sigma_g$	
H_2^{**} Q_1	$^1\Sigma_u^+(1)$	$1s\sigma_u$, $2s\sigma_g$	$H(1s\sigma) + H^*(2p\sigma)$
	$^1\Pi_u(1)$	$1s\sigma_u$, $3d\pi_g$	$H(1s\sigma) + H^*(2p\pi)$
	$^1\Sigma_u^+(2)$	$1s\sigma_u$, $3s\sigma_g$	$H(1s\sigma) + H^*(2s\sigma)$
	$^1\Sigma_u^+(3)$	$1s\sigma_u$, $4s\sigma_g$	$H(1s\sigma) + H^*(3s\sigma)$
	$^1\Sigma_u^+(4)$	$1s\sigma_u$, $4d\sigma_g$	$H(1s\sigma) + H^*(3s\sigma)$
H_2^{**} Q_2	$^1\Pi_u(1)$	$2p\pi_u$, $2s\sigma_g$	$H^*(2p\pi) + H^*(2s\sigma)$
	$^1\Pi_u(2)$	$2p\pi_u$, $3s\sigma_g$	$H^*(2p\pi) + H^*(2p\sigma)$
	$^1\Pi_u(3)$	$2p\pi_u$, $3d\sigma_g$	$H^*(2p\pi) + H^*(3l\sigma)$
	$^1\Pi_u(4)$	$2p\pi_u$, $4s\sigma_g$	$H^*(2p\pi) + H^*(3l\sigma)$
	$^1\Pi_u(5)$	$2p\pi_u$, $4d\sigma_g$	$H^*(2p\pi) + H^*(3l\sigma)$
H_2^+	$^2\Sigma_g^+$	$1s\sigma_g$	
	$^2\Sigma_u^+$	$1s\sigma_u$ $(= 2p\sigma_u)$	$H(1s\sigma) + H^+$
	$^2\Pi_u$	$2p\pi_u$	$H^*(2p\pi) + H^+$
	$^2\Pi_u$	$2s\sigma_g$	$H^*(2s\sigma) + H^+$
	$^2\Pi_u$	$3d\sigma_g$	$H^*(3d\sigma) + H^+$

Table 7.2: Molecular and electronic representation of experimental relevant states. Note that dissociation channels after autionization of H_2^{**} are not shown. Furthermore, higher doubly–excited states $Q_{n>2}$ are not listed.

Dipole–allowed transitions in H_2 and H_2^+

In Table 7.3, possible bound–bound single–photon transitions between two states of different symmetries are listed. In particular the first line represents possible transitions form the ground state of H_2 to doubly excited Q_1 and Q_2 states. Note, such considerations are also important for single–IR photon transitions between two H_2^+ levels, such as $(1s\sigma_g)$ and $(1s\sigma_u)$. $P_\parallel$ and $P_\perp$ denote parallel and perpendicular transitions, respectively.

	Σ_g^+	Σ_g^-	Σ_u^+	Σ_u^-	Π_g	Π_u
Σ_g^+	/	/	$P_\parallel$	/	/	$P_\perp$
Σ_g^-		/	/	$P_\parallel$	/	$P_\perp$
Σ_u^+			/	/	$P_\perp$	/
Σ_u^-				/	$P_\perp$	/
Π_g					/	$P_\parallel$
Π_u						/

Table 7.3: Possible single photon–induced parallel and perpendicular transitions are listed. Dipole–forbidden transition are not indicated.

Table 7.4 illustrates a few simple calculation rules for molecular symmetries which must be considered for dipole–allowed transitions.

$\Lambda \otimes \Lambda$	$g, u \otimes g, u$	$+, - \otimes +, -$
$\Sigma \otimes \Sigma = \Sigma$	$g \otimes g = g$	$+ \otimes + = +$
$\Sigma \otimes \Pi = \Pi$	$g \otimes u = u$	$+ \otimes - = -$
$\Pi \otimes \Pi = \Sigma^{+-}, \Delta$	$u \otimes u = g$	$- \otimes - = +$

Table 7.4: Changes of total angular momentum component Λ, g, u and $+, -$ symmetries in a single photon–induced dipole–allowed transition.

Autoionization times of selected doubly excited H_2^{**} states

Autoionization times τ_{AI} of the H_2^{**} states as a function of the internuclear distance are shown in Figure 7.1 for the Q_1 and Q_2 series. Here, only the lowest energetic state and $(^1\Sigma_g^+)$, $(^1\Sigma_u^+)$, $(^1\Pi_g)$ and $(^1\Pi_u)$ symmetries are considered. In Figure 7.1 (c) and (d) the autoionization times are shown for the doubly excited states that are mostly relevant in parallel and perpendicular transitions. Note, all curves are adapted from [SM97; SM99b].

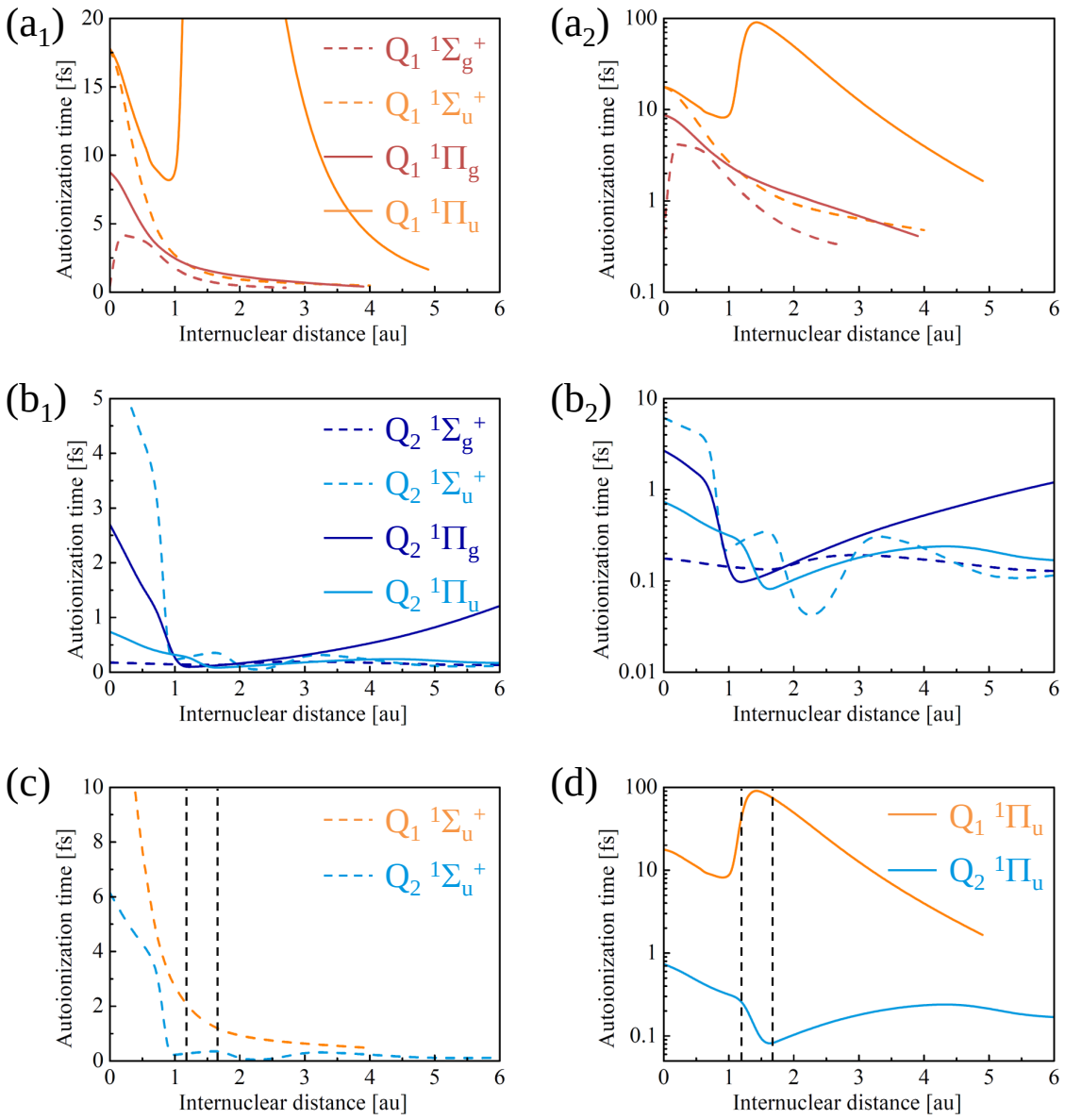

Figure 7.1: Autoionization times τ_{AI} of the H_2^{**} states as a fuction of the internuclear distance. (a_1) linear and (a_2) logarithmic plot of τ_{AI} for the first Q_1 states of $(^1\Sigma_g^+)$, $(^1\Sigma_u^+)$, $(^1\Pi_g)$, $(^1\Pi_u)$ symmetry. (b_1) linear and (b_2) logarithmic plot of τ_{AI} for the first Q_2 states of $(^1\Sigma_g^+)$, $(^1\Sigma_u^+)$, $(^1\Pi_g)$, $(^1\Pi_u)$ symmetry. (c) τ_{AI} of Q_1 and Q_2 $(^1\Sigma_u^+)$ states, relevant for parallel transition with single–XUV photons. (d) τ_{AI} of Q_1 and Q_2 $(^1\Pi_u)$ states, relevant for perpendicular transition with single–XUV photons. The dashed–black lines denote the Franck–Condon region in H_2.

Bibliography

[ADK86] M. V. Ammosov, N. B. Delone, and V. P. Krainov. "Tunnel ionization of complex atoms and of atomic ions in an alternating electromagnetic field". In: *Soviet Physics - JETP* 64.6 (1986), pp. 1191–1194.

[AF05] P. Atkins and R. Friedman. *Molecular Quantum Mechanics*. 4th. Oxford: Oxford University Press, 2005.

[Ago+79] P. Agostini et al. "Free-Free Transitions Following Six-Photon Ionization of Xenon Atoms". In: *Physical Review Letters* 42.17 (Apr. 1979), pp. 1127–1130.

[Agr01] G. P. Agrawal. *Nonlinear Fiber Optics*. 3rd ed. Academic Press, 2001.

[ALL96] Philippe Antoine, Anne L'Huillier, and Maciej Lewenstein. "Attosecond Pulse Trains Using High Order Harmonics". In: *Physical Review Letters* 77.7 (1996), pp. 1234–1237.

[Aln+05] A. S. Alnaser et al. "Simultaneous real-time tracking of wave packets evolving on two different potential curves in H_2^+ and D_2^+". In: *Physical Review A* 72.3 (Sept. 2005), pp. 30–702.

[And+95] M. H. Anderson et al. "Observation of Bose-Einstein Condensation in a Dilute Atomic Vapor". en. In: *Science* 269.5221 (July 1995), pp. 198–201.

[Bak+06] S. Baker et al. "Probing Proton Dynamics in Molecules on an Attosecond Time Scale". In: *Science* 312.5772 (Apr. 2006), pp. 424–427.

[Bal+97] Andrius Baltuska et al. "Optical pulse compression to 5 fs at a 1-MHz repetition rate". In: *Optics Letters* 22.2 (Jan. 1997), pp. 102–104.

[BD74] C. Bottcher and K. Docken. "Autoionizing states of the hydrogen molecule". In: *Journal of Physics B: Atomic and Molecular Physics* 7.1 (Jan. 1974), pp. L5–L8.

[Bel+98] M. Bellini et al. "Temporal Coherence of Ultrashort High-Order Harmonic Pulses". In: *Physical Review Letters* 81.2 (July 1998), pp. 297–300.

[BF73] R. Browning and J. Fryar. "Dissociative photoionization of H_2 and D_2 through the $1s\sigma_g$ ionic state". In: *Journal of Physics B: Atomic and Molecular Physics* 6.2 (Feb. 1973), pp. 364–371.

[BH00] M Bellini and T W Hänsch. "Phase-locked white-light continuum pulses: toward a universal optical frequency-comb synthesizer". In: *Optics letters* 25.14 (July 2000). PMID: 18064269, pp. 1049–1051.

[BHP70] Charles L. Beckel, Bertle D. Hansen, and James M. Peek. "Theoretical Study of H_2^+ Ground Electronic State Spectroscopic Properties". In: *The Journal of Chemical Physics* 53.9 (Nov. 1970), pp. 3681–3690.

[BO27] M. Born and R. Oppenheimer. "Zur Quantentheorie der Moleküle". en. In: *Annalen der Physik* 389.20 (1927), p. 457.

[Bor+96] C. Bordas et al. "Photoelectron imaging spectrometry: Principle and inversion method". In: *Review of Scientific Instruments* 67.6 (June 1996), pp. 2257 – 2268.

[Buc+90] P. H. Bucksbaum et al. "Softening of the H_2^+ molecular bond in intense laser fields". In: *Physical Review Letters* 64.16 (Apr. 1990), pp. 1883–1886.

[CC10] Zenghu Chang and P. Corkum. "Attosecond photon sources: the first decade and beyond [Invited]". In: *Journal of the Optical Society of America B* 27.11 (Oct. 2010), B9.

[Cha11] Z. Chang. *Fundamentals of Attosecond Optics*. 1st. Taylor and Francis Group, LLC, 2011.

[Chi04] S. L. Chin. "Advances in Multi-Photon Processes and Spectroscopy". In: ed. by S. H. Lin, A. A. Villaeys, and Y. Fujimura. World Scientific, 2004. Chap. From Multphoton to Tunnel Ionization, pp. 249–271.

[Chu+93] Y. M. Chung et al. "Dissociative photoionization of H_2 from 18 to 124 eV". In: *The Journal of Chemical Physics* 99.2 (July 1993), pp. 885–889.

[Coh95] L. Cohen. *Time-frequency Analysis, Theory and Applications*. Prentice-Hall signal processing series, 1995.

[Cor93] P. B. Corkum. "Plasma perspective on strong field multiphoton ionization". In: *Physical Review Letters* 71.13 (1993), pp. 1994–1997.

[Cör12] Philipp Cörlin. "Laser induced Coulomb–explosion of allene molecules: Experiment and simulation". Diplomarbeit. Ruprecht-Karls-Universität Heidelberg, 2012.

[Dac+09] H Dachraoui et al. "Interplay between absorption, dispersion and refraction in high-order harmonic generation". In: *Journal of Physics B: Atomic, Molecular and Optical Physics* 42.17 (Sept. 2009), p. 175402.

[DD78] J. L. Dehmer and Dan Dill. "Photoion angular distributions in dissociative photoionization of H_2 at 304 Angstrom". In: *Physical Review A* 18.1 (July 1978), pp. 164–171.

[Dem95] Wolfgang Demtröder. *Experimentalphysik 3 – Atome, Moleküle und Festkörper*. 1st. Springer-Verlag, 1995.

[DK91] N. B. Delone and V. P. Krainov. "Energy and angular electron spectra for the tunnel ionization of atoms by strong low-frequency radiation". In: *J. Opt. Soc. Am. B* 8.6 (1991), pp. 1207–1211.

[DK99] N. B. Delone and V. P. Krainov. *Multiphoton Processes in Atoms*. 2nd edition. Springer series on atoms and plasmas. Springer, 1999.

[DR06] J. C. Diehls and W. Rudolph. *Ultrashort Laser Pulse Phenomena*. 2st. Elsevier, 2006.

[Dre+01] Markus Drescher et al. "X-ray Pulses Approaching the Attosecond Frontier". In: *Science* 291 (2001), pp. 1923–1927.

[Eng96] F. Engelke. *Aufbau der Moleküle*. 3rd. Teubner Studienbuecher Chemie, 1996.

[EP97] André T. J. B. Eppink and David H. Parker. "Velocity map imaging of ions and electrons using electrostatic lenses: Application in photoelectron and photofragment ion imaging of molecular oxygen". In: *Review of Scientific Instruments* 68.9 (Sept. 1997), pp. 3477–3484.

[Erg+05] Th. Ergler et al. "Time-Resolved Imaging and Manipulation of H_2 Fragmentation in Intense Laser Fields". In: *Physical Review Letters* 95.9 (Aug. 2005), p. 093001.

[Erg+06a] Th. Ergler et al. "Quantum-Phase Resolved Mapping of Ground State Vibrational D_2 Wave Packets via Selective Depletion in Intense Laser Pulses". In: *Physical Review Letters* 97.10 (Sept. 2006), p. 103004.

[Erg+06b] Th. Ergler et al. "Spatiotemporal Imaging of Ultrafast Molecular Motion: Collapse and Revival of the D_2^+ Nuclear Wave Packet". In: *Physical Review Letters* 97.19 (Nov. 2006), p. 193001.

[Erg+06c] Th. Ergler et al. "Ultrafast mapping of $H_2^+(D_2^+)$ nuclear wave packets using time resolved Coulomb explosion imaging". In: *Journal of Physics B: Atomic, Molecular and Optical Physics* 39.13 (July 2006), S493–S501.

[Fan61] U. Fano. "Effects of Configuration Interaction on Intensities and Phase Shifts". In: *Phys. Rev.* 124 (6 1961), pp. 1866–1878.

[Fem] *Kaladeidoscope Hollow Fiber Compressor*. URL: `http://www.femtolasers.com/uploads/tx_npproductmatrix/KALEIDOSCOPE.pdf`.

[Fer+88] M. Ferray et al. "Multiple-harmonic conversion of 1064 nm radiation in rare gases". In: *Journal of Physics B: Atomic, Molecular and Optical Physics* 21.3 (Feb. 1988), pp. L31–L35.

[Fes62] Herman Feshbach. "A unified theory of nuclear reactions. II". In: *Annals of Physics* 19.2 (Aug. 1962), pp. 287–313.

[Feu+07] B. Feuerstein et al. "Complete Characterization of Molecular Dynamics in Ultrashort Laser Fields". In: *Physical Review Letters* 99.15 (Oct. 2007), p. 153002.

[Fis+10] Bettina Fischer et al. "Steering the Electron in H_2^+ by Nuclear Wave Packet Dynamics". In: *Physical Review Letters* 105.22 (Nov. 2010), p. 223001.

[Fis03] D. Fischer. "Mehr-Teilchen-Dynamik in der Einfach- und Doppelionisation von Helium durch geladene Projektile". PhD thesis. Ruprecht-Karls-Universität Heidelberg, 2003.

[Fis10] Andreas Fischer. "Erzeugung und Dispersionskontrolle von Femtosekundenlaserimpulsen". Diplomarbeit. Ruprecht-Karls-Universität Heidelberg, 2010.

[Fis12] Andreas Fischer. Private communication. Heidelberg, 2012.

[FM01] J. Fernández and F. Martín. "Autoionizing $^1\Sigma_u^+$ and $^1\Pi_u$ states of H_2 above the third and fourth ionization thresholds". In: *Journal of Physics B: Atomic, Molecular and Optical Physics* 34.21 (Nov. 2001), pp. 4141–4153.

[FM09] Jorge Fernández and Fernando Martín. "Electron and ion angular distributions in resonant dissociative photoionization of H_2 and D_2 using linearly polarized light". In: *New Journal of Physics* 11.4 (Apr. 2009), p. 043020.

[For+87] R. L. Fork et al. "Compression of optical pulses to six femtoseconds by using cubic phase compensation". In: *Optics Letters* 12.7 (July 1987), pp. 483–485.

[FT03] Bernold Feuerstein and Uwe Thumm. "Fragmentation of H_2^+ in strong 800 nm laser pulses Initial vibrational state dependence". In: *Physical Review A* 67.4 (Apr. 2003), p. 043405.

[Gar+06] E. Melero Garcia et al. "Fluorescence study of doubly excited states of molecular hydrogen". In: *Journal of Physics B: Atomic, Molecular and Optical Physics* 39.2 (Jan. 2006), pp. 205–213.

[GC+12] A. González-Castrillo et al. "Reproducibility of observables and coherent control in molecular photoionization: from continuous wave to ultrashort pulsed radiation". In: *The journal of physical chemistry. A* 116.11 (Mar. 2012). PMID: 22103857, pp. 2704–2712.

[GCK12] Lukas Gallmann, Claudio Cirelli, and Ursula Keller. "Attosecond science: recent highlights and future trends". In: *Annual review of physical chemistry* 63 (2012). PMID: 22404594, pp. 447–469.

[Gil+10] Steve Gilbertson et al. "Isolated Attosecond Pulse Generation without the Need to Stabilize the Carrier-Envelope Phase of Driving Lasers". In: *Physical Review Letters* 105.9 (Aug. 2010), p. 093902.

[Glo+96] T. E. Glover et al. "Observation of Laser Assisted Photoelectric Effect and Femtosecond High Order Harmonic Radiation". In: *Physical Review Letters* 76.14 (Apr. 1996), pp. 2468–2471.

[GM+10] M. Glass-Maujean et al. "Competing decay channel fluorescence, dissociation, and ionization in superexcited levels of H_2". In: *Physical Review A* 82.6 (Dec. 2010), p. 062511.

[GMS05] M. Glass-Maujean and H. Schmoranzer. "Dissociation dynamics of doubly excited states of molecular hydrogen". In: *Journal of Physics B: Atomic, Molecular and Optical Physics* 38.8 (Apr. 2005), pp. 1093–1105.

[Gol+97] A. V. Golovin et al. "Observation of Site Specific Electron Emission in the Decay of Superexcited O_2". In: *Physical Review Letters* 79.23 (Dec. 1997), pp. 4554–4557.

[Gop09] R. Gopal. "Electron Wave Packet Interferences in Ionization with Few-Cycle Laser Pulses and the Dissociative Photoionization of D_2 with Ultrashort Extreme Ultraviolet Pulses". PhD thesis. Ruprecht-Karls-Universität Heidelberg, 2009.

[Gri05] R. Grinter. *The Quantum in Chemistry: An Experimentalist´s view*. West Sussex: John Wiley & Sons, 2005.

[GS+95] A Giusti-Suzor et al. "Dynamics of H_2^+ in intense laser fields". In: *Journal of Physics B: Atomic, Molecular and Optical Physics* 28.3 (Feb. 1995), pp. 309–339.

[GZT54] J. P. Gordon, H. J. Zeiger, and C. H. Townes. "Molecular Microwave Oscillator and New Hyperfine Structure in the Microwave Spectrum of NH_3". In: *Physical Review* 95.1 (July 1954), pp. 282–284.

[Hae+09] S. Haessler et al. "Phase-resolved attosecond near-threshold photoionization of molecular nitrogen". In: *Physical Review A* 80.1 (July 2009), p. 011404.

[HCS09] S. X. Hu, L. A. Collins, and B. I. Schneider. "Attosecond photoelectron microscopy of H_2^+". In: *Physical Review A* 80.2 (2009), p. 023426.

[HE02] Y. Hikosaka and J.H.D. Eland. "Molecular frame photoelectron angular distributions in photoionization of H_2 into the $H_2^+(n = 2)$ states". In: *Chemical Physics* 277.1 (2002), pp. 53 –59.

[Hen+01] M. Hentschel et al. "Attosecond metrology". In: *Nature* 414.6863 (Nov. 2001). PMID: 11734845, pp. 509–513.

[HG05] C. E. Housecroft and Sharpe A. G. *Inorganic Chemistry*. 2th. Essex: Pearson Education Limited, 2005.

[His61] John R. Hiskes. "Dissociation of Molecular Ions by Electric and Magnetic Fields". In: *Physical Review* 122.4 (May 1961), pp. 1207–1217.

[HL27] W. Heitler and F. London. "Wechselwirkung neutraler Atome und homöopolare Bindung nach der Quantenmechanik". In: *Zeitschrift für Physik* 44 (1927), p. 455.

[HMH93] S.E. Harris, J.J. Macklin, and T.W. Hänsch. "Atomic scale temporal structure inherent to high order harmonic generation". In: *Optics Communications* 100 (July 1993), pp. 487–490.

[Hou] J. T. Hougen. *The Calculation of Rotational Energy Levels and Rotational Line Intensities in Diatomic Molecules*. URL: `http://www.nist.gov/pml/pubs/mono115/index.cfm`.

[HS10] I. V. Hertel and C. P. Schulz. *Atome, Moleküele und optische Physik 2 – Moleküle und Photonen - Spektroskopie und Streuphysik*. 1st. Springer-Verlag, 2010.

[HT10] Feng He and Uwe Thumm. "Dissociative ionization of H_2 in an attosecond pulse train and delayed laser pulse". In: *Physical Review A* 81.5 (May 2010), p. 053413.

[HW05] H. Haken and H. C. Wolf. *Molekülphysik und Quantenchemie*. 5th. Springer-Verlag, 2005.

[Hzb] *Seeded Free Electron Lasers*. URL: `https://www.helmholtz-berlin.de/forschung/grossgeraete/beschleunigerphysik/free-electron-lasers/index_de.html`.

[IDC92] F. A. Ilkov, J. E. Decker, and S. L. Chin. "Ionization of atoms in the tunnelling regime with experimental evidence using Hg atoms". In: *Journal of Physics B: Atomic, Molecular and Optical Physics* 25.19 (Oct. 1992), pp. 4005–4020.

[IHU96] Kenji Ito, Richard I. Hall, and Masatoshi Ukai. "Dissociative photoionization of H_2 and D_2 in the energy region of 25 to 45 eV". In: *The Journal of Chemical Physics* 104.21 (June 1996), pp. 8449–8457.

[Jag+02] O. Jagutzki et al. "A broad application microchannel plate detector system for advanced particle or photon detection tasks, large area imaging, precise multi hit timing information and high detection rate". In: *Nuclear Instruments and Methods in Physics Research Section A: Accelerators, Spectrometers, Detectors and Associated Equipment* 477.1 (Jan. 2002), pp. 244–249.

[Jes+04] V.L.B. de Jesus et al. "Reaction microscopes applied to study atomic and molecular fragmentation in intense laser fields: non–sequential double ionization of helium". In: *Journal of Electron Spectroscopy and Related Phenomena* 141 (Dec. 2004), pp. 127–142.

[Jia+10] Y. H. Jiang et al. "Investigating two-photon double ionization of D_2 by XUV pump XUV probe experiments". In: *Physical Review A* 81.5 (May 2010), p. 051402.

[KB48] P. Kirkpatrick and A. V. Baez. "Formation of Optical Images by X-Rays". In: *Journal of the Optical Society of America* 38 (1948), pp. 766–773.

[Kel+09] F. Kelkensberg et al. "Molecular dissociative ionization and wave-packet dynamics studied using two-color XUV and IR pump-probe spectroscopy". In: *Physical Review Letters* 103.12 (Sept. 2009). PMID: 19792432, p. 123005.

[Kel+11] F. Kelkensberg et al. "Attosecond Control in Photoionization of Hydrogen Molecules". In: *Physical Review Letters* 107.4 (July 2011), p. 043002.

[Kel65] L. V. Keldysh. "Ionization in the field of a strong electromagnetic wave". In: *Soviet Physics JETP* 20 (1965), p. 1307.

[KI09] Ferenc Krausz and Misha Ivanov. "Attosecond physics". In: *Reviews of Modern Physics* 81.1 (Feb. 2009), pp. 163–234.

[Kie+02] R. Kienberger et al. "Steering Attosecond Electron Wave Packets with Light". In: *Science* 297.5584 (Aug. 2002), pp. 1144–1148.

[Kli+06] M. F. Kling et al. "Control of Electron Localization in Molecular Dissociation". In: *Science* 312.5771 (Apr. 2006), pp. 246–248.

[Klü+11] K. Klünder et al. "Probing Single-Photon Ionization on the Attosecond Time Scale". In: *Physical Review Letters* 106.14 (Apr. 2011), p. 143002.

[Kob+98] Y. Kobayashi et al. "27-fs extreme ultraviolet pulse generation by high-order harmonics". In: *Optics Letters* 23.2 (1998), pp. 64–66.

[KR83] P Kruit and F H Read. "Magnetic field paralleliser for 2π electron-spectrometer and electron-image magnifier". In: *Journal of Physics E: Scientific Instruments* 16.4 (Apr. 1983), pp. 313–324.

[Kre+09] Manuel Kremer et al. "Electron Localization in Molecular Fragmentation of H_2 by Carrier-Envelope Phase Stabilized Laser Pulses". In: *Physical Review Letters* 103.21 (Nov. 2009), p. 213003.

[KS08] F. K. Kneubuehl and M. K. Sigrist. *Laser*. 7th. Vieweg + Teubner, 2008.

[KS89] K. C. Kulander and B. W. Shore. "Calculations of Multiple-Harmonic Conversion of 1064-nm Radiation in Xe". In: *Physical Review Letters* 62.5 (Jan. 1989), pp. 524–526.

[Laf+03] A. Lafosse et al. "Molecular frame photoelectron angular distributions in dissociative photoionization of H_2 in the region of the Q_1 and Q_2 doubly excited states". In: *Journal of Physics B: Atomic, Molecular and Optical Physics* 36.23 (Dec. 2003), pp. 4683–4702.

[Lat+93] C. J. Latimer et al. "A dissociative photoionization study of the autoionization lifetime of the lowest $^1\Sigma_u$ superexcited state in hydrogen and deuterium". In: *Journal of Physics B: Atomic, Molecular and Optical Physics* 26.18 (Sept. 1993), pp. L595–L600.

[Lat+95] C. J. Latimer et al. "Photoionization of hydrogen and deuterium". In: *The Journal of Chemical Physics* 102.2 (Jan. 1995), pp. 722–725.

[LB93] A. L'Huillier and Ph. Balcou. "High order harmonic generation in rare gases with a 1 ps 1053 nm laser". In: *Physical Review Letters* 70.6 (Feb. 1993), pp. 774–777.

[Lei07] Torsten Leitner. "High Order Harmonic Generation as a possible Seed Source for the BESSY Free Electron Laser". Diploma thesis. Humboldt–Universität zu Berlin, 2007.

[Lei11] Thorsten Leitner. Private communication. DPG conference in Dresden, 2011.

[Lew+94] M. Lewenstein et al. "Theory of high-harmonic generation by low-frequency laser fields". In: *Physical Review A* 49.3 (Mar. 1994), pp. 2117–2132.

[LM+05] Rodrigo López-Martens et al. "Amplitude and Phase Control of Attosecond Light Pulses". In: *Physical Review Letters* 94.3 (Jan. 2005), p. 033001.

[LSK91] A. L'Huillier, K. J. Schafer, and K. C. Kulander. "Higher order harmonic generation in xenon at 1064 nm: The role of phase matching". In: *Physical Review Letters* 66.17 (Apr. 1991), pp. 2200–2203.

[LTM06] C. D. Lin, X. M. Tong, and Toru Morishita. "Direct experimental visualization of atomic and electron dynamics with attosecond pulses". In: *Journal of Physics B: Atomic, Molecular and Optical Physics* 39.13 (July 2006), S419–S426.

[Luc+02] R. R. Lucchese et al. "Polar and azimuthal dependence of the molecular frame photoelectron angular distributions of spatially oriented linear molecules". In: *Physical Review A* 65.2 (Jan. 2002), p. 020702.

[Luc+12] M. Lucchini et al. "Autoionization and ultrafast relaxation dynamics of highly excited states in N_2". In: *Physical Review A* 86.4 (Oct. 2012), p. 043404.

[Mai+03] Y. Mairesse et al. "Attosecond Synchronization of High-Harmonic Soft X-Rays". In: *Science* 302.5650 (Nov. 2003), pp. 1540–1543.

[Mai60] T. H. Maiman. "Stimulated Optical Radiation in Ruby". In: *, Published online: 06 August 1960; | doi:10.1038/187493a0* 187.4736 (Aug. 1960), pp. 493–494.

[Mar+07] F. Martín et al. "Single Photon-Induced Symmetry Breaking of H_2 Dissociation". In: *Science* 315.5812 (Feb. 2007), pp. 629–633.

[Mar99] Fernando Martín. "Ionization and dissociation using B splines: photoionization of the hydrogen molecule". In: *Journal of Physics B: Atomic, Molecular and Optical Physics* 32.16 (Aug. 1999), R197–R231.

[Mas+08] Hiroki Mashiko et al. "Double Optical Gating of High-Order Harmonic Generation with Carrier-Envelope Phase Stabilized Lasers". In: *Physical Review Letters* 100.10 (Mar. 2008), p. 103906.

[Mau+04] J. Mauritsson et al. "Measurement and control of the frequency chirp rate of high-order harmonic pulses". In: *Physical Review A* 70.2 (2004), p. 021801.

[Mau+08] J. Mauritsson et al. "Coherent Electron Scattering Captured by an Attosecond Quantum Stroboscope". In: *Physical Review Letters* 100.7 (Feb. 2008), p. 073003.

[McP+87] A. McPherson et al. "Studies of multiphoton production of vacuum-ultraviolet radiation in the rare gases". In: *Physical Review Letters* 4.4 (Apr. 1987), p. 595.

[ME11] Heinz Mustroph and Steffen Ernst. "Das Franck Condon Prinzip". In: *Chemie in unserer Zeit* 45.4 (2011), pp. 256–269.

[Mec+08] M. Meckel et al. "Laser-Induced Electron Tunneling and Diffraction". In: *Science* 320.5882 (June 2008), pp. 1478–1482.

[MFK03] R. Moshammer, D. Fischer, and H. Kollmus. "Many-Particle Quantum Dynamics in Atomic and Molecular Fragmentation". In: ed. by J. Ullrich and V. P. Shevelko. Heidelberg: Springer, 2003. Chap. Recoil Ion Momentum Spectroscopy and Reaction Microscopes, pp. 33–58.

[Mil88] D. R. Miller. *Atomic and Molecular Beam Methods*. Singapore: Oxford University Press, 1988. Chap. Free Jet Sourcess.

[MQ05] Y. Mairesse and F. Quéré. "Frequency-resolved optical gating for complete reconstruction of attosecond bursts". In: *Physical Review A* 71.1 (Jan. 2005), p. 011401.

[MS64] E. A. J. Marcatili and R. A. Schmeltzer. "Hollow Metallic and Dielectric Waveguides for Long Distance Optical Transmission and Lasers". In: *Bell Syst. Tech. J.* 4 (1964), p. 1783.

[Mul75] Robert S. Mulliken. *Selected Papers of Robert S. Mulliken*. en. University of Chicago Press, Aug. 1975.

[Nis+02] M. Nisoli et al. "High-Brightness High-Order Harmonic Generation by Truncated Bessel Beams in the Sub-10-fs Regime". In: *Physical Review Letters* 88.3 (Jan. 2002), p. 033902.

[Nis+97a] M. Nisoli et al. "A novel-high energy pulse compression system: generation of multigigawatt sub-5-fs pulses". In: *Applied Physics B: Lasers and Optics* 65.2 (1997), pp. 189–196.

[Nis+97b] M. Nisoli et al. "Compression of high-energy laser pulses below 5 fs". In: *Optics Letters* 22.8 (Apr. 1997), pp. 522–524.

[NS09] M. Nisoli and G. Sansone. "New frontiers in attosecond science". In: *Progress in Quantum Electronics* 33.1 (Jan. 2009), pp. 17–59.

[NTM12] Thomas Niederhausen, Uwe Thumm, and Fernando Martín. "Laser-controlled vibrational heating and cooling of oriented H_2^+ molecules". In: *Journal of Physics B: Atomic, Molecular and Optical Physics* 45.10 (May 2012), p. 105602.

[Pau+01] P. M. Paul et al. "Observation of a Train of Attosecond Pulses from High Harmonic Generation". In: *Science* 292.5522 (Jan. 2001), pp. 1689–1692.

[Pfl08] T. Pflüger. "Electron impact single sonization of small argon clusters". Diplomarbeit. Ruprecht-Karls-Universität Heidelberg, 2008.

[PT+09] J. F. Pérez-Torres et al. "Asymmetric electron angular distributions in resonant dissociative photoionization of H_2 with ultrashort xuv pulses". In: *Physical Review A* 80.1 (July 2009), p. 011402.

[Red+12] T. J. Reddish et al. "Observation of Interference between Two Distinct Autoionizing States in Dissociative Photoionization of H_2". In: *Physical Review Letters* 108.2 (Jan. 2012), p. 023004.

[Rei03] Katharine L. Reid. "Photoelectron Angular Distributions". In: *Annual Review of Physical Chemistry* 54.1 (2003), pp. 397–424.

[Rie12] H. Rietz. "Attosekundenphysik mit dem Reaktionsmikroskop: Eine Konzeptstudie, erste Experimente und mögliche Anwendungen". PhD thesis. Ruprecht-Karls-Universität Heidelberg, 2012.

[Rij+00] A.M Rijs et al. "Magnetic bottle spectrometer as a versatile tool for laser photoelectron spectroscopy". In: *Journal of Electron Spectroscopy and Related Phenomena* 112 (Nov. 2000), pp. 151–162.

[Rob04] R. W. Robinett. "Quantum wave packet revivals". In: *arXiv:quant-ph/0401031* (Jan. 2004).

[RS60] A. C. Riviere and D. R. Sweetman. "Dissociation of H_2^+ and He^- by Electric Fields". In: *Physical Review Letters* 5.12 (Dec. 1960), pp. 560–562.

[Sae04] Alejandro Saenz. "Molecular Hydrogen in Strong Laser Fields: Bond Softening, Enhanced Ionisation, and Coherent Control". In: *Physica Scripta* 110 (2004), p. 126.

[San+06] G. Sansone et al. "Isolated Single-Cycle Attosecond Pulses". In: *Science* 314.5798 (Oct. 2006), pp. 443–446.

[San+10] G. Sansone et al. "Electron localization following attosecond molecular photoionization". In: *Nature* 465.7299 (June 2010), pp. 763–766.

[San+12] G. Sansone et al. "Attosecond Time-Resolved Electron Dynamics in the Hydrogen Molecule". In: *Selected Topics in Quantum Electronics, IEEE Journal of* 18.1 (Feb. 2012), pp. 520 –530.

[SBM06] Jose Luis Sanz-Vicario, Henri Bachau, and Fernando Martín. "Time-dependent theoretical description of molecular autoionization produced by femtosecond xuv laser pulses". In: *Physical Review A* 73.3 (Mar. 2006), p. 033410.

[Sch+10] M. Schultze et al. "Delay in Photoemission". en. In: *Science* 328.5986 (June 2010), pp. 1658–1662.

[Sch+97] H.T. Schmidt et al. "A Design Study for an Internal Gas-Jet Target for the Heavy-Ion Storage Ring CRYRING". In: *Hyperfine Interactions* 108 (1997), p. 339.

[Sch+98] M. Schnürer et al. "Guiding and high-harmonic generation of sub-10-fs pulses in hollow-core fibers at $10^{15}\,\mathrm{W/cm^2}$". In: *Applied Physics B: Lasers and Optics* 67.2 (1998), pp. 263–266.

[Sch01] W. P. Schleich. *Quantum Optics in Phase Space*. Wiley-VCH, 2001.

[Sch12] M. Schuricke. "Two and Three Photon Double Ionization of Lithium". PhD thesis. Ruprecht-Karls-Universität Heidelberg, 2012.

[Sen09] A. Senftleben. "Kinematically complete study on electron impact ionisation of aligned hydrogen molecules". PhD thesis. Ruprecht-Karls-Universität Heidelberg, 2009.

[SFH00] K. Sändig, H. Figger, and T. W. Hänsch. "Dissociation Dynamics of H_2^+ in Intense Laser Fields: Investigation of Photofragments from Single Vibrational Levels". In: *Physical Review Letters* 85.23 (Dec. 2000), pp. 4876–4879.

[Sha70] T.E. Sharp. "Potential energy curves for molecular hydrogen and its ions". In: *Atomic Data and Nuclear Data Tables* 2.0 (Dec. 1970), pp. 119–169.

[Shi65] Jon H. Shirley. "Solution of the Schrödinger Equation with a Hamiltonian Periodic in Time". In: *Physical Review* 138.4B (May 1965), B979–B987.

[SM85] Donna Strickland and Gerard Mourou. "Compression of amplified chirped optical pulses". In: *Optics Communications* 55.6 (Oct. 1985), pp. 447–449.

[SM97] I. Sánchez and F. Martín. "The doubly excited states of the H_2 molecule". In: *The Journal of Chemical Physics* 106.18 (May 1997), pp. 7720–7730.

[SM98] I. Sánchez and F. Martín. "Resonant dissociative photoionization of H_2 and D_2". In: *Physical Review A* 57.2 (Feb. 1998), pp. 1006–1017.

[SM99a] I. Sánchez and F. Martín. "Dissociative photoionization of H_2 and D_2 by (30 to 37) eV photons via $^1\Pi_u$ states". In: *Physical Review A* 60.3 (1999), pp. 2200–2206.

[SM99b] I. Sánchez and F. Martín. "Doubly excited autoionizing states of H_2 above the second ionization threshold: the Q_2 resonance series". In: *The Journal of Chemical Physics* 110.14 (1999), p. 6702.

[SM99c] I. Sánchez and F. Martín. "Multichannel Dissociation in Resonant Photoionization of H_2". In: *Physical Review Letters* 82.19 (May 1999), pp. 3775–3778.

[Sol+06] I. J. Sola et al. "Controlling attosecond electron dynamics by phase-stabilized polarization gating". en. In: *Nature Physics* 2.5 (2006), pp. 319–322.

[Spe+10] A. Sperl et al. "Sideband Oscillations in XUV/IR Pump-Probe Experiments". In: *Progress Report 2009-2010, Max-Planck-Institut für Kernphysik* 139 (2010), p. 139.

[Spi+97] Ch. Spielmann et al. "Generation of Coherent X-Rays in the Water Window Using 5-Femtosecond Laser Pulses". In: *Science* 278.5338 (Oct. 1997), pp. 661–664.

[SRM12] R. E. F. Silva, P. Rivière, and F. Martín. "Autoionizing decay of H_2 doubly excited states by using xuv pump infrared probe schemes with trains of attosecond pulses". In: *Physical Review A* 85.6 (June 2012), p. 063414.

[SV+10] J. L. Sanz-Vicario et al. "Molecular frame photoelectron angular distributions for H_2 ionization by single and trains of attosecond XUV laser pulses". In: *International Journal of Quantum Chemistry* 110.13 (2010).

[TNF08] Uwe Thumm, Thomas Niederhausen, and Bernold Feuerstein. "Time-series analysis of vibrational nuclear wave-packet dynamics in D_2^+". In: *Physical Review A* 77.6 (June 2008), p. 063401.

[Tza+03] P. Tzallas et al. "Direct observation of attosecond light bunching". en. In: *Nature* 426.6964 (Nov. 2003), pp. 267–271.

[Ull+03] J. Ullrich et al. "Recoil-ion and electron momentum spectroscopy: reaction-microscopes". In: *Rep. Prog. Phys.* 66 (2003), pp. 1463–1545.

[VTM96] Valerie Veniard, Richard Taieb, and Alfred Maquet. "Phase dependence of (N+1)-color (N>1) ir-uv photoionization of atoms with higher harmonics". In: *Physical Review A* 54 (1 1996), pp. 721–728.

[Wig32] E. Wigner. "Ionization in the field of a strong electromagnetic wave". In: *Physical Review* 40.749 (1932).

[Yan+08] V. Yanovsky et al. "Ultra-high intensity- 300-TW laser at 0.1 Hz repetition rate". In: *Optics Express* 16.3 (Feb. 2008), pp. 2109–2114.

[YSD98] M. Yan, H. R. Sadeghpour, and A. Dalgarno. "Photoionization Cross Sections of He and H_2". In: *The Astrophysical Journal* 496.2 (Apr. 1998), pp. 1044–1050.

[Zer+97] Raoul Zerne et al. "Phase-Locked High-Order Harmonic Sources". In: *Physical Review Letters* 79.6 (1997), pp. 1006–1009.

[Zew00] A. H. Zewail. "Femtochemistry: Atomic-Scale Dynamics of the Chemical Bond". In: *The Journal of Physical Chemistry A* 104.24 (June 2000), pp. 5660–5694.

[Zro05] K. Zrost. "Wechselwirkung von Atomen und kleinen Molekülen mit intensiven Laserpulsen". PhD thesis. Ruprecht-Karls-Universität Heidelberg, 2005.